



University of Kentucky  
UKnowledge

---

Theses and Dissertations--Mechanical  
Engineering

Mechanical Engineering

---

2012

## SIMULATION OF WHISTLE NOISE USING COMPUTATIONAL FLUID DYNAMICS AND ACOUSTIC FINITE ELEMENT SIMULATION

Jiawei Liu

University of Kentucky, [jiawei.liu@uky.edu](mailto:jiawei.liu@uky.edu)

[Right click to open a feedback form in a new tab to let us know how this document benefits you.](#)

---

### Recommended Citation

Liu, Jiawei, "SIMULATION OF WHISTLE NOISE USING COMPUTATIONAL FLUID DYNAMICS AND ACOUSTIC FINITE ELEMENT SIMULATION" (2012). *Theses and Dissertations--Mechanical Engineering*. 9. [https://uknowledge.uky.edu/me\\_etds/9](https://uknowledge.uky.edu/me_etds/9)

This Master's Thesis is brought to you for free and open access by the Mechanical Engineering at UKnowledge. It has been accepted for inclusion in Theses and Dissertations--Mechanical Engineering by an authorized administrator of UKnowledge. For more information, please contact [UKnowledge@lsv.uky.edu](mailto:UKnowledge@lsv.uky.edu).

## **STUDENT AGREEMENT:**

I represent that my thesis or dissertation and abstract are my original work. Proper attribution has been given to all outside sources. I understand that I am solely responsible for obtaining any needed copyright permissions. I have obtained and attached hereto needed written permission statements(s) from the owner(s) of each third-party copyrighted matter to be included in my work, allowing electronic distribution (if such use is not permitted by the fair use doctrine).

I hereby grant to The University of Kentucky and its agents the non-exclusive license to archive and make accessible my work in whole or in part in all forms of media, now or hereafter known. I agree that the document mentioned above may be made available immediately for worldwide access unless a preapproved embargo applies.

I retain all other ownership rights to the copyright of my work. I also retain the right to use in future works (such as articles or books) all or part of my work. I understand that I am free to register the copyright to my work.

## **REVIEW, APPROVAL AND ACCEPTANCE**

The document mentioned above has been reviewed and accepted by the student's advisor, on behalf of the advisory committee, and by the Director of Graduate Studies (DGS), on behalf of the program; we verify that this is the final, approved version of the student's dissertation including all changes required by the advisory committee. The undersigned agree to abide by the statements above.

    Jiawei Liu, Student

    Dr. David W. Herrin, Major Professor

    Dr. J. M. McDonough, Director of Graduate Studies

SIMULATION OF WHISTLE NOISE USING COMPUTATIONAL  
FLUID DYNAMICS AND ACOUSTIC FINITE ELEMENT SIMULATION

---

THESIS

---

A thesis submitted in partial fulfillment of the  
requirements for the degree of Master of Science  
in Mechanical Engineering in the College of Engineering  
at the University of Kentucky

By

Jiawei Liu

Lexington, Kentucky

Director: Dr. D. W. Herrin, Professor of Mechanical Engineering  
Co-director: Dr. Tingwen Wu, Professor of Mechanical Engineering

Lexington, Kentucky

2012

Copyright © Jiawei Liu 2012

## ABSTRACT OF THESIS

### SIMULATION OF WHISTLE NOISE USING COMPUTATIONAL FLUID DYNAMICS AND ACOUSTIC FINITE ELEMENT SIMULATION

The prediction of sound generated from fluid flow has always been a difficult subject due to the nonlinearities in the governing equations. However, flow noise can now be simulated with the help of modern computation techniques and super computers. The research presented in this thesis uses the computational fluid dynamics (CFD) and the acoustic finite element method (FEM) in order to simulate the whistle noise caused by vortex shedding. The acoustic results were compared to both analytical solutions and experimental results to better understand the effects of turbulence models, fluid compressibility, and wall boundary meshes on the acoustic frequency response. In the case of the whistle, sound power and pressure levels are scaled since 2-D models are used to model 3-D phenomenon. The methodology for scaling the results is detailed.

**KEYWORDS:** Acoustics, CFD, Whistle Noise, Finite Element Method, Scaling

Jiawei Liu

June 21, 2012

SIMULATION OF WHISTLE NOISE USING COMPUTATIONAL  
FLUID DYNAMICS AND ACOUSTIC FINITE ELEMENT SIMULATION

By

Jiawei Liu

Dr. D.W. Herrin  
(Director of Thesis)

Dr. Tingwen Wu  
(Co-director of Thesis)

Dr. J. M. McDonough  
(Director of Graduate Studies)

June 21<sup>st</sup>, 2012

## ACKNOWLEDGMENTS

I would like to express my sincere thankfulness to my graduate study advisor, Dr. David W. Herrin, for his guidance and patience during my graduate study at the University of Kentucky. I am also grateful to Dr. Herrin for giving me the opportunities to participate in trainings and conferences and providing me with exposure to industrial projects. I would also like to thank Dr. Tingwen Wu, the co-director of this thesis, for his help and advice during both my undergraduate and graduate studies. My sincere appreciation also goes to Dr. Sean Baily and Dr. James McDonough, who have provided insights which guided and challenged my thinking, and substantially improving the thesis.

I am also grateful to the students and friends, Jinghao Liu, Xin Hua, Limin Zhou, Srinivasan Ramalingam, Yitian Zhang and Rui He, who all have helped me and made my stay full of fun memories.

And finally, thank you Mom and Dad for supporting me on everything.

# Table of Contents

<b>ACKNOWLEDGMENTS</b> .....	<b>III</b>
<b>LIST OF TABLES</b> .....	<b>VIII</b>
<b>LIST OF FIGURES</b> .....	<b>IX</b>
<b>CHAPTER 1 INTRODUCTION</b> .....	<b>1</b>
1.1 INTRODUCTION .....	1
1.2 OBJECTIVES.....	3
1.3 MOTIVATION.....	4
1.4 APPROACH AND JUSTIFICATION .....	4
1.5 ORGANIZATION.....	4
<b>CHAPTER 2 BACKGROUND</b> .....	<b>6</b>
2.1 ACOUSTIC SOURCES.....	6
2.1.1 <i>Monopole</i> .....	6
2.1.2 <i>Dipole</i> .....	7
2.1.3 <i>Quadrupoles</i> .....	9
2.2 VORTEX SHEDDING .....	10
2.3 SOUND INDUCED BY VORTEX SHEDDING .....	15
2.4 Lighthill ANALOGY .....	18
2.4.1 <i>Development of Lighthill's Analogy</i> .....	19
2.5 CFD TURBULENCE MODELS .....	23

2.5.1	<i>k – ε Turbulence Model</i> .....	23
2.5.2	<i>k – ω model</i> .....	24
2.5.3	<i>Large Eddy Simulation</i> .....	28
2.6	ACOUSTIC FEM .....	30
2.6.1	<i>Introduction</i> .....	30
2.6.2	<i>Infinite Element</i> .....	32
<b>CHAPTER 3</b>	<b>SIMULATION APPROACH</b> .....	<b>35</b>
3.1	INTRODUCTION .....	35
3.1.1	<i>Computational Aeroacoustics</i> .....	35
3.1.2	<i>CFD-Sound Propagation Solver Coupling</i> .....	36
3.1.3	<i>Broadband Noise Sources Models</i> .....	37
3.2	GENERAL ASSUMPTIONS.....	37
3.2.1	<i>Model Dimension</i> .....	37
3.2.2	<i>Fluid Compressibility</i> .....	38
3.2.3	<i>Interactions and Feedbacks</i> .....	39
3.3	CFD-SOUND PROPAGATION SOLVER COUPLING PROCESS .....	40
3.3.1	<i>Comments on Source Mapping</i> .....	41
3.4	FAST FOURIER TRANSFORM FOR AEROACOUSTIC SIMULATION .....	42
3.4.1	<i>Determine Time Step Size and Number of Time Steps for CFD Simulation</i> ...	42
3.5	WALL BOUNDARY MESHING REQUIREMENTS .....	43
3.6	SCALING OF ACOUSTIC RESULT.....	45
3.6.1	<i>Sound Power Scaling Laws</i> .....	45



3.6.2	<i>Finite Length Scaling</i> .....	46
<b>CHAPTER 4</b>	<b>VERIFICATION OF SIMULATION APPROACH</b> .....	<b>48</b>
4.1	LID-DRIVEN TEST CASE FOR MESH SELECTION .....	48
4.1.1	<i>CFD Mesh Types</i> .....	48
4.1.2	<i>Lid-Driven Case Meshes</i> .....	50
4.1.3	<i>CFD Simulation Setup</i> .....	51
4.1.4	<i>Result and Discussion</i> .....	53
4.2	HELMHOLTZ RESONATOR CASE STUDY .....	57
4.2.1	<i>Helmholtz Resonator</i> .....	57
4.2.2	<i>Geometry and Mesh</i> .....	60
4.2.3	<i>Simulation Setup and Steps</i> .....	62
4.2.3.1	<i>Steady State Solution</i> .....	64
4.2.3.2	<i>Transient Solution</i> .....	66
4.2.3.3	<i>Acoustic Solution</i> .....	69
4.2.4	<i>Result and Discussion</i> .....	73
4.3	FLOW OVER CYLINDER CASE STUDY .....	74
4.3.1	<i>Geometry and Mesh</i> .....	75
4.3.2	<i>Transient CFD solution</i> .....	78
4.3.3	<i>Acoustic Simulation</i> .....	81
4.3.4	<i>Result and Discussion</i> .....	84
<b>CHAPTER 5</b>	<b>WHISTLE CASE STUDY – MEASUREMENT AND SIMULATION</b> .....	<b>86</b>

5.1	WHISTLE GEOMETRY .....	86
5.2	SOUND PRESSURE MEASUREMENT .....	88
5.3	CFD SIMULATION .....	90
5.3.1	<i>CFD Mesh</i> .....	90
5.3.2	<i>CFD Simulations</i> .....	91
5.3.3	<i>Acoustic Simulation</i> .....	95
5.3.4	<i>Scaling</i> .....	96
5.3.5	<i>Results and Discussion</i> .....	97
<b>CHAPTER 6</b>	<b>SUMMARY AND FUTURE WORK .....</b>	<b>100</b>
6.1	SUMMARY .....	100
6.2	FUTURE WORK .....	102
<b>REFERENCES</b>	<b>.....</b>	<b>104</b>
<b>VITA</b>	<b>.....</b>	<b>113</b>

## List of Tables

Table 1 Scaling Laws for Sound Power in Sound Fields with Different Dimensions.....	46
Table 2 Dimension of the Simulated Helmholtz Resonator .....	61
Table 3 Steady State Simulation Setup.....	65
Table 4 Transient LES Simulation Setup.....	66
Table 5 $y^+$ and Corresponding Wall Height.....	76
Table 6 Transient SST $k - \omega$ Simulation Setup.....	79
Table 7 CFD Simulation Setup (Common Parameters).....	92
Table 8 Simulation Setup (Parameters for Each Case).....	92

## List of Figures

Figure 1 Dipole Obtained by Superposition of Two Monopoles ( $kl \ll 1$ ) [9].....	7
Figure 2 Generation of Dipoles (Reproduced [9]).....	8
Figure 3 Superposition of Dipoles .....	9
Figure 4 Locations of Sound Sources on an Automobile Body [10].....	11
Figure 5 Vortex Street after a Cylindrical Obstacle.....	12
Figure 6 Regimes of Fluid Flow across Circular Cylinders .....	14
Figure 7 Relf's Motor Driven Apparatus .....	15
Figure 8 Re-plot of Strouhal's results for thin resonating brass wires, with the formulas of Lord Rayleigh, Roshko and Berger for comparison [16] .....	16
Figure 9 Polar distribution of sound pressure about rotating rod. Solid curve, observed; dotted curve, computed. [18] .....	17
Figure 10 Edge tone [41] .....	38
Figure 11 CFD-Sound Propagation Solver Coupling Solution Process .....	40
Figure 12 Linear Interpolation Source Projection Method.....	41
Figure 13 Conservative Integration Source Projection Method .....	42
Figure 14 Divisions of Near-wall Region.....	44
Figure 15 Line Source [9].....	47
Figure 16 An Example of Structured Mesh [48] .....	49
Figure 17 Unstructured Mesh around a NASA Airfoil (Matlab Demo).....	49
Figure 18 An Example of Hybrid Mesh [48].....	50
Figure 19 Meshes Used in Lid-Driven Case.....	51
Figure 20 Boundary Condition of the Lid-Driven Case .....	52

Figure 21 $x$ -Velocity at the Vertical Center Line.....	54
Figure 22 $x$ -Velocity at the Vertical Center Line.....	54
Figure 23 Velocity Contour Plot (Free Quad Elements) .....	55
Figure 24 Velocity Contour Plot (Structured Quad Elements).....	55
Figure 25 Continuity Residual History .....	56
Figure 26 Friction Coefficient History (At the Moving Wall) .....	56
Figure 27 Helmholtz Resonator and Spring-Mass Damper Analogy .....	59
Figure 28 Geometry of the Simulated Helmholtz Resonator.....	60
Figure 29 Helmholtz Resonator Mesh for CFD Simulation .....	61
Figure 30 Helmholtz Resonator Mesh for Acoustic Simulation.....	62
Figure 31 Simulation Process .....	63
Figure 32 Velocity Contour Plot (Steady State) .....	65
Figure 33 Non-Iterative Time-Advancement Scheme [6] .....	67
Figure 34 Velocity Contour Plot (Transient) .....	68
Figure 35 FFT with Integer Number of Periods .....	70
Figure 36 FFT with Non-Integer Number of Periods .....	70
Figure 37 FFT with Non-Integer Number of Periods (Windowed).....	71
Figure 38 Divergence of Lighthill Surface at 131 Hz.....	72
Figure 39 Direct Frequency Analysis Setup .....	73
Figure 40 Radiated Sound Power at Outlet.....	73
Figure 41 Flow Over Cylinder Case Geometry .....	75
Figure 42 Mesh for the Flow Over Cylinder Case.....	77
Figure 43 Acoustic Mesh for the Flow Over Cylinder Case .....	77

Figure 44 Velocity Contour of Compressible Flow, $y^+ = 1$ Case .....	79
Figure 45 Velocity Contour of Incompressible Flow, $y^+ = 1$ Case .....	80
Figure 46 Velocity Contour of Compressible Flow, $y^+ = 30$ Case .....	80
Figure 47 Velocity Contour of Incompressible Flow, $y^+ = 30$ Case .....	81
Figure 48 Divergence of Lighthill Surface at 477 Hz (Compressible, $y^+ = 1$ ) .....	82
Figure 49 Divergence of Lighthill Surface at 477 Hz (Incompressible, $y^+ = 1$ ) .....	82
Figure 50 Direct Frequency Analysis Setup .....	83
Figure 51 Radiated Sound Power at Outlet.....	84
Figure 52 Solid Model of the Whistle.....	87
Figure 53 Cross Section of the Whistle .....	87
Figure 54 Experimental Scheme .....	88
Figure 55 Experimental Setup .....	88
Figure 56 Averaged Measured Sound Pressure Level.....	89
Figure 57 CFD Mesh of the Whistle.....	91
Figure 58 Contour of Velocity Magnitude (Run1) .....	93
Figure 59 Contour of Velocity Magnitude (Run2) .....	93
Figure 60 Contour of Velocity Magnitude (Run3) .....	94
Figure 61 Contour of Velocity Magnitude (Run4) .....	94
Figure 62 Boundary Conditions of Acoustic Simulation.....	95
Figure 63 Scale the Sound Pressure of a Whistle .....	97
Figure 64 Whistle Simulation Results (Incompressible) .....	99
Figure 65 Whistle Simulation Results (Compressible).....	99

# Chapter 1

## Introduction

### 1.1 Introduction

When talking about acoustics, most people relate it to music. However, music, joyful sound, is not the only important aspect in acoustics. Acoustic noise is a major concern of society and industry, and aerodynamic or flow noise is especially concerning because it is closely related to the level of comfort of the environments in which people live and work. Common examples of aerodynamic noise are jet noise and noise generated when fluid flows over obstacles and cavities.

The prediction of sound generated from fluid flow has always been a difficult subject due to the nonlinearities in the governing equations. However, flow noise can now be simulated with the help of modern computation techniques and super computers.

Aerodynamic noise is a result of unsteady gas flow and the interaction of the unsteady gas flow with the associated structure. The unwanted gas flow and structure interaction may cause serious problems in industrial products such as the instability of the structures and structure fatigue [1]. Accordingly, simulating the aerodynamic noise is necessary and will improve the quality of the products at the design stage. However, due to the nature of turbulent flow and the limitation of computational power, it is not always feasible to obtain a reliable unsteady (transient) CFD solution for the aerodynamic noise analysis. The computational effort and time is a major hindrance. Even if there were no time limitation, any one of the commonly used turbulent models is not capable of solving

all scales of turbulence. Therefore, a time-efficient method with acceptable accuracy is needed in order to estimate flow noise.

Several well-known theories such as the theory of Lighthill [2] and the theory of Ffowcs Williams and Hawkings (FWH) [3] have been successfully applied to aeroacoustic problems. The theory of Lighthill is the foundation of the FWH approach. In Lighthill's paper, it has been shown that aerodynamic sound sources can be modeled as series of monopoles, dipoles, and quadrupoles generated by the turbulence in an ideal fluid region surrounded by a large fluid region at rest (i.e., velocity field in the fluid is zero).

In Lighthill's analogy, no fluid flow and sound wave interaction is considered. A justification of this assumption has been given in Lighthill's original paper. Due to the large difference in energy, there is very little feedback from acoustics to the flow. For flows in the low Mach number regimes, direct simulations are often costly, unstable, inefficient and unreliable due to the presence of rapidly oscillating acoustic waves (with periods proportional to the Mach number) in the equations themselves [4]. Even with the aforementioned difficulties, reliable results are sometimes obtained using a combination of incompressible (or compressible) flow solvers and Lighthill's analogy at low Mach number [5].

Commercial codes such as ANSYS FLUENT have incorporated the FWH approach in a computational aeroacoustics module. FWH assumes that there are no obstacles between the sound sources and the receivers [6]. Therefore, the sound radiation problem is inherently a weak part of the simulation, especially if the sound source is in a



waveguide or duct, enclosed, or obstructed in some way. One way to bypass this problem is to utilize acoustic finite element simulation and use infinite elements to simulate acoustic radiation at the boundary of the mesh.

This thesis examines the combination of the CFD solvers and the infinite element technique for the prediction of sound radiated from turbulent flow with the effects of vortex shedding. Based on the results derived from the test cases, guidelines for CFD modeling of low subsonic flow noise caused by vortex shedding is documented in an effort to improve the efficiency of the modeling process and select proper turbulent models.

## **1.2 Objectives**

This study will use the commercial code ANSYS FLUENT as a pure CFD solver and FFT ACTRAN as the acoustic wave solver. The sound pressure or sound power generated by turbulent flows will be obtained and compared to the theoretical values.

The cases studied include sound generated by:

- a. Flow over a cylinder
- b. Flow over a cavity (Helmholtz Resonator)
- c. Flow in a sports whistle

The study will be restricted to 2-D models with vortex shedding frequencies expected to be under or close to 2000 Hz. Fluid-structure interaction will not be considered in this study. Though the cases studied do not completely reflect real world situations, the

guidelines presented herein should benefit the simulation of future, more complicated situations.

### **1.3 Motivation**

Noise induced by flow over obstacles is a common engineering problem. In most instances, vortex shedding is the major culprit. Of course, vortex induced vibration (VIV) is well known to cause serious engineering failures (such as structure fatigue). However, vortex shedding also leads to unwanted noise in ducts and pipes, refrigeration systems, and in automotive applications [7]. Accordingly, it will be beneficial to model some simpler cases to guide simulation and CFD solver selection in more difficult cases. Using simulation, engineers can make modifications to a design in a virtual environment and avert serious aeroacoustic problems. Commercial software will be used in this investigation since it is readily available in academia and industry.

### **1.4 Approach and justification**

The built-in turbulence models in ANSYS FLUENT will be utilized for the CFD simulations since these models have proved reasonably accurate in industrial applications. The acoustic finite element method, using infinite elements at the boundary, will be used to solve the acoustic wave propagation from the flow sources which are determined using Lighthill's analogy. The acoustic finite element method is considered a standard approach for solving steady state acoustic problems [8].

### **1.5 Organization**

This thesis is organized into six chapters. Chapter 2 presents some background information about acoustics, including basic definitions. Some basics of vortex shedding

are also included. Chapter 3 discusses the simulation approach, including a literature review on turbulent models and vortex phenomenon. Additionally, the acoustic simulation approach is reviewed. In Chapter 4, a classic CFD problem called the lid-driven problem is studied. Additionally, Chapter 4 presents a validation of the simulation approach for two well-known vortex shedding cases, which have been thoroughly studied theoretically. The first case is flow over a rod, and the second is flow over a cavity. In Chapter 5, sound radiation from a whistle is simulated and compared to experimental results. Finally, Chapter 6 summarizes the results and includes recommendations for future research.

## Chapter 2 Background

### 2.1 Acoustic Sources

Lighthill [2] identified three categories of sound sources due to flow: monopoles, dipoles, and quadrupoles. Monopoles results from a fluctuating volume or mass flow. Dipoles can form when there are fluctuating forces. When fluctuating force couples appear, quadrupoles can form as a result. Although higher order poles do exist in aeroacoustic problems, they are usually not considered because of their low radiated power.

#### 2.1.1 Monopole

A monopole radiates sound equally in all directions and is the simplest acoustic source. In aeroacoustics, monopoles normally result from pulsating flow. Examples include tire, and compressor noise. One example of a monopole source is a pulsating sphere. Likewise, a loudspeaker can be approximated as a monopole source at low frequencies. The particle velocity of a monopole in the radial direction is given by

$$u(r, t) = \frac{\tilde{A}}{\rho_0 c r} \left( 1 + \frac{1}{i k r} \right) e^{i(\omega t - k r)} \quad \text{Equation 2-1}$$

where  $\tilde{A}$  is the amplitude [kg/s<sup>2</sup>],  $k$  is the wave number,  $\rho_0$  is the density of the medium,  $c$  is the speed of sound in the medium, and  $\omega$  is the angular frequency. If the monopole source has an infinitely small radius, the volume flow rate can be obtained by taking the limit of the product of the surface area and the particle velocity when the radius goes to zero which yields

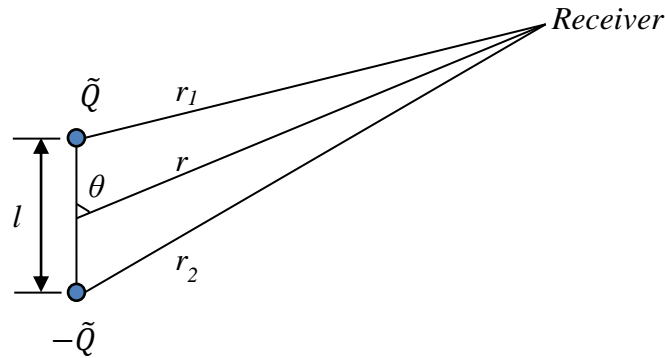
$$\tilde{Q} = \frac{4\pi\tilde{A}}{i\omega\rho_0} \quad \text{Equation 2-2}$$

Therefore, the sound pressure for a simple monopole source at a distance  $r$  is given by

$$p(r, t) = i\rho_0\omega \frac{\tilde{Q}}{4\pi r} e^{i(\omega t - kr)} \quad \text{Equation 2-3}$$

### 2.1.2 Dipole

A dipole is the superposition of two monopoles that are out of phase. In aeroacoustics, dipoles are normally the result of vortex shedding. Examples include flow over a rod or cavity.



**Figure 1 Dipole Obtained by Superposition of Two Monopoles ( $kl \ll 1$ ) [9]**

The sound pressure at the receiver is obtained by adding the sound pressure generated by the monopoles out-of-phase and can be expressed as

$$p = \frac{\rho_0 i \omega \tilde{Q}}{4\pi} \left( \frac{e^{-ikr_1}}{r_1} - \frac{e^{-ikr_2}}{r_2} \right) e^{i\omega t} \quad \text{Equation 2-4}$$

By utilizing the law of cosines, with the limit of  $l$  goes to zero, the sound field induced by the simple dipole can be expressed as

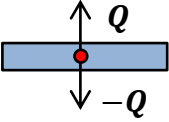

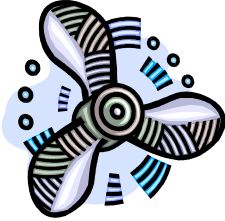
$$p = \frac{ikF \cos \theta}{4\pi r} \left(1 + \frac{1}{ikr}\right) e^{-i(\omega t - kr)} \quad \text{Equation 2-5}$$

where

$$F = Ql$$

where  $Q$  is the volume flow rate and  $l$  is the distance between the two out-of-phase monopoles.

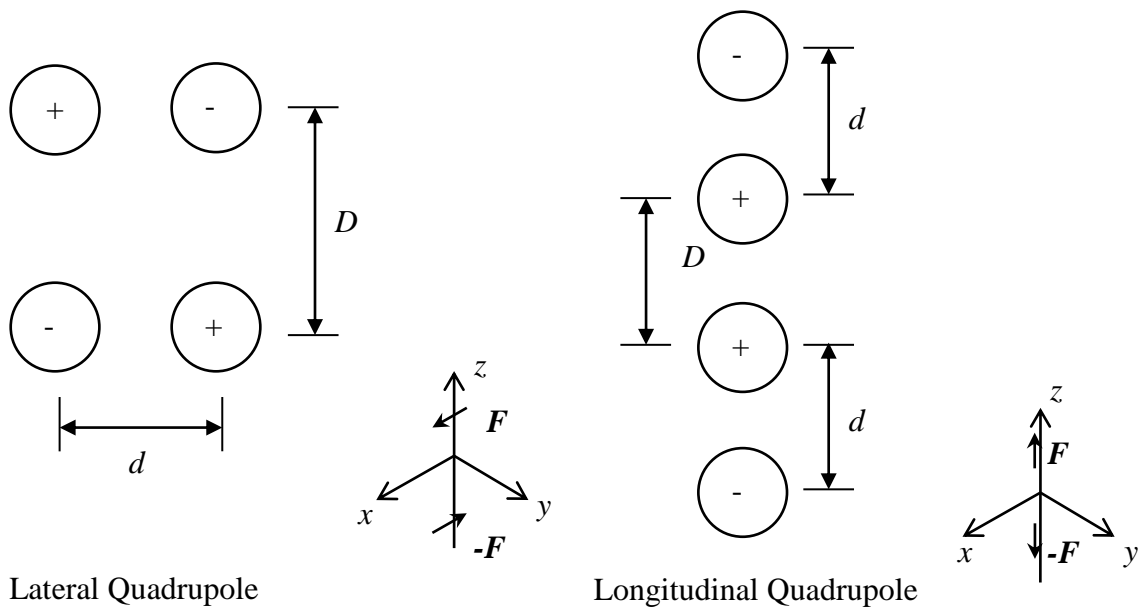
It can be seen that dipole sources are induced by forces instead of volume changes in monopoles. In turbulent flow fields, the fluctuating pressure creates a distribution of dipoles at the surface of the body breaking the flow [9]. Figure 2 shows a few of the physical situations that give rise to dipole sources at low frequencies.

Dipole	Physical situation	Sketch
↑ $F$ Fluctuating force	Transversally oscillating bodies	
	Bodies in a flow field	
	Propellers	

**Figure 2 Generation of Dipoles (Reproduced [9])**

### 2.1.3 Quadrupoles

Similar to the formation of a dipole source, a simple quadrupole source can be obtained by the superposition of two dipole sources of the same strength that are out-of-phase (see Figure 3). Quadrupoles arise from turbulence. One example is the jet stream. Depending on the distribution of the dipoles, quadrupoles can be further classified as longitudinal and lateral. Quadrupole sources are induced by fluctuating moments or viscous forces..



**Figure 3 Superposition of Dipoles**

The far field sound pressure for each of the cases in Figure 3 can be expressed by the following Equations 2-6 and 2-7,

$$p_{longitudinal} = -\frac{k^2 M_{zz}}{4\pi r} \cos^2 \theta \quad \text{Equation 2-6}$$

$$p_{lateral} = -\frac{k^2 M_{xz}}{4\pi r} \cos\theta \sin\theta \cos\phi \quad \text{Equation 2-7}$$

where

$$M_{zz} = \rho_0 i \omega Q d D$$

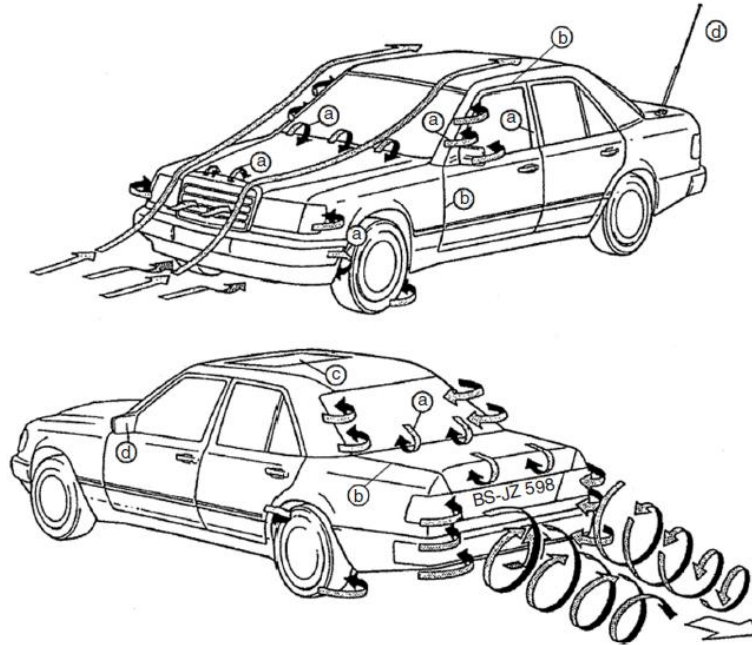
$$M_{xz} = \rho_0 i \omega Q d D$$

$\theta$  and  $\phi$  are the angles the vector  $r$  makes with z-axis and x-axis in spherical coordinates (see Figure 3).

## 2.2 Vortex shedding

In aeroacoustics, unwanted tones are usually caused by vortex shedding. As seen in Figure 4, vortex induced noise can be found in many locations around a vehicle body. At (a) type locations such as the windshield base and front hood edge, abrupt changes in body geometry occur. At (b) type locations such as door gaps, air flows over cavities. At (d) type locations such as the radio antenna, air flows over a cylinder. Separated flow exists at each of these locations and vortex shedding may occur depending on the flow conditions.



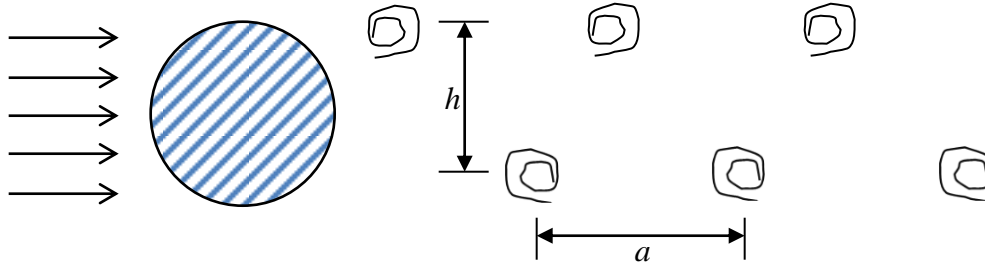


**Figure 4 Locations of Sound Sources on an Automobile Body [10]**

Vortex shedding has been studied since the late 1800s. When viscous fluid flows over solid objects, a boundary layer of fluid around the object will develop. These boundary layers can be either laminar or turbulent which can be determined by local Reynolds numbers. Because of the effects of adverse pressure gradient and the surface viscous stagnation, the flow at the boundary suffers from constant deceleration. Eventually the inertial force is unable to overcome the resistance, and a boundary layer will start to separate from the surface of the object. With the help of the main stream flow, the separated boundary layer will form a pair of vortices rotating in opposite directions. The two vortices shed off alternately and a vortex street forms as the separations occur continuously behind the object, such as a circular cylinder. This phenomenon is named after the engineer Theodore von Karman. A relatively steady vortex street formed after a circular cylinder has the following relation [11]:

$$\frac{h}{a} = 0.281$$

where  $h$  and  $a$  are shown in Figure 5.



**Figure 5 Vortex Street after a Cylindrical Obstacle**

The vortex shedding frequency can be obtained from Equation 2-8 [12]:

$$\frac{fd}{U} = 0.198 \left( 1 - \frac{19.7}{Re} \right) \quad \text{Equation 2-8}$$

where

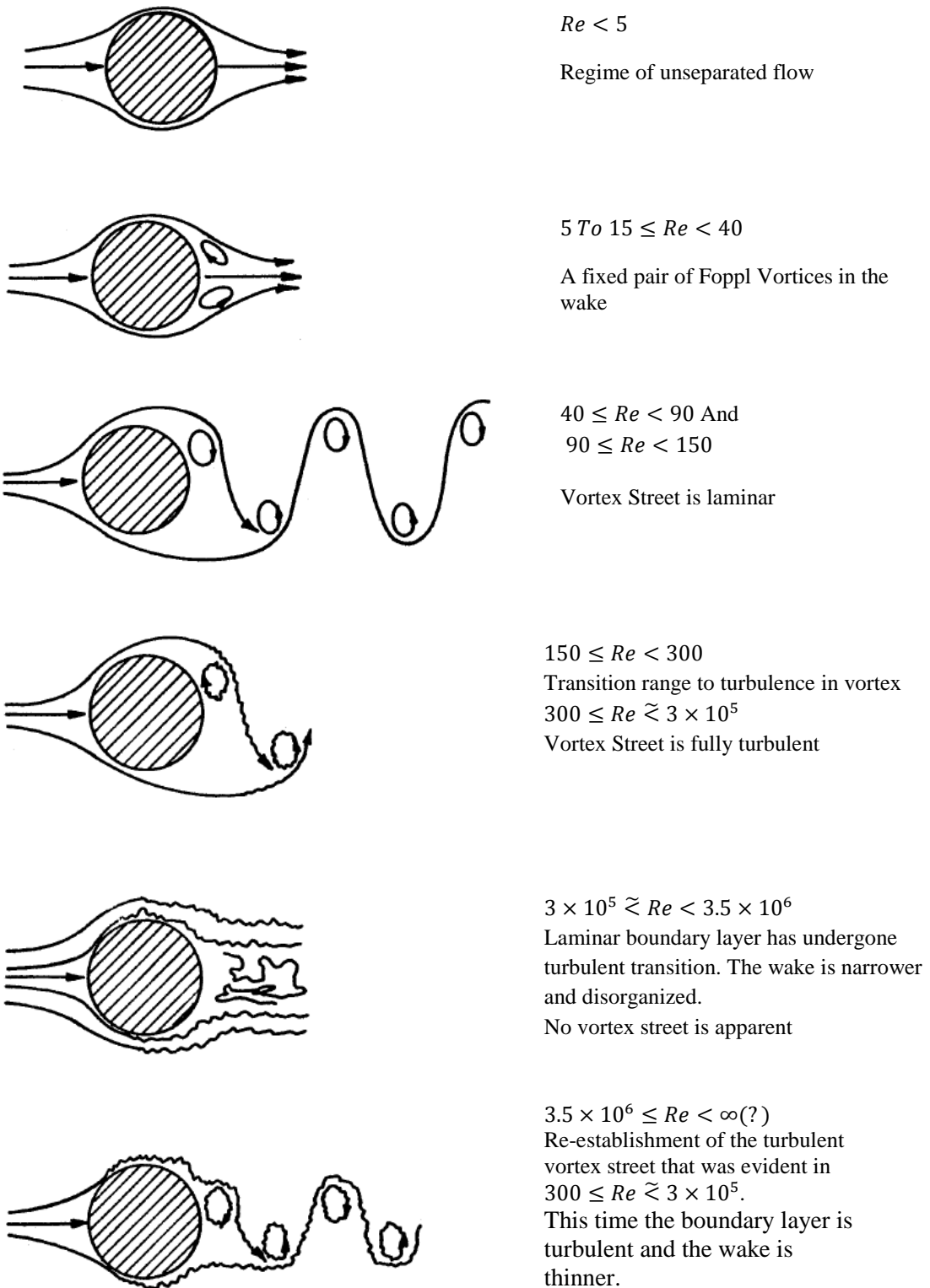
$f$  Vortex shedding frequency

$d$  Diameter of the cylinder

$U$  Flow velocity.

It is important to understand the vortex regimes of fluid flow across obstacles in order to select the more appropriate laminar or turbulent models. Some turbulence models are only suitable for high Reynolds number flows while others are suitable for low Reynolds flows. Figure 3, from Lienhard [13], categorizes the flow regimes for different ranges of Reynolds number.

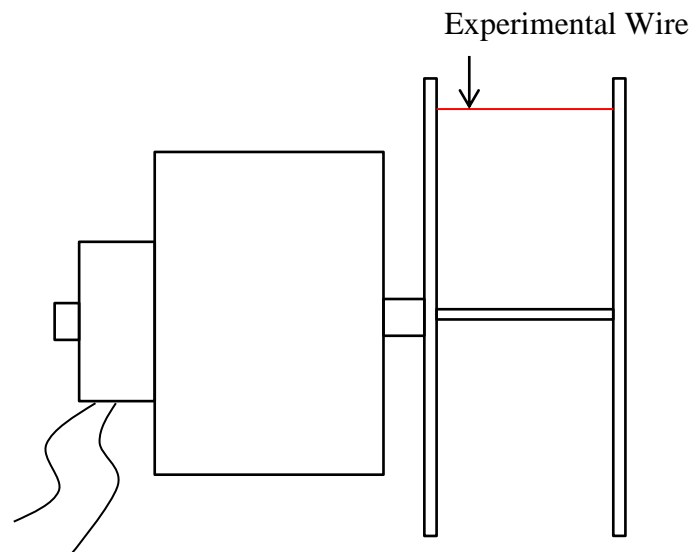
When  $Re < 5$ , the flow is laminar and there is no vortex shedding. As the Reynolds number increases, vortices start to appear in the flow field. When  $Re$  is in the range of 5 to 15, a fixed pair of vortices first appears in the wake of the cylinder. As the Reynolds number increases to about 40, the former fixed pair of vortices becomes stretched and unstable and as a result, the first periodic driving forces begin. Laminar vortex streets appear when Reynolds number is in the range of 40 to 150. The vortices are laminar till Reynolds numbers exceed roughly 150. For Reynolds numbers above 300, the flow will begin to transition from laminar to turbulent until flow is fully turbulent between roughly 300 and  $3 \times 10^5$ . Another transition takes place when Reynolds numbers in the range of  $1 \times 10^5$  and  $5 \times 10^5$ . The exact Reynolds numbers for these transitions will vary depending on the surface roughness and the free-stream turbulence level. Although some of the regimes can be further divided into sub categories, the listed regimes and Reynolds number ranges are sufficient to serve as guidelines for the engineers to select the turbulence models in CFD simulation.



**Figure 6 Regimes of Fluid Flow across Circular Cylinders**

### 2.3 Sound induced by vortex shedding

The first quantitative study of sound induced by vortex shedding was published by Strouhal in 1878. Since then, theoretical models have been developed for predicting the sound generated from flow over cylinders. This part of the thesis serves as a review of the predictions of sound generated by vortex shedding of flow over cylinders.



**Figure 7 Relf's Motor Driven Apparatus**

In Strouhal's experiment, the apparatus he used looks similar to Relf's motor driven wire-air current equipment [14] as shown in Figure 7. Strouhal concluded that [15] (1) the frequency was independent of wire tension or length although the intensity did increase with wire length, and (2) the frequency was approximately predicted by the relationship:

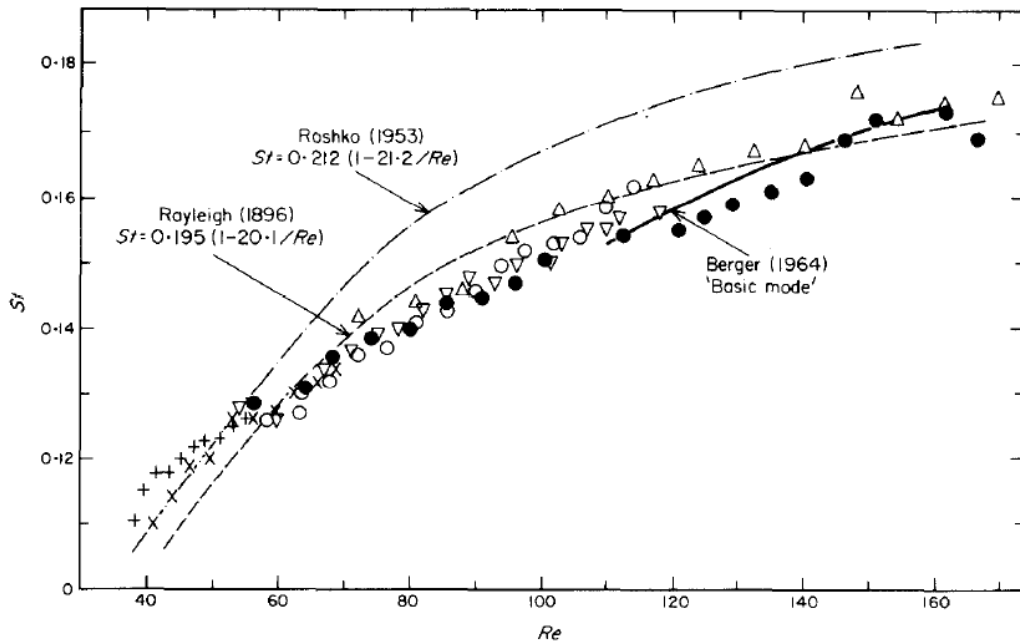
$$f = \frac{StU}{D} \text{ Hz} \quad \text{Equation 2-9}$$

where

$U$  free stream velocity

$D$  diameter of the wire

$St$  Strouhal number



Diameter (mm): +, 0.179; ×, 0.231; ∇, 0.286; ○, 0.327; ●, 0.394; ●, 0.499. — Rayleigh (1896),  $St=0.195(1-20.1/Re)$ ; -.-, Roshko (1953),  $St=0.212(1-21.2/Re)$ ; —·—, Berger (1964) “basic mode”  $St = 0.220(1-33.6/Re)$ .

**Figure 8 Re-plot of Strouhal’s results for thin resonating brass wires, with the formulas of Lord Rayleigh, Roshko and Berger for comparison [16]**

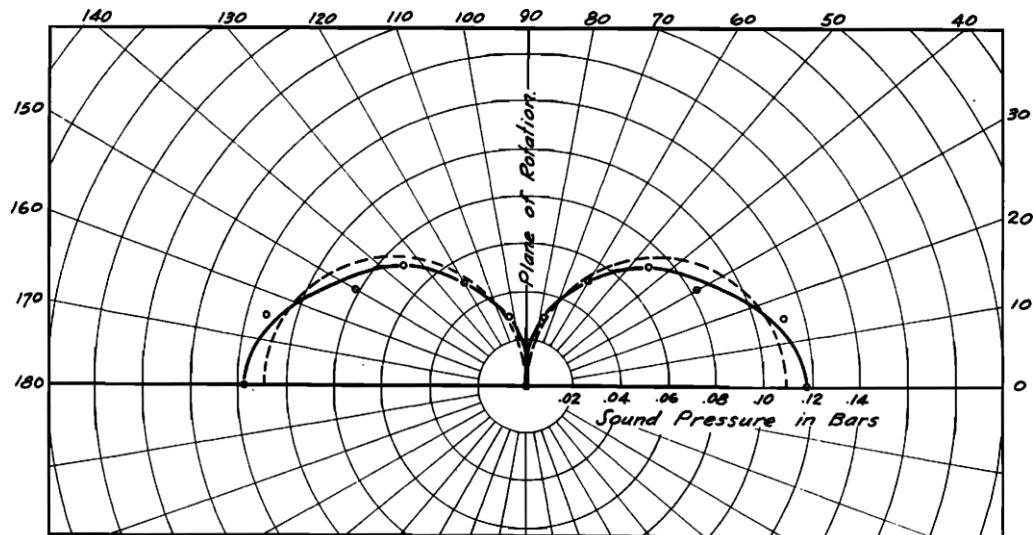
Strouhal’s scaling is considered to work well at low Reynolds numbers. In Zdravkovich’s replot of Strouhal’s results [16] along with other researchers’ results, the sound induced by vortex shedding begins to appear at a Reynolds number close to 40.

Lord Reyleigh's [17] empirical equation matches well with Strouhal's data acquired for a rod with a diameter of 0.499 mm (see Figure 8).

Stowell and Deming [18] continued Strouhal's work by measuring the sound pressure distribution of the rotating rods. The data of the double-lobed pattern shown in Figure 9 was obtained at 2800 rpm with rods length of 0.4572 m. They also discovered that sound power can be related to the tip velocity and the length of the rod via

$$W_{vort} \sim U^{5.5} L,$$

where  $U$  is the tip velocity and  $L$  is the length of the rod.



**Figure 9 Polar distribution of sound pressure about rotating rod. Solid curve, observed; dotted curve, computed. [18]**

A number of measurement studies were performed after the publication of Lighthill's [2] aerodynamic theory in order to validate the theory. In most cases, sound power, correlation length, and oscillating forces were measured simultaneously. Leehey and Hanson [19] measured the sound radiated by a wire in a low-turbulence open jet

wind tunnel. They also measured the lift coefficient and the vibration forces. Leehey and Hanson's measured sound radiation result is within 3 dB of the theoretical prediction. Accordingly, the theoretical formula (Equation 3 in [19]) for sound radiated aerodynamically into a free space was verified in their study.

## **2.4 Lighthill Analogy**

In 1952, a paper named *on sound generated aerodynamically, I. General theory* by Dr. Michael James Lighthill was published. In this paper, he derived a set of formulas which were later named after him. Researchers in acoustics often regard the first appearance of his theory as the birth of aeroacoustics. Thereafter, aeroacoustics has become a branch of acoustics which studies the sound induced by aerodynamic activities or fluid flow. In 60 years of time, the theory of aeroacoustics has been greatly developed and widely applied in modern engineering fields.

The subject of Lighthill's paper is sound generated aerodynamically, a byproduct of an airflow and distinct from sound produced by vibration of solids. The general problem he discussed in the paper was to estimate the radiated sound from a given fluctuating fluid flow. There are two major assumptions. The first assumption is that the acoustic propagation of fluctuations in the flow is not considered. The second one is the preclusion of the back-reaction of the sound produced on the flow field itself. Therefore, the effects of solid boundaries are neglected. However, the back-reaction is only anticipated when there is a resonator (i.e. a cavity) close to the flow field. Accordingly, his theory is applicable to most engineering problems. Furthermore, his theory is confined in its application to subsonic flows, and should not be used to analyze the transition to supersonic flow.



Lighthill examined a limited volume of a fluctuating fluid flow in a very large volume of fluid. The remainder of the fluid is assumed to be at rest. He then compared the equations governing the fluctuations of density in the real fluid with a uniform acoustic medium at rest, which coincides with the real fluid outside the region of flow. A force field is acquired by calculating the difference between the fluctuating part and the stationary part. This force field is applied to the acoustic medium and then acoustic metrics can be predicted away from the source by solving Helmholtz equation. Helmholtz equation can be solved easily if a free field is assumed or can be solved using numerical simulation.

There are two significant advantages in this analogy as mentioned in his paper. First, since we are not concerned with the back-reaction of the sound on the flow, it is appropriate to consider the sound as produced by the fluctuating flow after the manner of a forced oscillation. Secondly, it is best to take the free system, on which the forcing is considered to occur, as a uniform acoustic medium at rest. Otherwise, it would be necessary to consider the modifications due to convection with the turbulent flow and wave propagation at different speeds within the, which would be difficult to handle. Using the method just described, an equivalent external force field is used to describe the acoustic source generation in the fluid [2].

#### **2.4.1 Development of Lighthill's Analogy**

The continuity and momentum equations for a fluid can be expressed as:

$$\frac{\partial \rho}{\partial t} + \frac{\partial}{\partial x_i} (\rho v_i) = 0 \quad \text{Equation 2-10}$$

$$\frac{\partial}{\partial t}(\rho v_i) + \frac{\partial}{\partial x_j}(\rho v_i v_j + p_{ij}) = 0 \quad \text{Equation 2-11}$$

Here  $\rho$  is the density,  $v_i$  is the velocity in the direction  $x_i$ .  $p_{ij}$  represents the compressive stress tensor.  $v_i$  and  $v_j$  are the velocity components in two directions.  $p_{ij}$  is expressed as below:

$$p_{ij} = -\sigma_{ij} + \delta_{ij} p \quad \text{Equation 2-12}$$

$$\sigma_{ij} = \mu \left( \frac{\partial v_i}{\partial x_j} + \frac{\partial v_j}{\partial x_i} \right) - \frac{2}{3} \mu \frac{\partial v_k}{\partial x_k} \delta_{ij} \quad \text{Equation 2-13}$$

where  $p$  is the static pressure of the flow field,  $\delta_{ij}$  is Kronecker's delta and  $\mu$  is the dynamic viscosity.

Now, eliminate the momentum density  $\rho v_i$  from the Equations 2-3 and 2-4 by subtracting the gradient of the momentum equation from the time derivative of the continuity equation. It is straightforward to obtain

$$\frac{\partial^2 \rho}{\partial t^2} = \frac{\partial^2}{\partial x_i \partial x_j} (\rho v_i v_j + p_{ij}) \quad \text{Equation 2-14}$$

where  $p_{ij}$  represents the pressure acting on the fluid.

Next, subtract  $c_0^2 \frac{\partial^2 \rho}{\partial x_i^2}$  from both sides of Equation 2-7, this results in

$$\frac{\partial^2 \rho}{\partial t^2} - c_0^2 \frac{\partial^2 \rho}{\partial x_i^2} = \frac{\partial^2}{\partial x_i \partial x_j} (\rho v_i v_j + p_{ij} - c_0^2 \rho \delta_{ij}) \quad \text{Equation 2-15}$$

where  $c_0$  is the characteristic speed of sound in the medium surrounding the flow region and the right hand side of this equation combined is called the source term which can be expressed as

$$T_{ij} = \rho v_i v_j + p_{ij} - c_0^2 \rho \delta_{ij} \quad \text{Equation 2-16}$$

and is referred to as the Lighthill's stress tensor.

It follows that the calculation of the aerodynamic sound can be accomplished by solving this equation for the radiation into a stationary, ideal fluid. The sound sources are a distribution of sources whose strength per unit volume is the Lighthill stress tensor  $T_{ij}$  [20].

The Lighthill stress tensor  $T_{ij}$  can be approximated as

$$T_{ij} \approx \rho_o v_i v_j \quad \text{Equation 2-17}$$

under the following conditions:

- Low Mach number – it can be assumed that velocity fluctuations are of order  $\rho_0 Ma^2$ ,
- Isentropic flow,
- High Reynolds number – it can be assumed that viscous effects are much smaller than inertial effects, and the viscous stress tensor is neglected because the Reynolds stresses  $\rho v_i v_j$  are much higher
- Viscous terms can be neglected since viscous terms in  $T_{ij}$  can be expressed as

$-\sigma_{ij} = \mu \frac{\partial v_i}{\partial x_j}$ , so that  $\frac{\partial^2 T_{ij}}{\partial x_i \partial x_j} = \mu \frac{\partial^3 v_i}{\partial x_j \partial x_i \partial x_j}$ , corresponding to an octupole

source (a very ineffective sound radiator) [21].

In the frequency domain, Lighthill's equation is written as [22]:

$$-\omega^2 \rho - a_0^2 \frac{\partial^2 \rho}{\partial x_i^2} = \frac{\partial^2 T_{ij}}{\partial x_i \partial x_j} \quad \text{Equation 2-18}$$

A transformed potential is then used so that the finite element formulation for the aeroacoustic analogy is compatible with the formulation for the acoustic wave propagation. Accordingly,

$$\rho = -\frac{i\omega\psi}{c^2} \quad \text{Equation 2-19}$$

where

$$a_0^2 = c^2 = \left( \frac{\partial p}{\partial \rho} \right)_s = \frac{\mathcal{P}}{\rho} \quad (\text{Stokesian perfect gas})$$

$\psi$  is a transformed variable [22] in the Helmholtz equation and  $\gamma$  represents the ratio of specific heats.

An alternative equation for Lighthill's analogy can be obtained by inserting Equation 2-19 to Equation 2-18:

$$\frac{\omega^2}{c^2} \psi + \frac{\partial^2 \psi}{\partial x_i^2} = \frac{1}{i\omega} \frac{\partial^2 T_{ij}}{\partial x_i \partial x_j} \quad \text{Equation 2-20}$$

Oberai et al. (2000) developed a variational formulation of Lighthill's analogy which can be expressed as:

$$\int_{\Omega} \frac{\omega^2}{c^2} \psi \delta\psi d\Omega + \int_{\Omega} \frac{\partial^2 \psi}{\partial x_i^2} \delta\psi d\Omega = \int_{\Omega} \frac{1}{i\omega} \frac{\partial^2 T_{ij}}{\partial x_i \partial x_j} \delta\psi d\Omega \quad \text{Equation 2-21}$$

where  $\delta\psi$  is a test function, and  $\Omega$  is the non-moving and non-deforming part of the computational domain.

By using Green's method, the weak form of the above equation is obtained:

$$\begin{aligned} & \int_{\Omega} \frac{\omega^2}{c^2} \psi \delta\psi d\Omega - \int_{\Omega} \frac{\partial \psi}{\partial x_i} \frac{\partial \delta\psi}{\partial x_i} d\Omega \\ & = \int_{\Omega} \frac{i}{\omega} \frac{\partial \delta\psi}{\partial x_i} \frac{\partial T_{ij}}{\partial x_j} d\Omega - \int_{\Gamma} \frac{\delta\psi}{i\omega} \frac{\partial}{\partial x_i} (c^2 \rho \delta_{ij} + T_{ij}) n_i d\Gamma \end{aligned} \quad \text{Equation 2-22}$$

and the above equation can be written as Equation 2-23 by using Equations 2-11 and 2-16:

$$\begin{aligned} & - \int_{\Omega} \frac{\omega^2}{\rho_0 c^2} \psi \delta\psi d\Omega - \int_{\Omega} \frac{1}{\rho_0} \frac{\partial \psi}{\partial x_i} \frac{\partial \delta\psi}{\partial x_i} d\Omega \\ & = \int_{\Omega} \frac{i}{\rho_0 \omega} \frac{\partial \delta\psi}{\partial x_i} \frac{\partial T_{ij}}{\partial x_j} - \int_{\Gamma} \frac{1}{\rho_0} F(\rho v_i n_i) d\Gamma \end{aligned} \quad \text{Equation 2-23}$$

## 2.5 CFD Turbulence models

### 2.5.1 $k - \varepsilon$ Turbulence Model

Because of the complexity of fluid turbulence, currently there is no single turbulence model which is valid for all turbulent phenomena. However, the  $k - \varepsilon$  model is widely used in industry due to its stability and convergence. The standard  $k - \varepsilon$  model used in ANSYS FLUENT was proposed by W. P. Jones and B. K. Launder, and a benchmark showing the acceptable performance of this model is discussed in *Lectures in Mathematical Models of Turbulence* [23].

The  $k - \varepsilon$  model is a semi-empirical turbulence model. The initial idea of developing this model was to improve the mixing-length hypothesis and to avoid prescribing the turbulence length scale algebraically. There are two equations in this model, the  $k$  equation and the  $\varepsilon$  equation.  $k$  represents turbulence kinetic energy and  $\varepsilon$  represents the dissipation rate. They can be obtained by solving the following transport equations [24]:

$$\frac{\partial(\rho k)}{\partial t} + \frac{\partial(\rho u_i k)}{\partial x_i} = \frac{\partial}{\partial x_i} \left[ \left( \mu + \frac{\mu_t}{\sigma_k} \right) \frac{\partial k}{\partial x_i} \right] + \mu_t \left( \frac{\partial u_i}{\partial x_j} + \frac{\partial u_j}{\partial x_i} \right) \frac{\partial u_i}{\partial x_j} - \rho \varepsilon \quad \text{Equation 2-24}$$

$$\frac{\partial(\rho \varepsilon)}{\partial t} + \rho u_k \frac{\partial k}{\partial x_k} = \frac{\partial}{\partial x_k} \left[ \left( \mu + \frac{\mu_t}{\sigma_\varepsilon} \right) \frac{\partial \varepsilon}{\partial x_k} \right] + \frac{c_1 \varepsilon}{k} \mu_t \frac{\partial u_i}{\partial x_j} \left( \frac{\partial u_i}{\partial x_j} + \frac{\partial u_j}{\partial x_i} \right) - c_2 \rho \frac{\varepsilon^2}{k} \quad \text{Equation 2-25}$$

where  $\mu_t$  is called turbulent viscosity and

$$\mu_t = c_\mu \rho k^2 / \varepsilon \quad \text{Equation 2-26}$$

The constants  $c_1, c_2, c_\mu, \sigma_k, \sigma_\varepsilon$  are respectively 1.44, 1.92, 0.09, 1.0, and 1.3. However, with the given values, the model is only suitable for high Reynolds flow, which works well if the flow is fully developed and is sufficiently spaced from wall boundaries. To improve the performance of the model in the near wall fields, wall functions can be used to model boundary effects.

### 2.5.2 $k - \omega$ model

The  $k - \omega$  turbulence model was first introduced by Kolmogorov in 1942 [25]. Similar to the  $k - \varepsilon$  turbulence model, the  $k - \omega$  turbulence model is also a two-equation turbulence model. The first turbulence parameter in this model is the kinetic energy term,

$k$ , which is also used in the  $k - \varepsilon$  model. Instead of using  $\varepsilon$ , the dissipation per unit mass,  $\omega$ , the dissipation per unit turbulence kinetic energy, was chosen as the second turbulence parameter. Since the introduction of the  $k - \omega$  turbulence model, it has been improved by several researchers. Nowadays, the most widely used  $k - \omega$  turbulence model is based on Wilcox et al.'s work [26] [27] [28].

In Wilcox's  $k-\omega$  turbulence model [29], eddy viscosity is expressed as:

$$\mu_T = \frac{\rho k}{\omega} \quad \text{Equation 2-27}$$

Turbulence kinetic energy and specific dissipation rate can be obtained by solving the following transport equations:

$$\rho \frac{\partial k}{\partial t} + \rho U_j \frac{\partial k}{\partial x_j} = \tau_{ij} \frac{\partial U_i}{\partial x_j} - \beta^* \rho k \omega + \frac{\partial}{\partial x_j} \left[ (\mu + \sigma^* \mu_T) \frac{\partial k}{\partial x_j} \right] \quad \text{Equation 2-28}$$

$$\rho \frac{\partial \omega}{\partial t} + \rho U_j \frac{\partial \omega}{\partial x_j} = \alpha \frac{\omega}{k} \tau_{ij} \frac{\partial U_i}{\partial x_j} - \beta \rho \omega^2 + \frac{\partial}{\partial x_j} \left[ (\mu + \sigma \mu_T) \frac{\partial \omega}{\partial x_j} \right] \quad \text{Equation 2-29}$$

where the closure coefficients are

$$\alpha = \frac{5}{9}$$

$$\beta = \frac{3}{40}$$

$$\beta^* = \frac{9}{100}$$

$$\sigma = \frac{1}{2}$$

$$\sigma^* = \frac{1}{2}$$

with the auxiliary relations

$$\epsilon = \beta^* \omega k$$

$$l = \frac{k^{\frac{1}{2}}}{\omega}.$$

The closure coefficients are used to replace unknown double and triple correlations with algebraic expressions involving known turbulence and mean-flow properties as proposed by Wilcox [29]. These values are determined based on experimental results.

The  $k - \omega$  turbulence model performs better at near wall layers than the  $k - \epsilon$  turbulence model, and has been successfully applied for flows with moderate adverse pressure gradients. However, it still has trouble dealing with pressure induced separation [30]. One major disadvantage of the standard  $k - \omega$  turbulence model is that the sensitivity of its  $\omega$  equation is strongly related to the values of  $\omega$  in the free stream outside the boundary layer [31]. Although the near wall performance is superior, this major flaw prevents the  $k - \omega$  turbulence model from replacing the  $k - \epsilon$  turbulence model [32]. This led to the development of the shear stress transport (SST)  $k - \omega$  turbulence model.

The SST  $k - \omega$  turbulence model [30] is a two equation eddy-viscosity model like the  $k - \epsilon$  model. The advantage of the shear stress transport (SST) formulation is that it combines both  $k - \epsilon$  and  $k - \omega$  turbulence models. When dealing with the free stream flow, the SST formulation will use the  $\epsilon$  behavior to avoid the excessive free stream sensitivity from which the original  $k - \omega$  turbulence model suffers. Furthermore, the advantage of the  $k - \omega$  turbulence model is preserved so the model works well close



to the wall. No extra damping is needed. The damping functions introduced to represent the viscous effects near a wall used in the  $k - \varepsilon$  model are well known to cause numerical stability problems, but these problems are avoided using SST models. The SST models have the following relations [33]:

$$\frac{D\rho k}{Dt} = \tau_{ij} \frac{\partial u_i}{\partial x_j} - \beta^* \rho \omega k + \frac{\partial}{\partial x_j} \left[ (\mu + \sigma_k \mu_t) \frac{\partial k}{\partial x_j} \right] \quad \text{Equation 2-30}$$

$$\begin{aligned} \frac{D\rho\omega}{Dt} = & \frac{\gamma}{\nu_t} \tau_{ij} \frac{\partial u_i}{\partial x_j} - \beta \rho \omega^2 + \frac{\partial}{\partial x_j} \left[ (\mu + \sigma_\omega \mu_t) \frac{\partial \omega}{\partial x_j} \right] \\ & + 2(1 - F_1) \rho \sigma_{\omega 2} \frac{1}{\omega} \frac{\partial k}{\partial x_j} \frac{\partial \omega}{\partial x_j} \end{aligned} \quad \text{Equation 2-31}$$

where

$$\phi = F_1 \phi_1 + (1 - F_1) \phi_2.$$

The constants of  $\phi_1$  are:

$$\begin{aligned} \sigma_{k1} = 0.85, \quad \sigma_{\omega 1} = 0.5, \quad \beta_1 = 0.0750, \quad \alpha_1 = 0.31 \\ \beta^* = 0.09, \quad \kappa = 0.41, \quad \gamma_1 = \frac{\beta_1}{\beta^*} - \frac{\sigma_{\omega 1} \kappa^2}{\sqrt{\beta^*}} \end{aligned}$$

The constants of  $\phi_2$  are:

$$\begin{aligned} \sigma_{k2} = 1.0, \quad \sigma_{\omega 2} = 0.856, \quad \beta_2 = 0.0828 \\ \beta^* = 0.09, \quad \kappa = 0.41, \quad \gamma_2 = \frac{\beta_2}{\beta^*} - \frac{\sigma_{\omega 2} \kappa^2}{\sqrt{\beta^*}} \end{aligned}$$

The eddy viscosity is defined as:

$$\nu_t = \frac{a_1 k}{\max(a_1 \omega; \Omega F_2)}.$$

Other definitions used in the formulation above are:

$$\tau_{ij} = \mu_t \left( \frac{\partial u_i}{\partial x_j} + \frac{\partial u_j}{\partial x_i} - \frac{2}{3} \frac{\partial u_k}{\partial x_k} \delta_{ij} \right) - \frac{2}{3} \rho k \delta_{ij}$$

$$F_1 = \tanh(\phi_1^4)$$

$$\phi_1 = \min \left[ \max \left( \frac{\sqrt{k}}{0.09\omega y}, \frac{500}{y^2\omega} \right); \frac{4\rho\sigma_{\omega 2}k}{CD_{k\omega}y^2} \right]$$

$$CD_{k\omega} = \max \left[ 2\rho\sigma_{\omega 2} \frac{1}{\omega} \frac{\partial k}{\partial x_j} \frac{\partial \omega}{\partial x_j}, 10^{-20} \right]$$

$$F_2 = \tanh(\phi_2^2)$$

$$\phi_2 = \max \left[ \frac{2\sqrt{k}}{0.09\omega y}, \frac{500\nu}{y^2\omega} \right].$$

Notice that the constants of  $\phi_2$  are the same as those in the k- $\epsilon$  turbulence model.

### 2.5.3 Large Eddy Simulation

The Large Eddy Simulation (LES) turbulence model is a “hybrid” approach. In LES, the large motions are directly computed but the small eddies are usually approximated using a model [34]. . It is the most widely used model in academia, but it is still not popular in industrial applications. One of the reasons is that the near wall region needs to be represented with an extremely fine mesh not only in the direction perpendicular to the wall but also parallel with the wall. For this reason, LES is not recommended with flows with strong wall boundary effects. In other words, the flow should be irrelevant to the wall boundary layers. Another disadvantage of the LES turbulence model is the excessive computational power needed due to the statistical stability requirement. Generally, the LES solver requires long computational times to

reach a statistically stable state. Therefore, a substantially long preparation time is needed for a successful run of LES.

The main idea of the LES formulation is to separate the Navier-Stokes equations into two parts, a filtered part and a residual part. Filtering in LES is a mathematical operation separates a range of small scales from the Navier-Stokes equations solution. The large scale motions are resolved in the filtered part while the small scale motions are modeled in the residual part. The large scale motions are strongly influenced by the geometry and boundary conditions. The small scale motions are determined by the rate of energy transport from large-scale eddies and viscosity [35]. Well documented explanations of filtered Navier-Stokes equations can be found in many turbulence modeling textbooks, and the subgrid-scale (SGS) turbulence model is used to model the near-wall regions.

Using the SGS model, the SGS stress can be found using [36]:

$$\tau_{ij} - \frac{1}{3}\tau_{kk}\delta_{ij} = -2\mu_t\bar{S}_{ij} \quad \text{Equation 2-32}$$

where  $\mu_t$  represents the SGS turbulent viscosity and  $\bar{S}_{ij}$  is the rate-of-strain tensor for the resolved scale defined by:

$$\bar{S}_{ij} = \frac{1}{2}\left(\frac{\partial\bar{u}_i}{\partial x_j} + \frac{\partial\bar{u}_j}{\partial x_i}\right). \quad \text{Equation 2-33}$$

In the Smagorinsky-Lilly formation, the turbulent viscosity has the following representation [35]:

$$\mu_t = \rho L_s^2 |\bar{S}| \quad \text{Equation 2-34}$$

$$|\bar{S}| = \sqrt{2\bar{S}_{ij}\bar{S}_{ji}} \quad \text{Equation 2-35}$$

where  $L_s$  is the mixing length for subgrid scales and is computed as:

$$L_s = \min\left(\kappa d, C_s V^{\frac{1}{3}}\right)$$

where

$$\kappa = 0.42$$

and

$d$  distance to the closest wall

$C_s$  Smagorinsky constant

$V$  volume of the computational cell.

## 2.6 Acoustic FEM

### 2.6.1 Introduction

There are two major types of numerical methods in acoustics: the boundary element method (BEM) and finite element method (FEM). Although noise control engineering primarily depends on measurement and experience, numerical methods have been used to predict noise in the early design stage as a means to lower the cost of design by increasing design efficiency [37]. Normally, acoustic FEM is used to solve interior problems, but nowadays FEM can be used to solve acoustic radiation problems with the advent of infinite elements.

The Helmholtz equation is the governing equation for linear acoustics and can be expressed as

$$\nabla^2 p + k^2 p = 0 \quad \text{Equation 2-36}$$

where  $p$  is the sound pressure and  $k$  is the wavenumber.

Multiply Equation 2-36 by a weighting function  $w_L$  and integrate the resulting equation by parts. Then, the weak form of the linear Helmholtz equation can be expressed as

$$-\int_V (\nabla w_L \cdot \nabla p) dV + \int_V (w_L k^2 p) dV + \int_S \left( w_L \frac{\partial p}{\partial n} \right) dS = 0 \quad \text{Equation 2-37}$$

By applying the natural and general natural boundary conditions, Equation 2-30 becomes

$$-\int_V (-\nabla w_L \cdot \nabla p + w_L k^2 p) dV + \int_{S_1} \left( w_L \frac{\partial p}{\partial n} \right) dS_1 \quad \text{Equation 2-38}$$

$$-\int_{S_2} i\rho\omega w_L v_n dS_2 - \int_{S_3} i\rho\omega \frac{1}{Z} w_L p dS_3 = 0$$

According to the Galerkin approach,  $p$  and  $w_L$  can be approximated by using a linear combination of shape functions  $N_i$  and  $W_L$ :

$$p = [N]\{P\} \quad \text{Equation 2-39}$$

$$w_L = [N]\{W_L\} \quad \text{Equation 2-40}$$

By substituting  $p$  and  $w_L$  into equation 2-38, the finite element equation can be expressed as

$$\left( \int_V \nabla[N] \cdot \nabla\{N\}dV + i\rho\omega \int_{S_3} \frac{1}{Z} [N]\{N\}dS_3 - \frac{\omega^2}{c^2} \int_V [N]\{N\}dV \right) \{p\} = -i\rho\omega \int_{S_3} [N]\{v_n\}dS_3 \quad \text{Equation 2-41}$$

### 2.6.2 Infinite Element

An infinite element is a finite element that covers a semi-infinite sector of space [38]. It was developed in the interest of solving radiation problems. The solution of the wave equation using infinite elements is based on multipole expansion. The method used in ACTRAN is reviewed in this chapter. More detailed information can be found in ACTRAN User's Guide Volume 1.

Consider the convected wave equation in the local coordinate system  $(x'_1, x'_2, x'_3)$ :

$$\Delta\psi - 2ikM \frac{\partial\psi}{\partial x'_1} - M^2 \frac{\partial^2\psi}{\partial x'^2_1} + k^2\psi = 0 \quad \text{Equation 2-42}$$

The above equation can be further simplified to the Helmholtz equation using Prandtl-Glauert transformation. The resulting equation is expressed as follows:

$$\Delta\bar{\psi} + \bar{k}^2\bar{\psi} = 0, \quad \text{Equation 2-43}$$

where

$$\bar{k} = \frac{k}{\beta}$$

$$\lambda = \frac{kM}{\beta}$$

$$\bar{\psi} = \psi e^{-i\lambda x_1''}.$$

The solution of the equation can be expanded in the following form according to the Wilcox-Atkinson theorem from outside an ellipsoidal surface in the transformed coordinate system:

$$\bar{\psi}(r'', \theta'', \varphi'') = e^{-i\bar{k}r''} \sum_{n=1}^{\infty} \frac{\bar{F}_n(\theta'', \varphi''; \bar{k})}{r''^n} \quad \text{Equation 2-44}$$

where  $(r'', \theta'', \varphi'')$  represents the coordinates in the transformed system.

A conjugated infinite element which comes from Equation 2-37 is expressed as:

$$\psi(x'; k) = e^{-i\bar{k}(r'' - Mx_1'')} \sum_{n=1}^{\infty} \frac{\bar{F}_n(\theta'', \varphi''; \bar{k})}{r''^n} \quad \text{Equation 2-45}$$

The interpolation function is:

$$\psi(\xi; k) = \sum_{i=1}^N N_i(\xi; k) \psi_i \quad \text{Equation 2-46}$$

where

$$N_i(\xi; k) = P_i(\xi) e^{-ik\mu(\xi)}. \quad \text{Equation 2-47}$$

$P_i$  are polynomial interpolation functions and  $\mu$  is:

$$\mu(\xi) = \frac{r''(\xi) - r_b''(\xi) - M(x_1''(\xi) - x_{b1}''(\xi))}{\beta} \quad \text{Equation 2-48}$$

An additional scaling factor is introduced in order to ensure the integrability of basic element matrices:

$$\delta\psi_i(\xi) = W(\xi)N_i^*(\xi; k) \quad \text{Equation 2-49}$$

$N_i^*$  represents the complex conjugate and the scaling factor  $W(\xi)$  is given by:

$$W(\xi) = \left(\frac{r_b''}{r''}\right)^2 \quad \text{Equation 2-50}$$

The coefficients of matrices  $\mathbf{K}^{\infty,e}$ ,  $\mathbf{C}^{\infty,e}$ ,  $\mathbf{M}^{\infty,e}$  are given by:

$$\mathbf{K}_{ij}^{\infty,e} = \int_{\Omega^{\infty,e}} \frac{\rho_\infty}{\rho_T^2} (\nabla Q_i \cdot \nabla P_j - (\nabla Q_i \cdot \mathbf{M})(\nabla P_j \cdot \mathbf{M})) d\Omega^{\infty,e} \quad \text{Equation 2-51}$$

$$\begin{aligned} \mathbf{C}_{ij}^{\infty,e} = \int_{\Omega^{\infty,e}} \frac{\rho_\infty}{\rho_T^2 a_\infty} (Q_i(\nabla\mu + (1 - \mathbf{M} \cdot \nabla\mu)\mathbf{M}) \cdot \nabla P_j \\ - P_j(\nabla\mu + (1 - \mathbf{M} \cdot \nabla\mu)\mathbf{M}) \cdot \nabla Q_i) d\Omega^{\infty,e} \end{aligned} \quad \text{Equation 2-52}$$

$$\begin{aligned} \mathbf{M}_{ij}^{\infty,e} = \int_{\Omega^{\infty,e}} \frac{\rho_\infty}{\rho_T^2 a_\infty^2} Q_i P_j (1 - \nabla\mu \cdot \nabla\mu + (\mathbf{M} \cdot \nabla\mu)(\mathbf{M} \cdot \nabla\mu) \\ - 2(\mathbf{M} \cdot \nabla\mu)) d\Omega^{\infty,e} \end{aligned} \quad \text{Equation 2-53}$$



## **Chapter 3**

### **Simulation Approach**

#### **3.1 Introduction**

Usually in an aeroacoustic problem, there are four aspects to consider: the sound wave and the acoustic medium, sources, and the receiver [39]. The medium in aeroacoustic problems is air or a gas mixture. The sources are the pressure fluctuations due to vortex shedding and turbulence. The receiver can be microphones (or field points in a simulation) or, in reality, the human ears.

There are three primary aeroacoustic simulation approaches: computational aeroacoustics (CAA), CFD-sound propagation solver coupling, and broadband noise source models.

##### **3.1.1 Computational Aeroacoustics**

Computational aeroacoustics (or direct noise simulation) refers to when sound sources and sound wave propagation are solved in a single comprehensive model. In this case, computational fluid dynamics is used to solve the sound generation and the sound wave propagation because they both follow the Navier-Stokes equations.

The advantages of the CAA approach are that: 1) sound generation and sound wave propagation are solved in one simulation, and 2) acoustic pressure fluctuations can affect the flow. However, there are disadvantages that prevent CAA from being used in practice. First of all, the entire acoustic domain of interest must be included in the CFD mesh. However, the acoustic receive is often a large distance away from the flow source.

This would require a very large mesh. Secondly, the procedure is computationally expensive since it requires finer meshes, long transient computations in the statistical steady state, and pressure scale limits.

### **3.1.2 CFD-Sound Propagation Solver Coupling**

CFD-sound propagation solver coupling works differently from CAA. In this method, the problem is separated in two parts: (1) sound generation and (2) sound wave propagation. In order to obtain the sound generated, a transient CFD simulation is performed first. Then the CFD simulation result is imported to a wave equation solver (acoustic finite or boundary element analysis) to determine the sound sources.

Some major advantages of the CFD-sound propagation solver coupling include: 1) a much smaller CFD domain restricted to the source region can be used which will greatly reduce the computational effort, and 2) far-field sound wave propagation can be obtained by utilizing the wave equation solver. For example, in FFT ACTRAN, by applying the infinite element boundary condition, the far-field sound pressure and sound power can be easily obtained without needing a detailed CFD model which includes the source region and the receiver.

The obvious disadvantage is that the effect of sound on flow is ignored and sometimes the effect of sound on flow can be vital. In addition, the geometric scales of the sound generation and transmission should be largely different in order to get a valid simulation result.

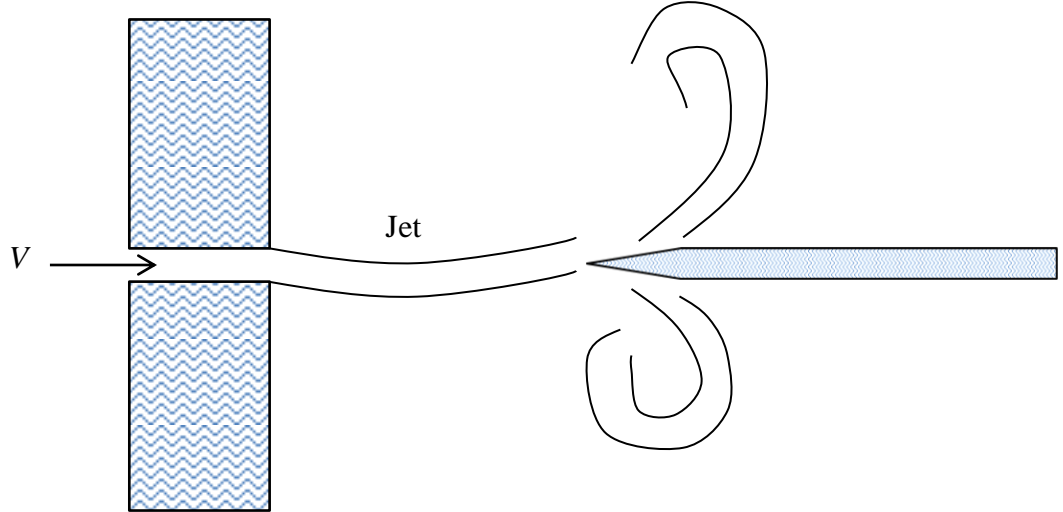
### **3.1.3 Broadband Noise Sources Models**

It is well known that the Transient CFD solutions are CPU intensive. However, if no specific tones are expected, broadband noise sources models can be utilized and the transient CFD solution can be avoided. Instead, only a steady state CFD solution is required. With the help of analytical models such as Lilley's acoustic source strength broadband noise model [40], the strength of the sound sources can be obtained with good accuracy. Those sound sources can be applied directly to an acoustic BEM or FEM model.

## **3.2 General Assumptions**

### **3.2.1 Model Dimension**

The models used in this thesis are all 2-D models. Studies have shown that 2-D models for symmetric geometry work well in aeroacoustic simulations. Takahashi et al. [41] have shown that identical results can be obtained using 2-D and 3-D models for the edge tone problem (see Figure 10). The peaks in acoustic frequency spectrum compare especially well between both 2-D and 3-D models. They have concluded that the 2-D approximation is adequate for determining the tones due to flow noise. Additionally, Rubio et al. [42] has performed an aeroacoustic simulation of a 2-D expansion chamber, and found that phenomenon that could be modeled in 2-D governed the tonal noise. However, a 3-D model was necessary to accurately predict the broadband noise due to turbulence.



**Figure 10 Edge tone [41]**

### **3.2.2 Fluid Compressibility**

The CFD calculation can be performed by solving either incompressible or compressible Navier-Stokes equations. The appropriate assumption depends on both the Mach number and the specific physical situation. The Lighthill's tensor is then calculated from the velocity and density fields obtained from an appropriate CFD calculation. Layton and Novotny [43] have pointed out that for flows in the low Mach number regimes (below 0.3 according to Wilcox [44]), the direct simulations are often costly, unstable, inefficient and unreliable, mainly due to the high frequency content in the equations. An efficient way to improve the simulation is to use incompressible models at low Mach numbers. For instance, Wang et al. [45] have concluded that at low Mach numbers, incompressible flow solutions are sometimes adequate. However, there is no

agreed Mach number threshold for CFD solutions aimed at identifying aeroacoustic sources.

### **3.2.3 Interactions and Feedbacks**

Fluid-structure interaction is the interaction of some movable or deformable structure with an internal or surrounding fluid flow [46]. One infamous example of this type of interaction is the failure of the Tacoma Narrows Bridge in 1940. In aeroacoustics, this type of interaction is often disregarded because of the complexity of structure and fluid solver coupling.

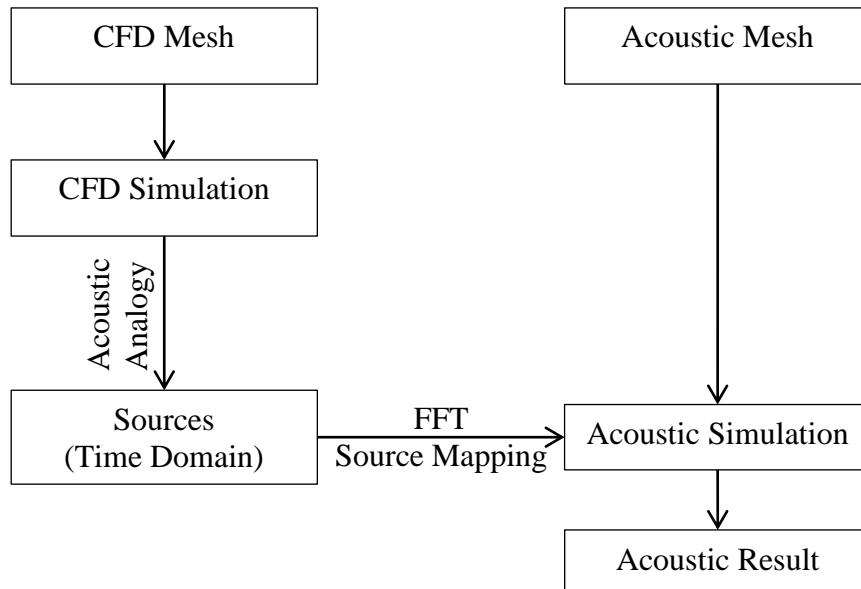
There is no fluid-structure interaction considered in this thesis though the fluid-structure interaction can be vital in certain cases such as the vibration of fan blades and flow over cylinders. This kind of interaction is more likely to occur when the frequency of turbulence is close to the natural frequency of the structure and therefore generates sound in greater amplitude. In this thesis, we focus on the sound generated by fluid flow only and therefore we assume all structures are perfectly rigid.

Aeroacoustic feedback occurs when the sound wave generated from the fluid flow positively affects the flow field and therefore establishes a self-excited system. This aeroacoustic feedback loop plays an important role in certain cases such as flow over a cavity and flow at a sharp edge, and will cause an increase in the sound amplitude. However, most CFD solvers are unable to model this interaction due to the difference in scales. There are orders of magnitude difference in pressure and velocity between CFD and acoustics. For example, the acoustic wave in air travels at 343 m/s under normal conditions while low sub sonic flow is at least two orders of magnitude lower. Typically,

CFD solvers have inherent dissipation to ensure stability and are therefore unable to handle these interactions.

### **3.3 CFD-Sound Propagation Solver Coupling Process**

The aeroacoustic simulation in a CFD-sound propagation solver coupling process is based on variables such as the pressure and density fields computed by a CFD solver during transient flow simulation. Figure 11 shows the solution process of this solver coupling approach. The aeroacoustic solver will read in the transient CFD solution data and compute the aeroacoustic sources in the time domain. Then a Fast Fourier Transform is conducted in order to obtain the source data in the frequency domain. After the frequency domain sources are computed, an acoustic simulation can be performed.

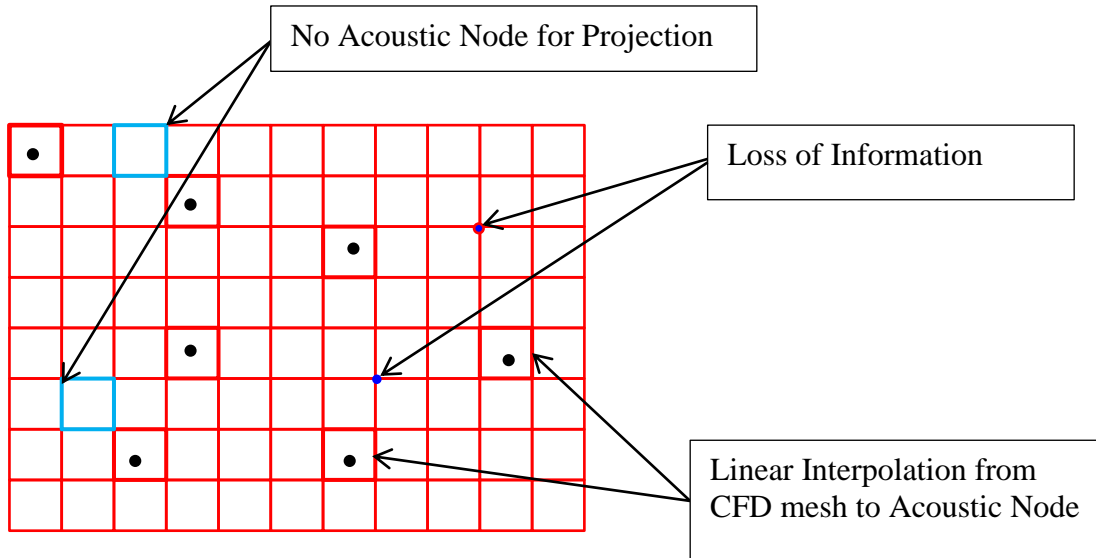


**Figure 11 CFD-Sound Propagation Solver Coupling Solution Process**

### 3.3.1 Comments on Source Mapping

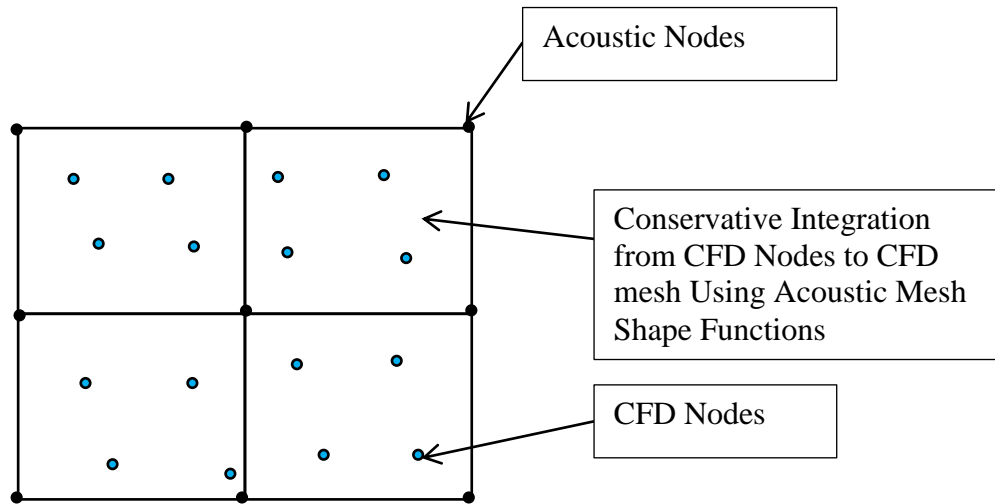
Two methods are available to accomplish the source mapping from the CFD domain to the acoustic domain: 1) linear interpolation and 2) conservative integration.

In linear interpolation, all nodal coordinates' acoustic values are sampled in the CFD mesh, and are projected to the closest node on the acoustic mesh. Loss of information may occur during this process if the acoustic mesh is coarser than the CFD mesh (Figure 12).



**Figure 12 Linear Interpolation Source Projection Method**

Conservative integration overcomes this difficulty. The aeroacoustic field is integrated using the shape functions of the acoustic mesh. Accordingly, all aeroacoustic sources are preserved (Figure 13).



**Figure 13 Conservative Integration Source Projection Method**

### **3.4 Fast Fourier Transform for Aeroacoustic Simulation**

The acoustic simulation is in the frequency domain, while the CFD transient solution is in time domain. Hence, aeroacoustic sources computed from the CFD solution must be transformed to the frequency domain using a Fast Fourier Transform. The Fast Fourier Transform follows the general FFT rules including the Nyquist requirement. Thus, the time step size and number of samples in time domain will affect the frequency resolution in frequency domain.

#### **3.4.1 Determine Time Step Size and Number of Time Steps for CFD Simulation**

Before the CFD simulation, the maximum frequency of the aeroacoustic result, sampling frequency should be set to the maximum frequency of interest. Additionally, if tones are expected, the sampling frequency needs to be at least 10 to 20 times greater



than the highest frequency of the tones of interest. Accordingly, the time step size of the CFD simulation can be obtained using the following relation,

$$\text{Number of Time Steps} = \frac{2 \times \text{Sampling Frequency}}{\text{Frequency Resolution}} \quad \text{Equation 3-1}$$

$$\text{Time Step Size} = \frac{1}{2 \times \text{Sampling Frequency}} \quad \text{Equation 3-2}$$

Notice that sampling frequency is multiplied by 2 due to the Nyquist requirement.

### **3.5 Wall Boundary Meshing Requirements**

A successful CFD simulation often requires a CFD mesh with great quality. It is essential to have a mesh representing the shape of the geometry accurately. Additionally, the near wall region needs to be handled with care because turbulent flows are largely affected by the presence of the wall boundaries where rapid changes of flow variables such as pressure gradients take place. In the modeling process, the dimensionless wall distance ( $y^+$ ) is often used in the estimation of the actual boundary thickness and can be used to guide the selection of an appropriate near wall treatment.  $y^+$  can be read as the ratio of the turbulent and laminar effects in a cell.

A dimensionless wall distance is defined by the following formula:

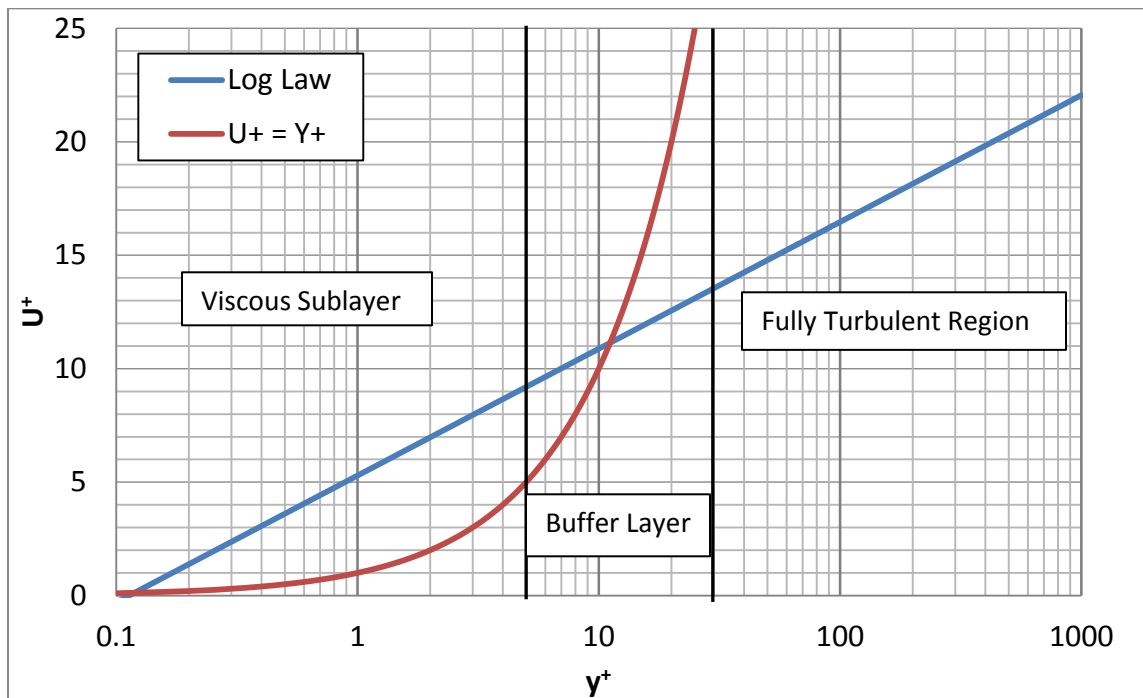
$$y^+ = \frac{u_* y}{\nu} \quad \text{Equation 3-3}$$

where

- $u_*$  friction velocity (shear velocity) at the closest wall
- $y$  distance to the closest wall
- $\nu$  local kinematic viscosity of the fluid

Figure 14 shows the divisions of the near wall region. The near wall region can be further divided into three sub layers:

- $y^+ < 5$                       Viscous Sublayer (laminar flow)
- $5 < y^+ < 30$                 Buffer Layer (neither laminar or turbulent)
- $y^+ > 30$  to 60                Fully Turbulent Region (Log Law Region)



**Figure 14 Divisions of Near-wall Region**

It is desirable that  $y^+ \approx 30$  for wall-bounded turbulent flows and  $y^+ \approx 1$  for near-wall modeling [47].

### 3.6 Scaling of Acoustic Result

#### 3.6.1 Sound Power Scaling Laws

To simplify the aeroacoustic modeling process, 2-D models are often selected over 3-D models whenever the flow field is symmetric. However, the sound pressure result or sound power result obtained from a 2-D simulation should be scaled.

The sound power radiated due to a monopole is

$$\bar{W} = \frac{\rho_0 c k^2}{4\pi} Q^2 \quad \text{Equation 3-4}$$

where  $Q$  is the volume velocity and

$$Q \propto U d^2$$

where  $U$  is the speed and  $d$  is the diameter.

By inserting the Strouhal frequency (Equation 2-9) into Equation 3-5, it can be seen that

$$\bar{W} \propto \rho_0 d^2 U^4 / c \quad \text{Equation 3-5}$$

In a similar fashion, the sound power radiated by a dipole and quadrupole in a 3-D field, following relations can be expressed as

$$\text{Dipole: } \bar{W} = \rho_0 d^2 U^6 / c^3 \quad \text{Equation 3-6}$$

$$\text{Quadrupole: } \bar{W} = \rho_0 d^2 U^8 / c^5 \quad \text{Equation 3-7}$$

Table 1 shows the scaling laws for sound power in sound fields with different dimensions [9]. Notice that the sound power in 2-D is the 1-D sound power scaled by the

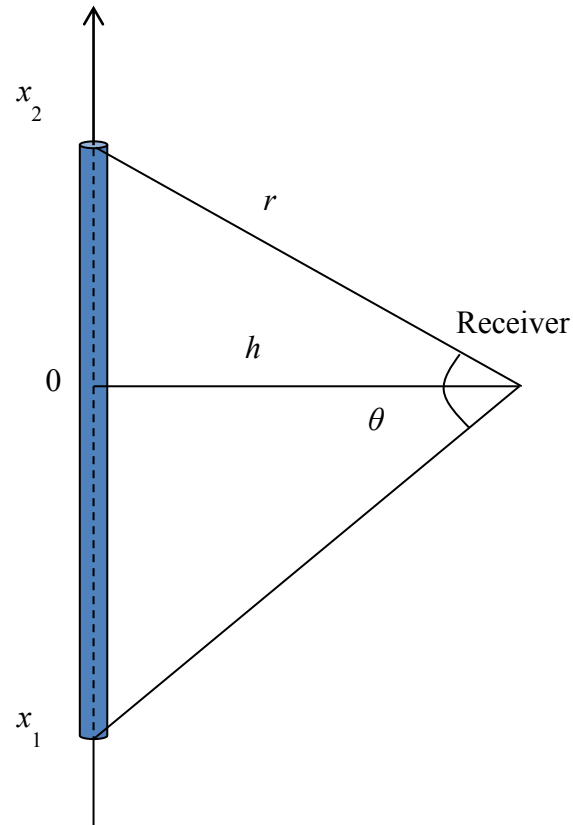
Mach number for a monopole, dipole, and quadrupole. Similarly, the sound power in 3-D is the 2-D sound power scaled by the Mach number.

**Table 1 Scaling Laws for Sound Power in Sound Fields with Different Dimensions**

<b>Dimension</b>	<b>Monopole</b>	<b>Dipole</b>	<b>Quadrupole</b>
<b>1-D</b>	$\rho_0 c d^2 U^2$	$\rho_0 d^2 U^4 / c$	$\rho_0 d^2 U^6 / c^3$
<b>2-D</b>	$\rho_0 d^2 U^3$	$\rho_0 d^2 U^5 / c^2$	$\rho_0 d^2 U^7 / c^4$
<b>3-D</b>	$\rho_0 d^2 U^4 / c$	$\rho_0 d^2 U^6 / c^3$	$\rho_0 d^2 U^8 / c^5$

### **3.6.2 Finite Length Scaling**

A 2-D simulation assumes that the sound source has infinite length in the direction perpendicular to the computational domain. However, in the physical situation, the computational domain has a finite length. To properly scale the sound power or sound pressure result, the contribution of the source region with finite length needs to be extracted from the original result. The scaling law for this situation can be derived from a line source (Figure 15).



**Figure 15 Line Source [9]**

Assuming that the sound power radiated per unit length of the line source is  $\overline{W}$ .

The sound pressure at the receiver's location can be calculated by the following equation:

$$P_{line}^2 = \frac{\rho_0 c \overline{W}^2 \theta}{4\pi h} \quad \text{Equation 3-8}$$

where  $c$  is the speed of sound and  $\rho_0$  is the density of air.  $h$  and  $\theta$  are defined in Figure 15.

There are two steps resulting sound pressure or power from 2-D to 3-D. The first step is to apply the rules in Table 1. After that, the line source rule should be used to obtain the acoustic result in finite 3-D domain.

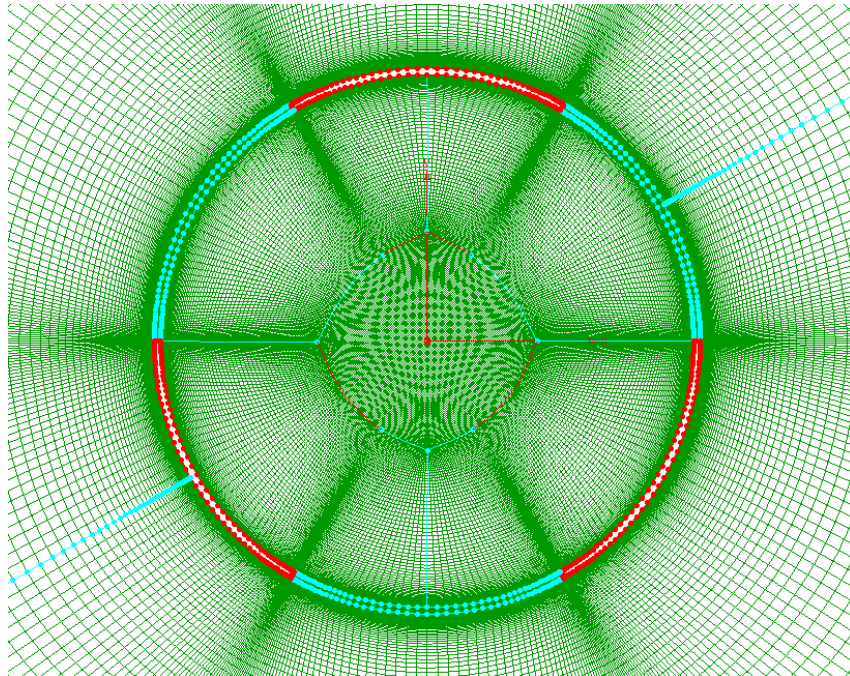
## Chapter 4

### Verification of Simulation Approach

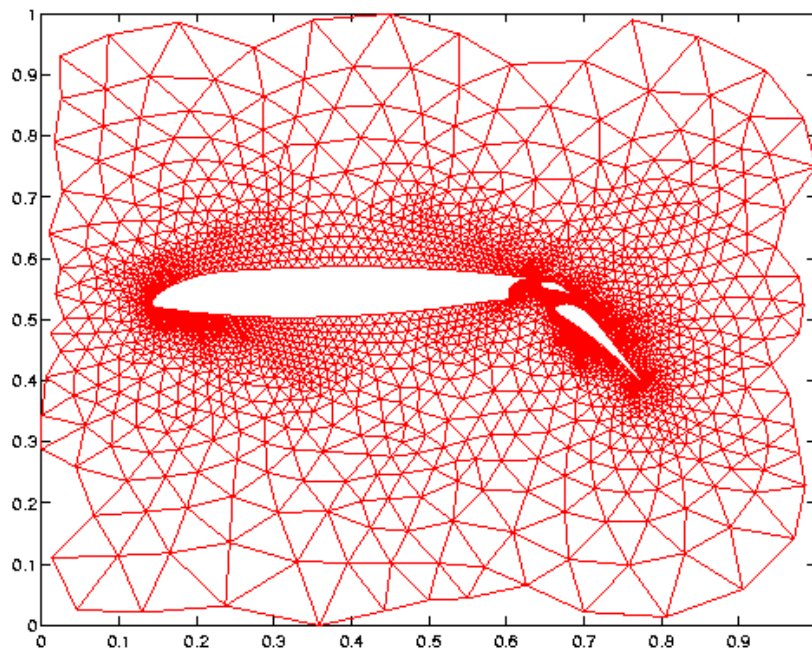
#### 4.1 Lid-Driven Test Case for Mesh Selection

##### 4.1.1 CFD Mesh Types

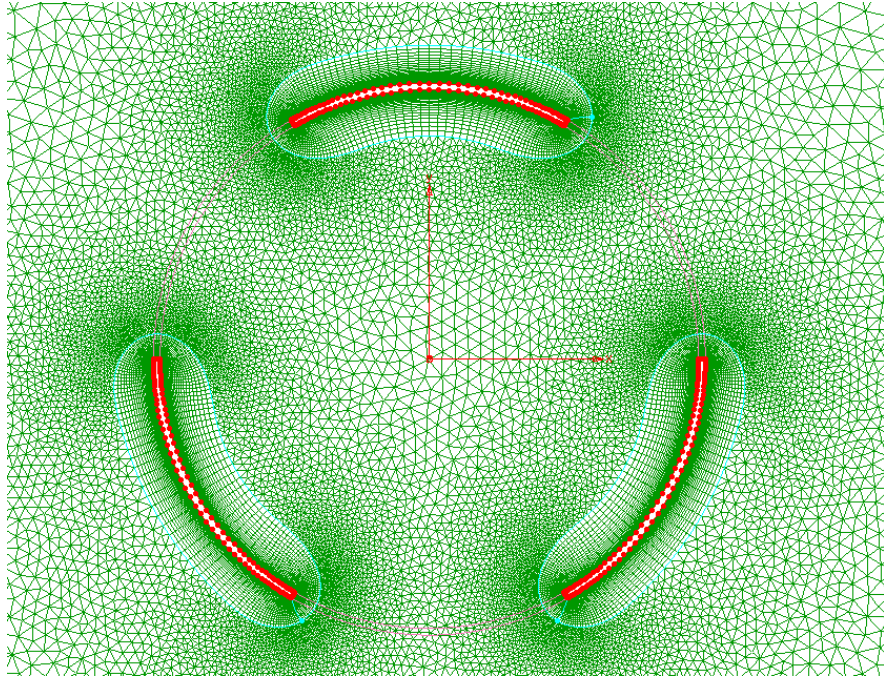
There are three types of mesh strategies used in CFD simulations: structured meshes, unstructured meshes, and hybrid meshes. A mesh is called structured if the node connectivity has a fixed pattern. Structured meshes are usually easy to generate for regular geometries (see Figure 16). A mesh is unstructured if the connectivities of the nodes are irregular. More space is required to store the unstructured mesh because there is no fixed pattern neighborhood connectivity (see Figure 17). An unstructured mesh usually requires less effort as it can be generated using automatic meshers. A “hybrid” mesh is a combination of both structured and unstructured domains. Figure 18 shows an example where the area close to the blades is represented with a structured mesh while the regions away from the blades are unstructured. The advantage of a hybrid mesh is that a structured mesh can be used in regions where more detail and accuracy are needed whereas a coarser unstructured mesh is viable away from the blades.



**Figure 16 An Example of Structured Mesh [48]**



**Figure 17 Unstructured Mesh around a NASA Airfoil (Matlab Demo)**



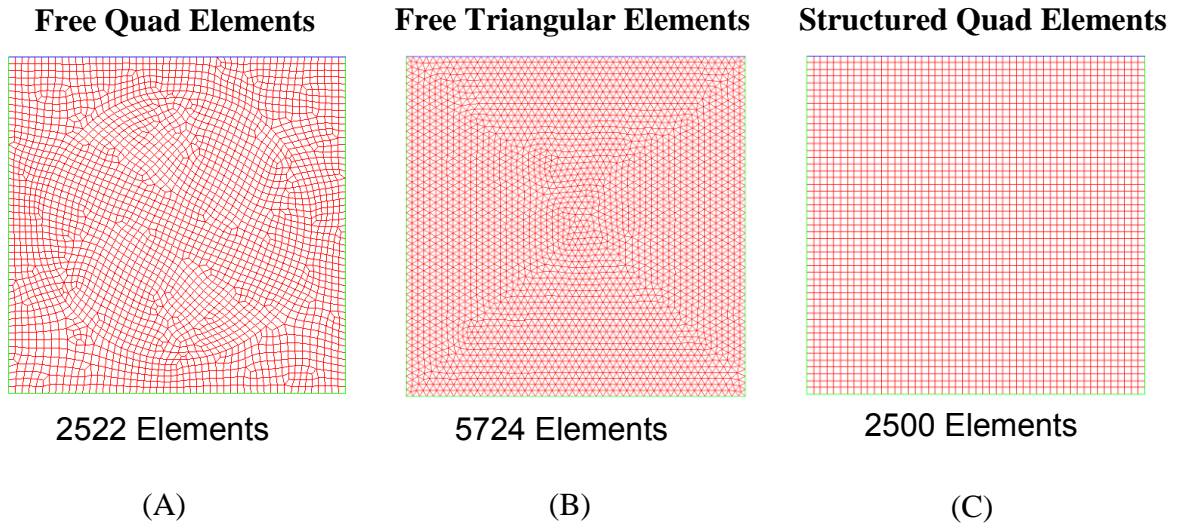
**Figure 18 An Example of Hybrid Mesh [48]**

#### **4.1.2 Lid-Driven Case Meshes**

The lid-driven problem has been used as a test case for CFD codes since the early work by Burggraf [49]. To better understand the effects of different mesh strategies on solution time and accuracy, a lid-driven case study was conducted. Three different mesh strategies were considered: free quad elements (Figure 19(a)), free triangular elements (Figure 19(b)), and structured quad elements (Figure 19(c)). The area of the domain is  $1 \text{ m} \times 1 \text{ m}$ . There are 2522 quad elements generated by the automatic mesher in the free quad mesh. The same distance between nodes was used in the free triangular mesh that was used in the free quad mesh. Thus, there are twice as many elements generated using a free triangular mesh. The structured quad elements were generated by using a mapped mesh. Since the domain is a square, it is easy to divide each side by the same number of



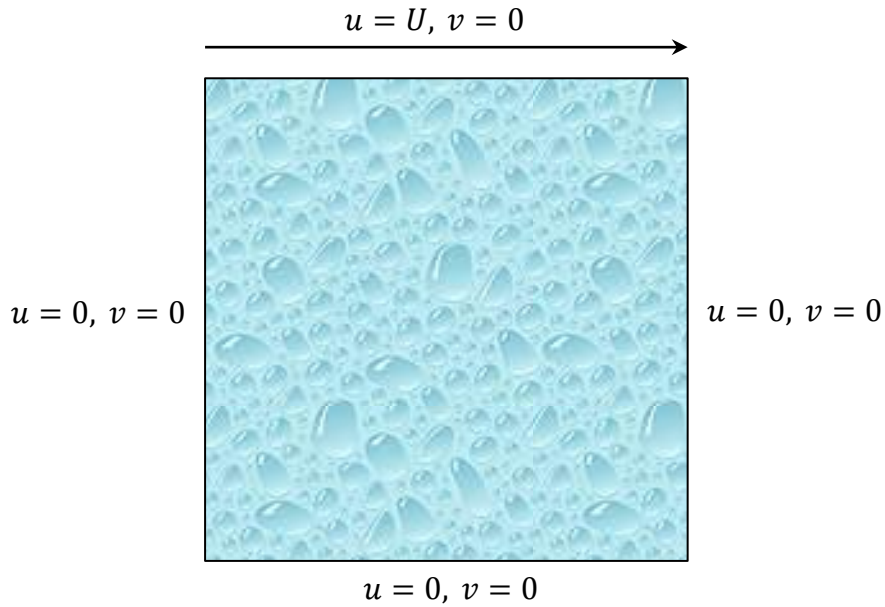
divisions. In this case, there are 50 divisions on each side making a total of 2500 structured quad elements.



**Figure 19 Meshes Used in Lid-Driven Case**

### **4.1.3 CFD Simulation Setup**

The standard lid-driven problem is a 2-D square domain with fluid and Dirichlet boundary conditions. A Dirichlet boundary condition specifies the values of the solution on the boundary of the computational domain of an ordinary or a partial differential equation. Figure 20 shows the boundary conditions of the case studied. Three out of the four sides of the square domain are stationary, and there is only one side moving.  $u$  represents the horizontal velocity and  $v$  represents the vertical velocity. For the case shown here, the horizontal velocity of the lid ( $u$ ) is 1 m/s.



**Figure 20 Boundary Condition of the Lid-Driven Case**

The fluid used in this simulation was selected to have a density  $\rho = 1 \text{ kg/m}^3$ , and a dynamic viscosity  $\mu = 0.001 \text{ kg/ms}$ . The reason for choosing these values is to achieve a Reynolds number of 1000 at the moving wall. The lid-driven case at this Reynolds number has been well studied numerically by Ghia et al. [50].

At a Reynolds number of 1000, the flow is laminar. Therefore, a laminar viscous model is used and the steady state solution is obtained.

Scaled residuals can be good indicators of the convergence of a solution. In a typical ANSYS FLUENT simulation case, there are three types of residuals: continuity, velocity and solver specific residuals. If a computer has an infinite precision, the residuals will reach zero eventually. However, in reality, computers have finite precision. For a double precision computer, the residual can drop up to 12 orders of magnitude. A recommended criterion of scaled continuity and velocity residual is  $10^{-3}$  [6].

The convergence criteria in this study are as follows:

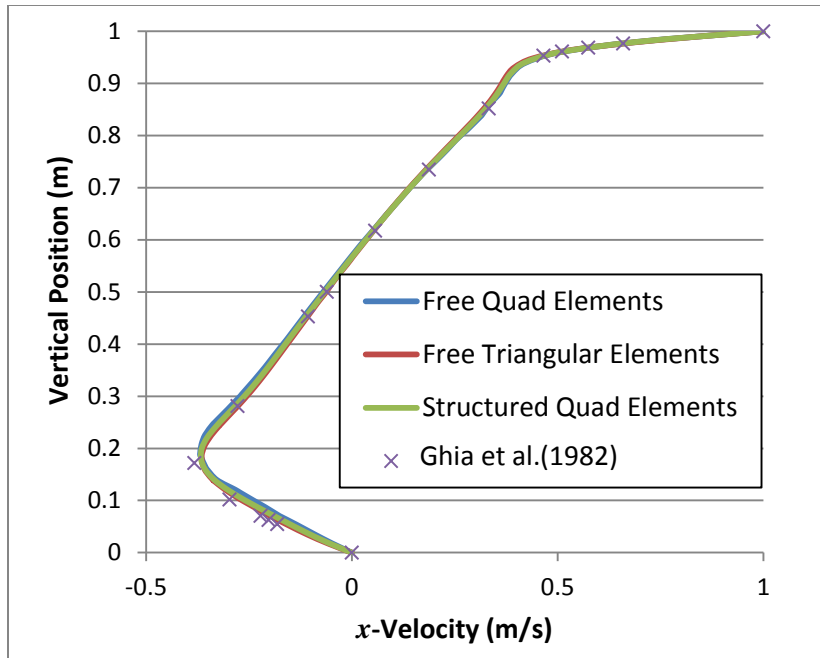
Continuity Residual  $< 10^{-6}$ ;

Velocity Residual  $< 10^{-3}$ .

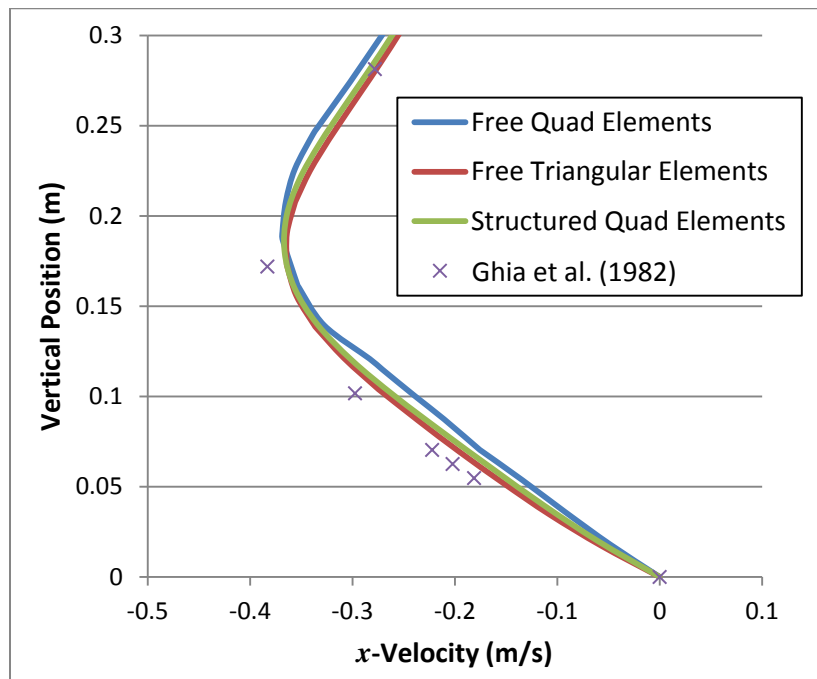
#### **4.1.4 Result and Discussion**

Figures 21 and 22 show the  $x$ -component of the velocity at the vertical center line of the domain from the bottom to the top of the domain. The results are compared to the results of Ghia et al. [50]. Figure 21 shows the solution at the centerline while Figure 22 zooms in at the vertical position of 0.2 m.

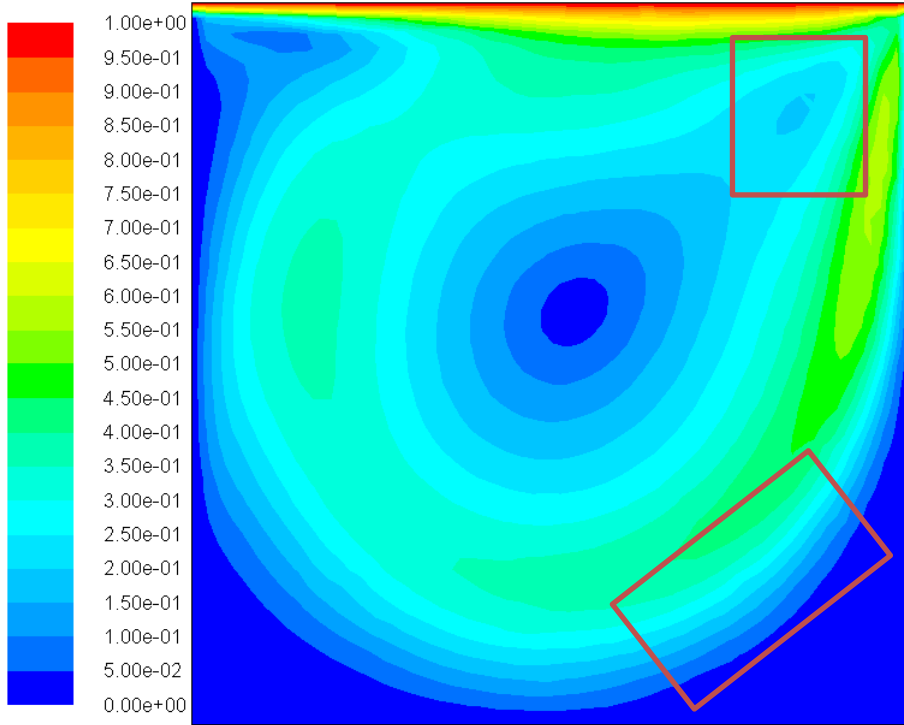
The results from each of the three mesh strategies compare well to the previous study which was obtained through a CFD simulation as well as can be seen from Figure 21 and Figure 22. Similarly, contour plots are shown in Figure 23 and Figure 24. However, the difference is not significant. Since the results are nearly identical, it is important to take a look at solution time. Both free and structured quad elements converge in half the time as a mesh consisting of triangular elements. Figure 25 compares the continuity residual for the three meshes. Notice that the residual decreases much more rapidly for both quad meshes. Similarly, the friction coefficient converges in approximately half the number of iterations (Figure 26).



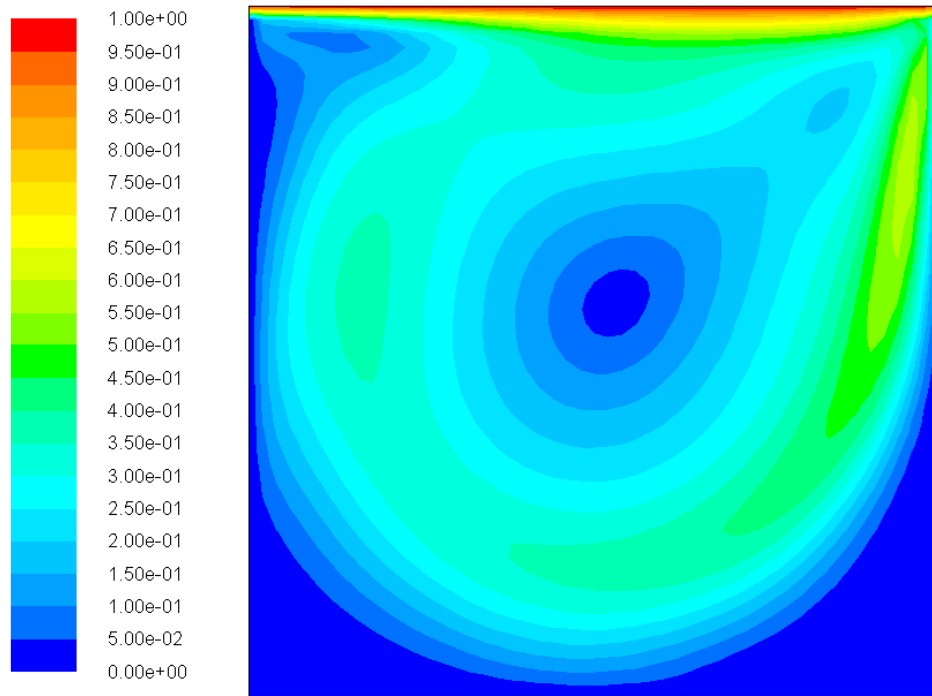
**Figure 21  $x$ -Velocity at the Vertical Center Line**



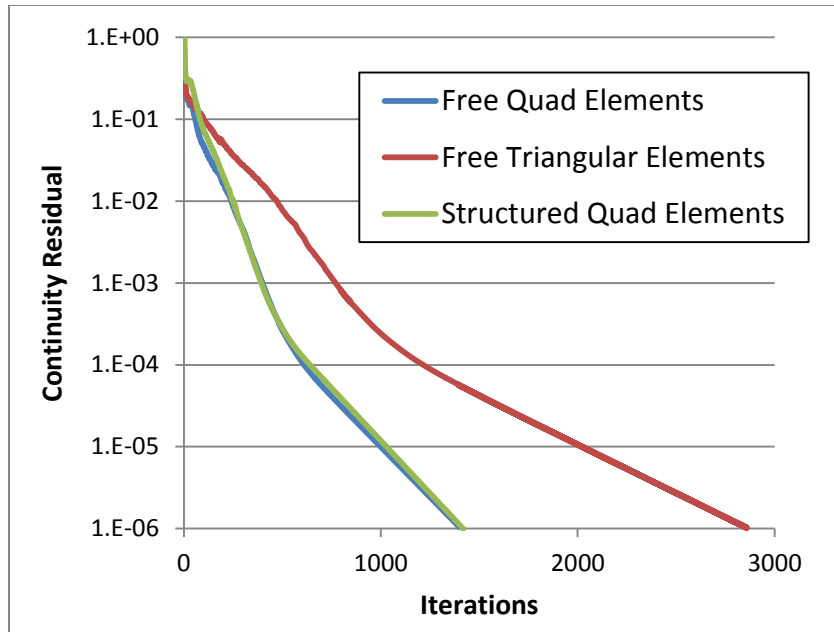
**Figure 22  $x$ -Velocity at the Vertical Center Line**



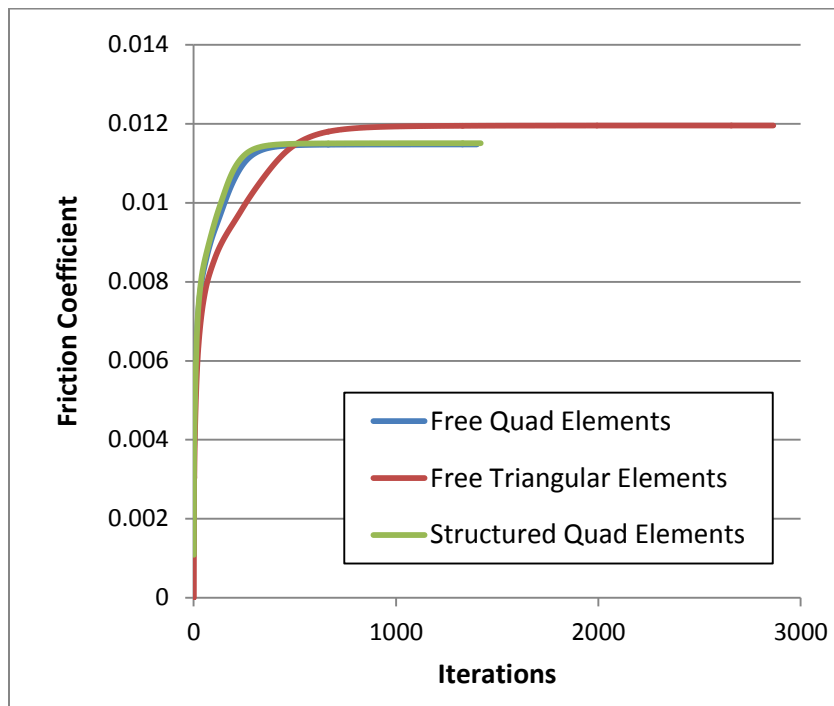
**Figure 23 Velocity Contour Plot (Free Quad Elements)**



**Figure 24 Velocity Contour Plot (Structured Quad Elements)**



**Figure 25 Continuity Residual History**



**Figure 26 Friction Coefficient History (At the Moving Wall)**

## 4.2 Helmholtz Resonator Case Study

Tones can be generated when gas flows over a cavity. A shear layer forms at the opening and oscillates periodically causing pressure fluctuations, which in turn generate sound. A real world example of this phenomenon is when a car is moving at a high speed with one window open. A tonal sound which is low in frequency can often be heard. A typical test case for this type of phenomenon is flow over the opening of a Helmholtz resonator. In that case, a tonal sound will develop, and the frequency of that tone can be analytically predicted.

### 4.2.1 Helmholtz Resonator

A Helmholtz resonator consists of two primary components: a cavity and a neck and is analogous to a spring-mass-damper system. Figure 27(a) shows a typical Helmholtz resonator and Figure 27(b) shows the spring-mass-damper system. The air at the neck acts like a mass ( $M$ ) while the elasticity of the air in the cavity is the spring ( $K$ ). The damping ( $C$ ) is due to the loss of energy through the neck due to viscous forces. Resonant frequencies are often excited by vortex shedding at the opening. It is assumed that sound generated has a frequency low enough that the wavelength of the sound is much larger than the cavity itself. As a result, the pressure can be seen as uniform inside the cavity. If the small portion of air in the neck in Figure 27(a) moves a small distance  $x$  into the cavity, it will compress the air in the cavity so that the volume of the cavity becomes  $V - S_b x$  and the pressure of the cavity becomes  $P_A + P$ . When compressed, the temperature of the system increases. However, this process can be assumed adiabatic because everything happens so

quickly and there is no time for the heat exchange. The adiabatic process has the following relation:

$$\frac{P}{P_A} = -\gamma \frac{\Delta V}{V} = -\gamma \frac{S_b x}{V} \quad \text{Equation 4-1}$$

where  $\gamma$  is the ratio of specific heats.

According to Newton's second law,

$$\frac{d^2 x}{dt^2} = \frac{F}{m} \quad \text{Equation 4-2}$$

where

$$F = PS_b = -\gamma \frac{S_b^2 P_A x}{V}$$

$$m = \rho S_b L$$

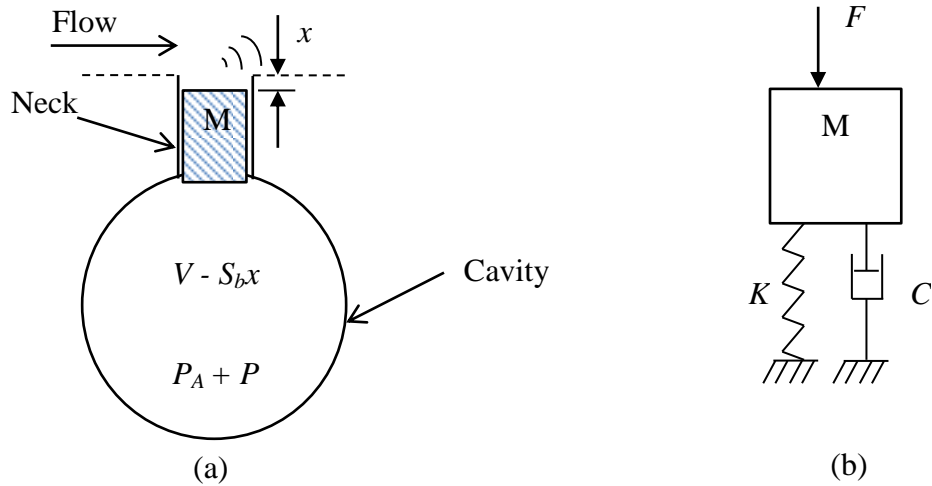
By replacing  $F$  and  $m$  using Equation 4-1, the following equation can be obtained:

$$\frac{d^2 x}{dt^2} = -\frac{\gamma S_b P_A}{\rho V L} x \quad \text{Equation 4-3}$$

This is a first order system and the natural frequency of this system is:

$$f = \frac{1}{2\pi} \sqrt{\frac{\gamma S_b P_A}{\rho V L}} = \frac{c}{2\pi} \sqrt{\frac{S_b}{V L}} \quad \text{Equation 4-4}$$





**Figure 27 Helmholtz Resonator and Spring-Mass Damper Analogy**

$L$  in the previous equation is now replaced with the corrected length  $L'$  because in reality, an additional volume outside the neck and inside the cavity moves with the system. The resonance frequency of the Helmholtz resonator can be expressed by the following formula:

$$f_c = \frac{c}{2\pi} \sqrt{\frac{S_b}{VL'}} \quad \text{Equation 4-5}$$

where

- $L'$  Corrected length of the neck
- $S_b$  Cross section area of the neck
- $V$  Volume of the cavity
- $c$  Speed of sound

The corrected length of the neck [51] can be approximated as:

$$L' = L + 0.96\sqrt{S_b} \quad \text{Equation 4-6}$$

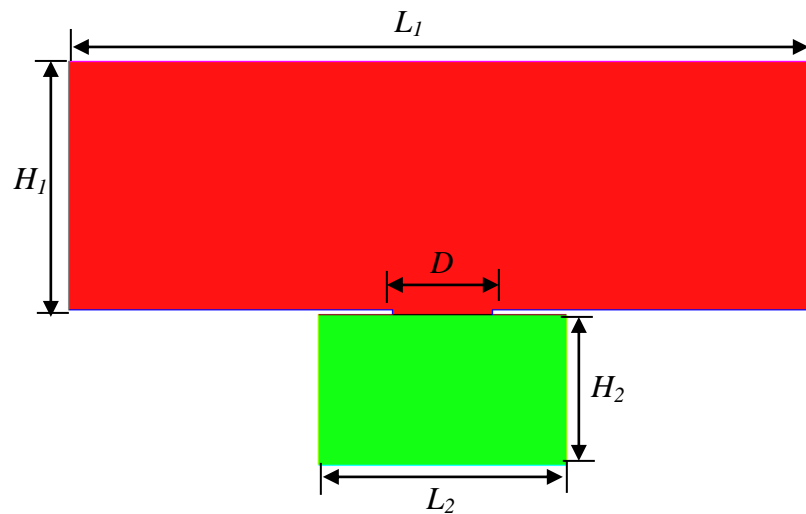
when the opening is flanged and

$$L' = L + 0.48\sqrt{S_b} \quad \text{Equation 4-7}$$

when the opening is in free space.  $L$  is the length (height) of the neck.

#### 4.2.2 Geometry and Mesh

Figure 28 shows the geometry of the simulated Helmholtz resonator. The length of each section can be found in Table 2. The geometry has three components: the free stream area (shown in red), the resonator cavity (shown in green), and the neck connecting the free stream area and the resonator cavity.

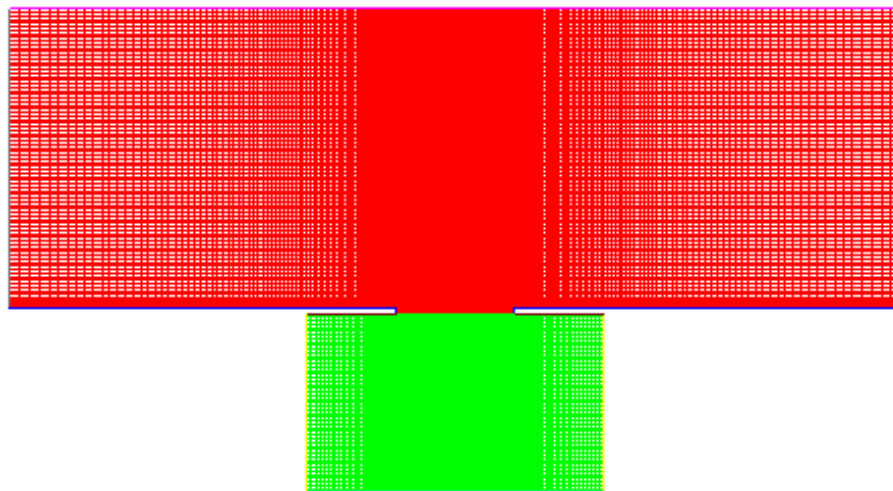


**Figure 28 Geometry of the Simulated Helmholtz Resonator**

**Table 2 Dimension of the Simulated Helmholtz Resonator**

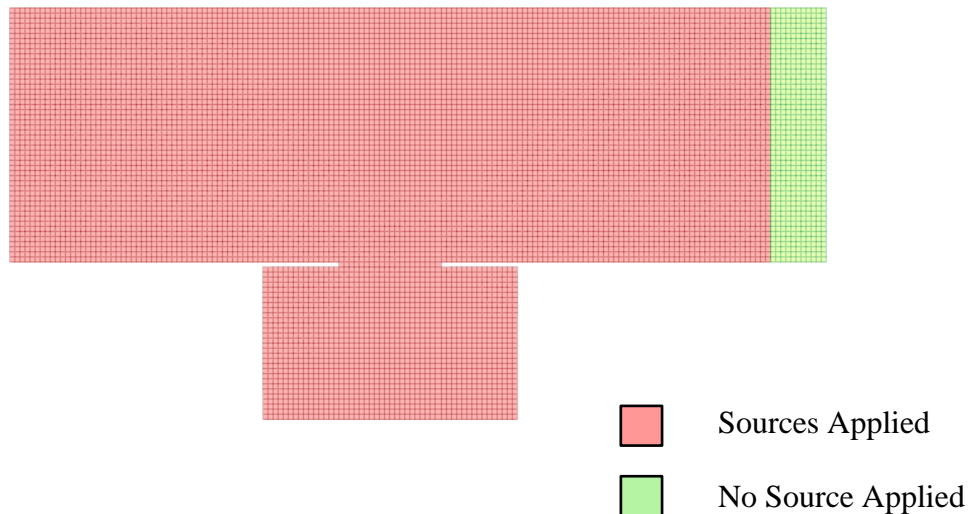
$L_1$	1.5 m
$H_1$	0.5 m
$D$	0.2 m
$L_2$	0.5 m
$H_2$	0.3 m
Neck Length	0.01 m

These values were recommended by ANSYS FLUENT [52] in order to achieve a relatively low resonance frequency, and therefore requires less solution time because the sampling frequency can be lower (See Chapter 3.4.1). The frequency of the resonator can be calculated using Equation 4-5, and a frequency of 120 Hz is obtained.



**Figure 29 Helmholtz Resonator Mesh for CFD Simulation**

Figure 29 shows the mesh used for the CFD simulation. All the parts of the geometry are simple and a structured mesh was used because of the simple geometry. The minimum element length is 2 mm while the maximum element length is 17.2 mm at the inlet and outlet. Another coarser mesh (Figure 30) for acoustic simulation has been made to shorten the run time needed for the acoustic calculation. A conservative integration method is chosen to preserve the source information in the projection from the CFD domain to the acoustic domain (see Chapter 3.3.1 for detail of source projection). The mesh is extended at the outlet for acoustic wave propagation purposes. The element size is uniformly 10 mm in this mesh.

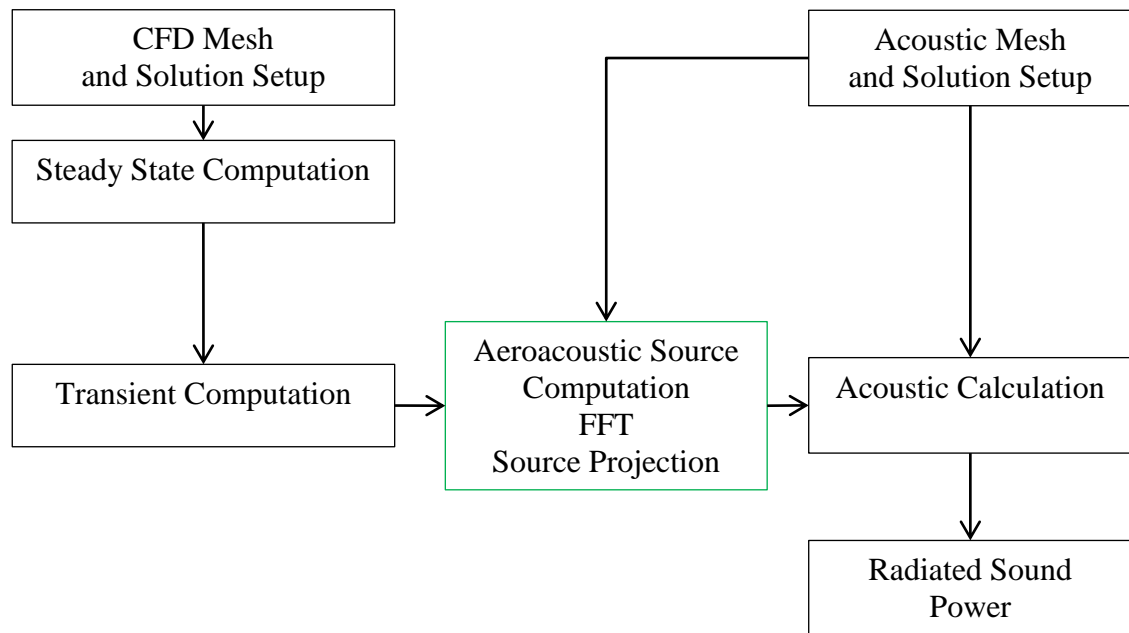


**Figure 30 Helmholtz Resonator Mesh for Acoustic Simulation**

#### **4.2.3 Simulation Setup and Steps**

Figure 31 shows the overview of the simulation steps. The first step is to generate the CFD mesh and setup the CFD simulation with proper boundary conditions, and a

turbulent model. A steady state CFD computation is then performed to determine the initial flow velocity. The steady state velocity field is then used to initialize the transient computation. During the transient computation, the velocity and density fields are exported at each time step. The next step is to link between the CFD simulation and acoustic simulation by computing aeroacoustic sources from the transient CFD simulation. A fast fourier transform is performed so that the source terms are transferred into the frequency domain. In order to use the coarser mesh (compared to the CFD mesh) for the acoustic simulation, the source terms are projected to the acoustic mesh and the acoustic simulation is performed in the frequency domain. Each of these steps will now be discussed in more detail.



**Figure 31 Simulation Process**

#### 4.2.3.1 Steady State Solution

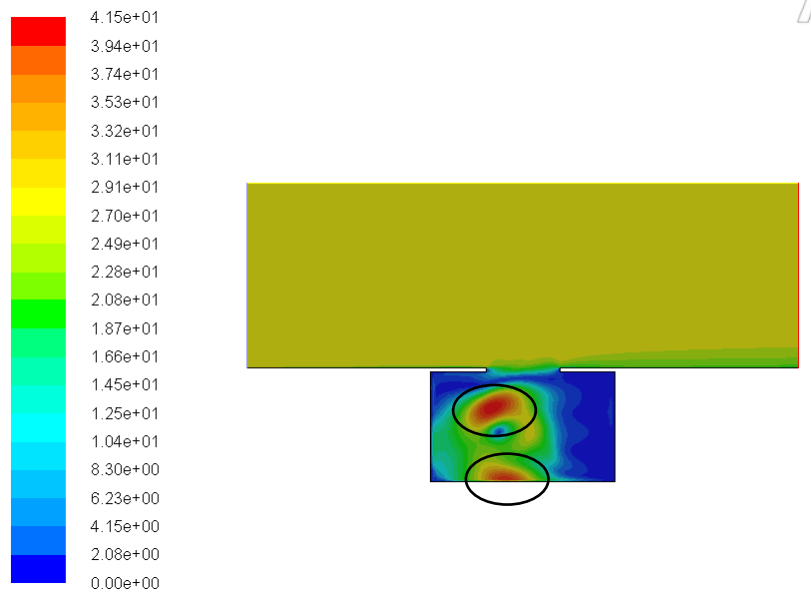
A steady state solution is first conducted in preparation for the transient simulation. In general, the transient solution data needs to be collected until the flow is fully established. In order to meet this requirement, analysts must run the transient flow simulation for a very long time before exporting the solution data from each of the time steps. Alternatively, a steady state solution can be performed and the steady state solution data is used to initialize the transient solution from which the transient solution data is exported. Information about the simulation setup including the turbulence model and the boundary conditions can be found in Table 3.

A realizable  $k - \varepsilon$  with non-equilibrium wall function is selected as the turbulence model in this simulation. The realizable  $k - \varepsilon$  model is suitable for coarse meshes, where the wall-cell  $y^+$  values are typically 30 and above. The term “realizable” means that the model satisfies certain mathematical constraints so that the Reynolds stresses calculated are consistent with the real flow physics. Like the standard wall functions, the non-equilibrium wall functions are also a two-equation approach. Unlike the standard wall functions, the non-equilibrium wall functions are sensitized to pressure-gradient effects [53]. SIMPLE (semi-implicit method for pressure-linked equations) pressure-velocity coupling method is selected. The SIMPLE algorithm uses a relationship between velocity and pressure corrections to enforce mass conservation and to obtain the pressure field [54]. The Green-Gauss cell based method is selected for its good performance with structured meshes as recommended by ANSYS FLUENT [52]. The computation is initialized from the inlet which means the conditions at the inlet are first satisfied.

**Table 3 Steady State Simulation Setup**

Turbulence Model	Realizable k- $\epsilon$ with non-equilibrium wall functions
Fluid Property	Ideal-gas
Pressure-Velocity Coupling	SIMPLE
Gradient Method	Green-Gauss cell based
Inlet	Velocity inlet $V = 27$ m/s with 1% turbulence intensity
Outlet	Pressure outlet $P = 1$ atm with 1% turbulence intensity
Initialization	Initialized from inlet

After 300 iteration, the solution converged. It can be seen in the velocity contour plot below that two unsteady regions with high velocity magnitude have formed (see Figure 32 circled parts). The velocity field at this point is used to initialize the transient solution.



**Figure 32 Velocity Contour Plot (Steady State)**

#### 4.2.3.2 Transient Solution

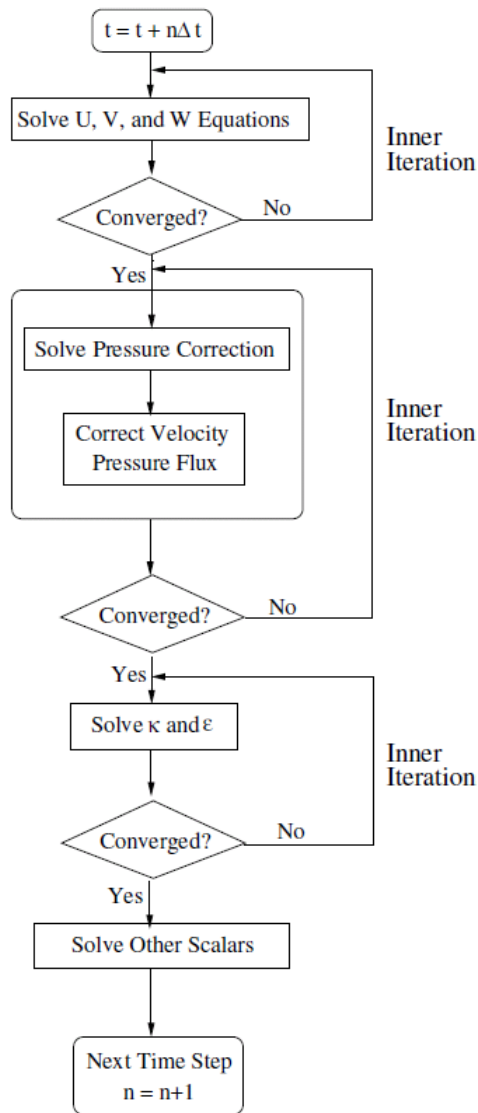
A built-in ANSYS FLUENT TUI command *init-instantaneous-vel* provides a way to get a more realistic instantaneous velocity field (this new velocity field is unsteady). Transient LES simulation can be started after the issuance of this command. The setup of LES simulation is listed in Table 4. More information about the LES simulation can be found in Section 2.4.3. It is well known that LES requires excessively high resolution for wall boundary layers because near the wall, the turbulence components are geometrically very small close to the wall. As a result, standard LES is only recommended to the flow situation where the wall boundary layers are irrelevant. However, with the help of WALE (Wall-Adapting Local Eddy-Viscosity) model, the hardship of LES can be improved at the boundary layers. It will also make it possible to compute laminar shear boundary layers without any model impact because it returns a zero turbulent viscosity for laminar shear flows [55].

**Table 4 Transient LES Simulation Setup**

Turbulence Model	LES with WALE subgrid-scale model
Fluid Property	Ideal-gas
Transient Formulation	Non-iterative time advancement
Gradient Method	Green-Gauss cell based
Inlet	Velocity inlet $V = 27$ m/s with 1% turbulence intensity
Outlet	Pressure outlet $P = 1$ atm with 1% turbulence intensity
Initialization	Initialized from steady state solution.
Time Step	$3 \times 10^{-4}$ s, 1500 steps



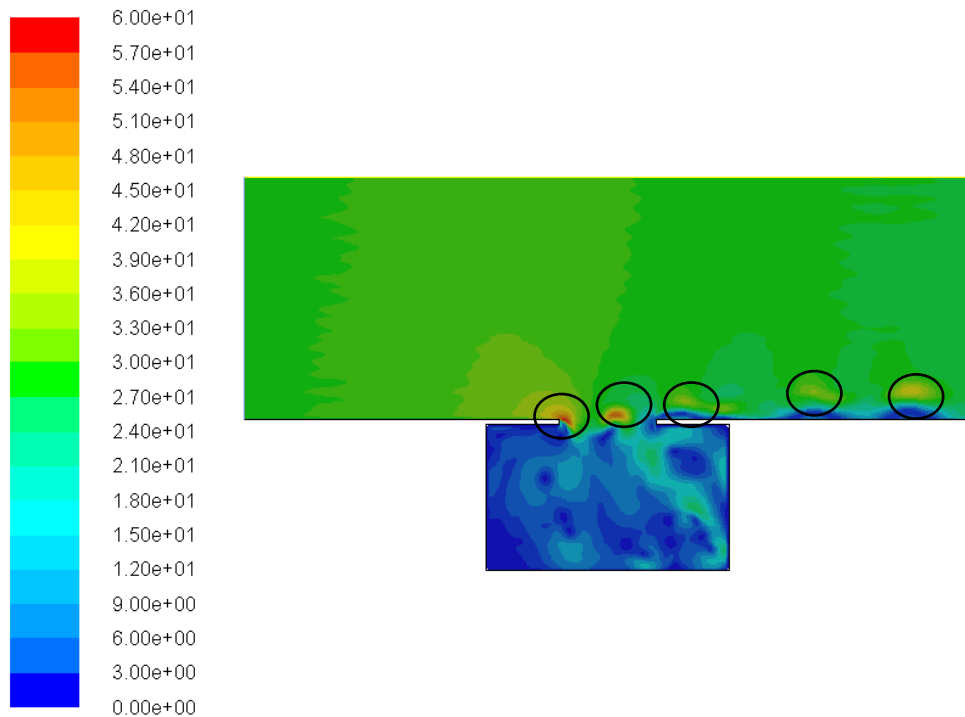
The non-iterative time advancement algorithm is selected to compensate for the slow solution of the LES model. In this algorithm, the splitting error is kept at the same order as the truncation error whereas in the iterative algorithm, the splitting error is zero. The overview of the non-iterative time advancement salutation method is shown in Figure 33.



**Figure 33 Non-Iterative Time-Advancement Scheme [6]**

The time step selected is  $3 \times 10^{-4}$  s with a total number of 1500 steps. With the selected time step configuration, the frequency domain result for identifying and simulating vortex shedding is valid up to 250 Hz (see Chapter 3.4).

A velocity contour plot randomly selected during the transient calculation is shown in Figure 31. From the velocity contour plot, vortex shedding can be clearly seen (see black circles in Figure 34). By monitoring the velocity contour plot in successive time steps, the vortex shedding frequency can be estimated to be approximately 130 Hz. Although it is only an estimation, this method can be used to quickly get an idea whether the simulation is correct before proceeding to the acoustic simulation.

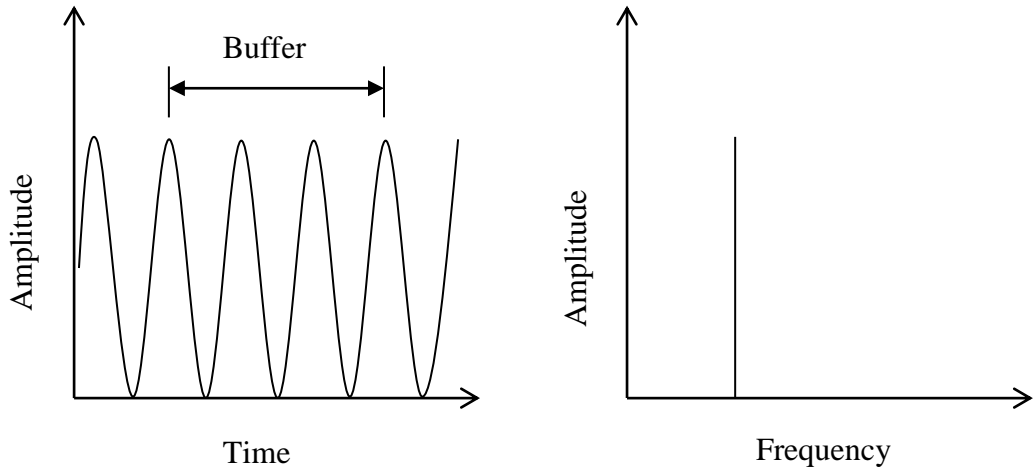


**Figure 34 Velocity Contour Plot (Transient)**

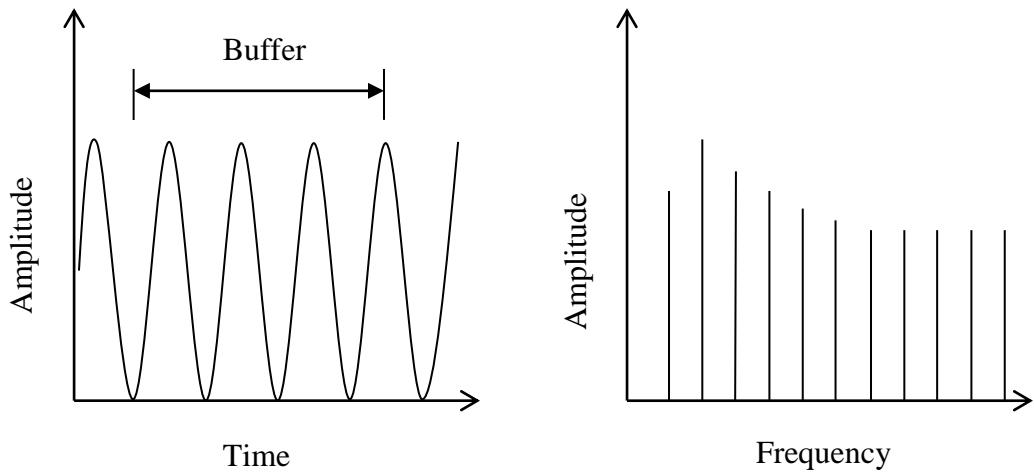
#### **4.2.3.3 Acoustic Solution**

Velocity and density fields at each of the 1500 time steps were imported into the FFT ACTRAN ICFD solver which is the interface between CFD codes and ACTRAN acoustic module. Two major functions of the ICFD solver are 1) computing the aeroacoustic source, and 2) performing Fourier transform. With the help of this solver, A fast Fourier transform is performed and the Lighthill tensor is calculated. The time domain data is transferred to the frequency domain and the sources are mapped from the CFD domain to the acoustic domain. During the FFT process, a proper window function should be used in order to minimize the edge effects that result in spectral leakage. It is desired that the acquisition buffer used in the FFT process is over an integer number of periods which will result in an ideal frequency domain data (see Figure 35).

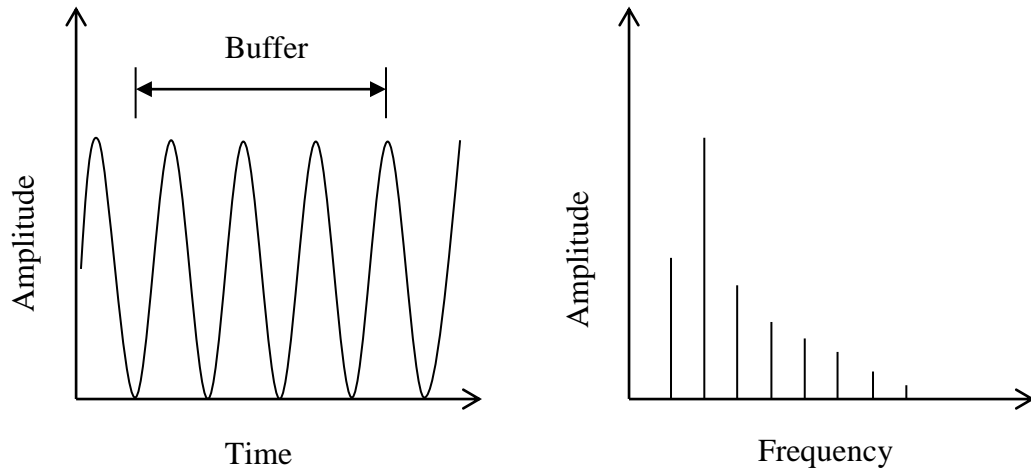
Unfortunately, that is unlikely to happen. When the acquisition buffer contains a non-integer number of periods, the spectral leakage will result in a distorted result (see Figure 36). With the help of Window functions, the spectral leakage can be improved with some trade-offs such as reduced frequency resolution and decreased amplitude (see Figure 37). The Hann window function is used in the FFT process because it is known to have a good compromise between the frequency resolution and the spectral leakage.



**Figure 35 FFT with Integer Number of Periods**



**Figure 36 FFT with Non-Integer Number of Periods**



**Figure 37 FFT with Non-Integer Number of Periods (Windowed)**

A contour plot of the divergence of the Lighthill surface at 131 Hz is shown in Figure 38. In this Figure, the divergence of convective fluxes is presented. The divergence of convective fluxes is defined by

$$\text{div}(\text{Fluxes}_{conv}) = \int_{\Omega} \frac{i}{\rho_0 \omega} \frac{\partial \delta \psi}{\partial x_i} \frac{\partial}{\partial x_j} F(\rho v_i v_j) d\Omega \quad \text{Equation 4-8}$$

which is the right hand side of Equation 2-16. Notice that not all of the components of the right hand side of Equation 2-16 are calculate because the cell Reynolds number is greater than one and the convective fluxes dominates as a consequence. This is the case even at the boundary layers. The entropy term of Equation 2-16 is zero for homentropic flows (no combustion involved). Regions in Figure 32 with larger values contain stronger sources. A direct frequency analysis is performed after the ICFD run. Figure 39 shows a schematic of the analysis.

The radiated sound power is evaluated at the infinite element layer using the total acoustic pressure and velocity field using the following equation:

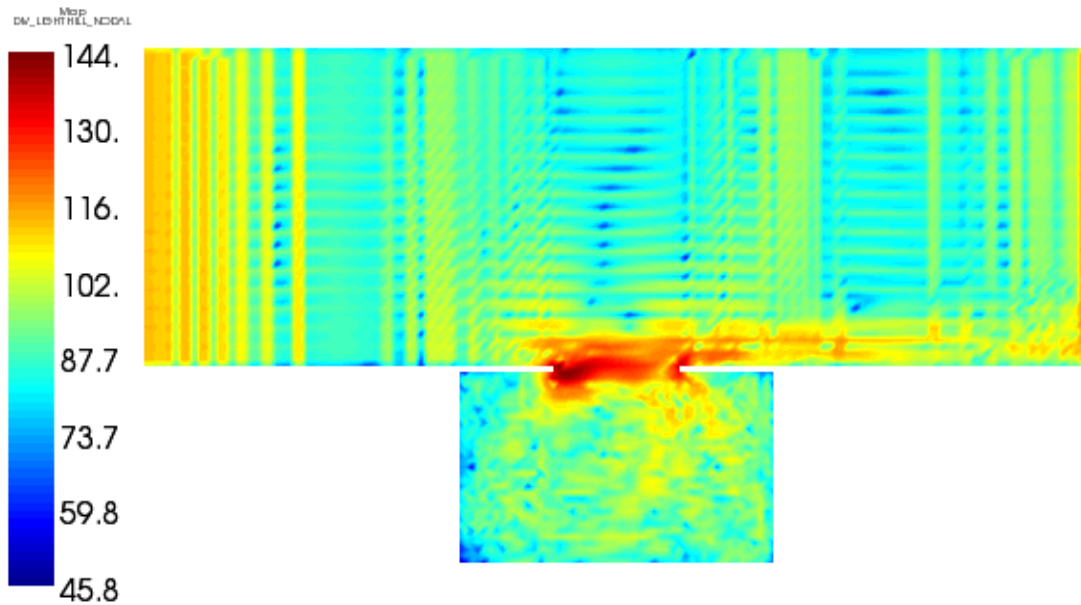
$$W_{rad} = \frac{1}{2} \int p_{tot} v_{tot}^* dS \quad \text{Equation 4-9}$$

where  $p_{tot}$  and  $v_{tot}$  are defined by the equations

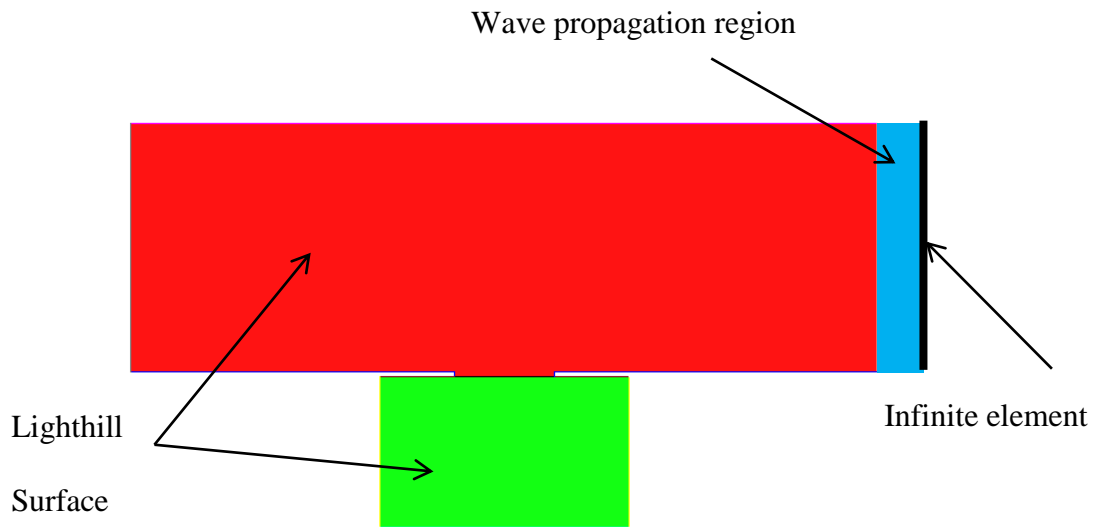
$$p_{tot}^2 = \frac{1}{S} \int p_{tot} p_{tot}^* dS \quad \text{Equation 4-10}$$

$$v_{tot}^2 = \frac{1}{S} \int v_{tot} v_{inc}^* dS \quad \text{Equation 4-11}$$

$v_{inc}$  is called the incident (in free field conditions) velocity field and it is generated by the various sources.

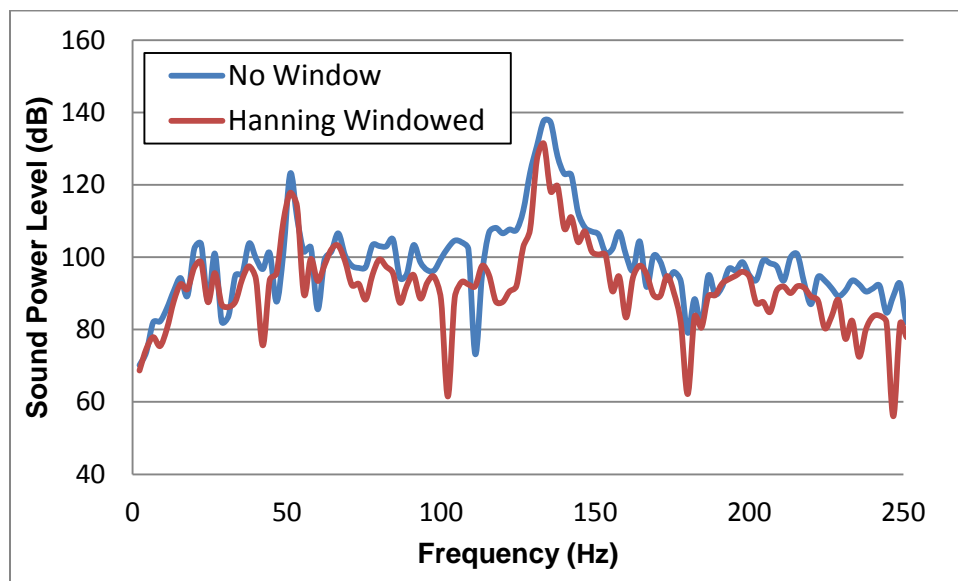


**Figure 38 Divergence of Lighthill Surface at 131 Hz**



**Figure 39 Direct Frequency Analysis Setup**

**4.2.4 Result and Discussion**



**Figure 40 Radiated Sound Power at Outlet**

Figure 40 shows the radiated sound power at the outlet of the Helmholtz resonator. The most important tone is at 133 Hz which is approximately 10 Hz higher than the analytical solution. This result is reasonable since the formula used to estimate the resonance frequency is also an approximation. Furthermore, the analytical solution does not consider the effect of sound and flow interactions.

More importantly, a 3 dB difference can be seen between the result with windowing and the result without. Therefore, the windowed data should be scaled up by 3 dB.

It has been verified that a steady state velocity field can be used to initialize the transient solution with the help of the built-in ANSYS FLUENT TUI command and as a result, the time needed for the transient solution is greatly reduced because a fully developed flow can be obtained from the specially initialized steady state velocity field (which takes less time to calculate). The combination of LES turbulence model and Lighthill's analogy has worked well in this case as the main peak of the simulated result is within 8% of the analytical solution. Also, the Hann window function reduced some spectral leakage.

### **4.3 Flow Over Cylinder Case Study**

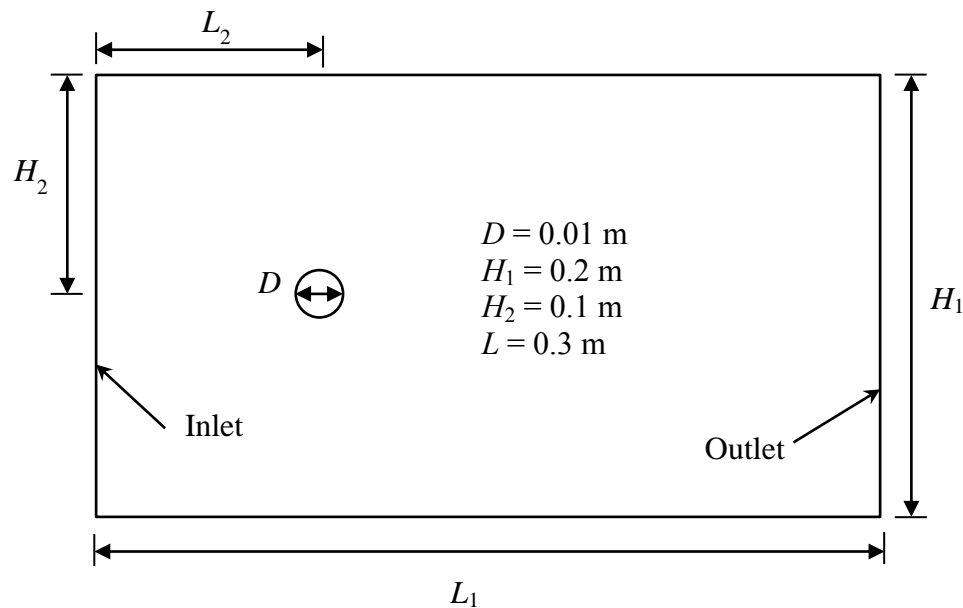
The purpose of the flow over cylinder case is to examine the effects of the height of the wall on the aeroacoustic result and the performance of the SST  $k - \omega$  turbulence model in an aeroacoustic simulation. Compressible flow and incompressible flow have been used on both of the cases. Two identical models have been made with different  $y^+$



values (see Chapter 3.5 for details on  $y^+$  value). The results from both models are compared.

#### 4.3.1 Geometry and Mesh

Figure 41 shows the dimensions of the geometry. By design, the air enters the duct from the left side with a flow velocity of 20 m/s. Using the equation discussed in Chapter 3, the vortex shedding frequency with this geometry is at 400 Hz. In order to minimize the effects of the walls on the flow, the both the distance from the top wall and bottom wall to the center of the cylinder is 10 times the cylinder diameter. The distance from the inlet to the center of the cylinder is 10 times the cylinder diameter as well. The distance from the outlet to the center of the cylinder is 20 times the cylinder diameter so that the flow can be established before it exits the outlet. A fully structured mesh was used in all analyses.



**Figure 41 Flow Over Cylinder Case Geometry**

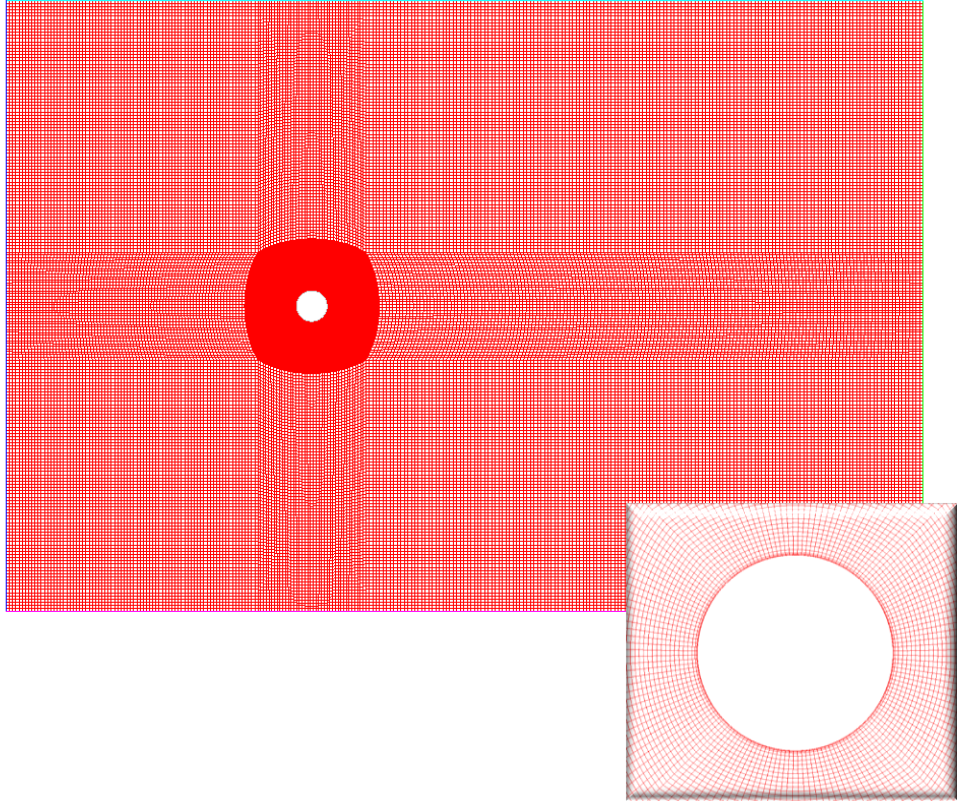
The wall height for each case is listed in the table below. A  $y^+$  value of 1 means that the node closest to the wall falls in the viscous sub layer while a value of 30 implies that it falls in the log law region of the boundary layer. Table 5 lists the  $y^+$  values (dimensionless) and the corresponding real wall height.

**Table 5  $y^+$  and Corresponding Wall Height**

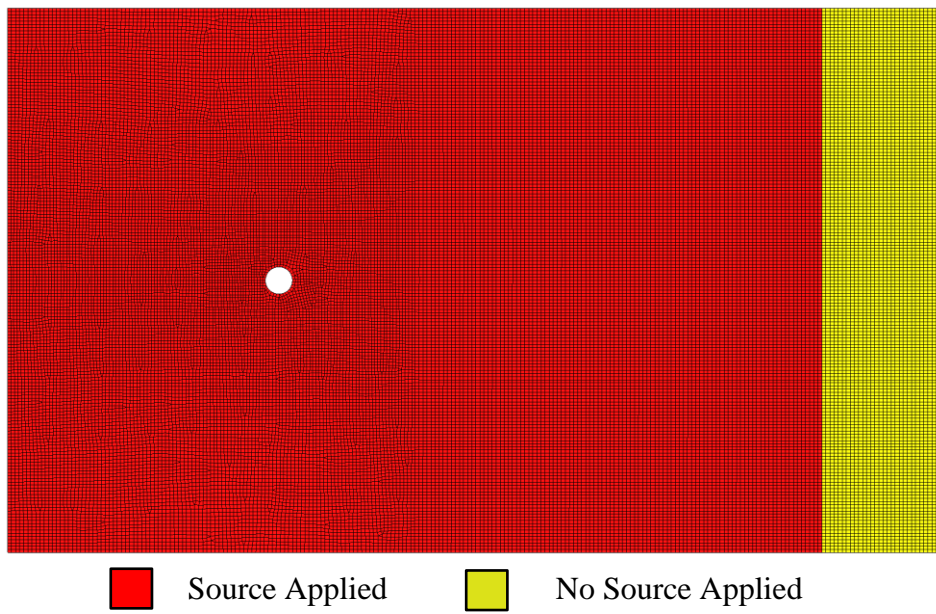
$y^+$	Wall Height
1	$1.15 \times 10^{-5}$ m
30	$3.3 \times 10^{-4}$ m

The upper part of Figure 42 shows the structured mesh while the lower part is a zoomed in look of the mesh close to the cylinder.

A 2-D acoustic mesh (Figure 43) has been made with coarser element size of 1 mm. Notice that the acoustic mesh is extended at the outlet (yellow part in Figure 43) for the purpose of sound wave propagation (it is not necessary but a convention). The Lighthill tensors are calculated from at the CFD domain and then mapped to the acoustic source domain (red part in Figure 43).



**Figure 42 Mesh for the Flow Over Cylinder Case**



**Figure 43 Acoustic Mesh for the Flow Over Cylinder Case**

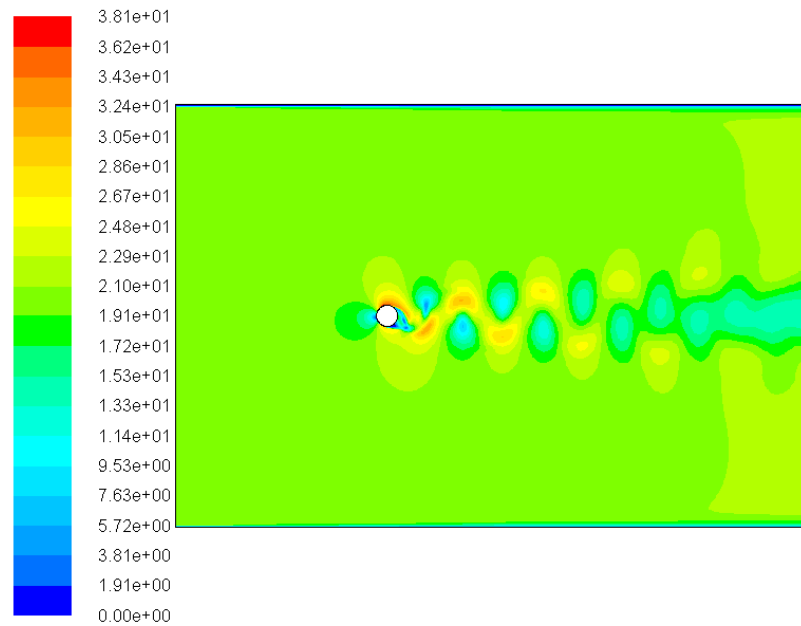
### 4.3.2 Transient CFD solution

The transient CFD simulation setup is shown in Table 6. The reason of choosing the SST  $k - \omega$  turbulence model is to better simulate the adverse pressure gradient when air strikes the cylinder. In the SST  $k - \omega$  turbulence model, standard wall functions were used for the coarser wall boundary mesh ( $30 < y^+ < 300$ ). For the fine wall mesh ( $y^+ < 4$  to 5), the appropriate low-Reynolds number boundary conditions were applied. The SIMPLE pressure-velocity coupling method is used though it was admittedly not the only choice. However, the purpose of this simulation was not to verify or benchmark pressure-velocity coupling methods. Simulations were performed for both incompressible and compressible flow. A case can be made for incompressible flow since the Mach number is under 0.1. A step time of  $3.7 \times 10^{-5}$  s was used with 3000 time steps. This will result in a frequency resolution of 9 Hz and the results are valid up to 1000 Hz (see Chapter 3.4 for details). The CFD analysis was performed for 2000 time steps to fully establish the flow prior to running for the 3000 time steps. It took about 5 hours to complete each of the CFD runs.

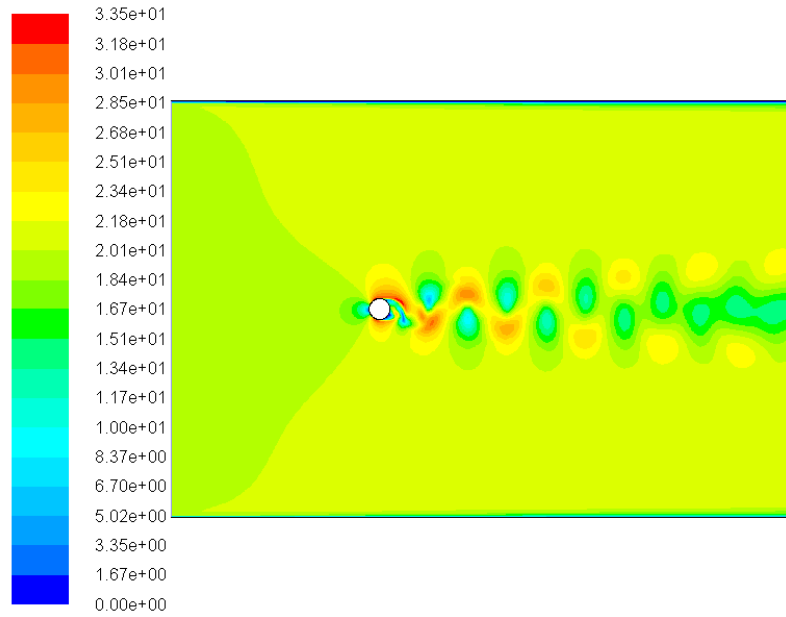
Figures 44 and 45 show contour plots of the flow velocity magnitude for compressible and incompressible flow respectively with  $y^+$  value of 1. Similarly, Figures 46 and 47 show the velocity magnitudes for cases with  $y^+$  equal to 30. Figures 46 and 47 show the contour plots for compressible and incompressible flow respectively.

**Table 6 Transient SST  $k - \omega$  Simulation Setup**

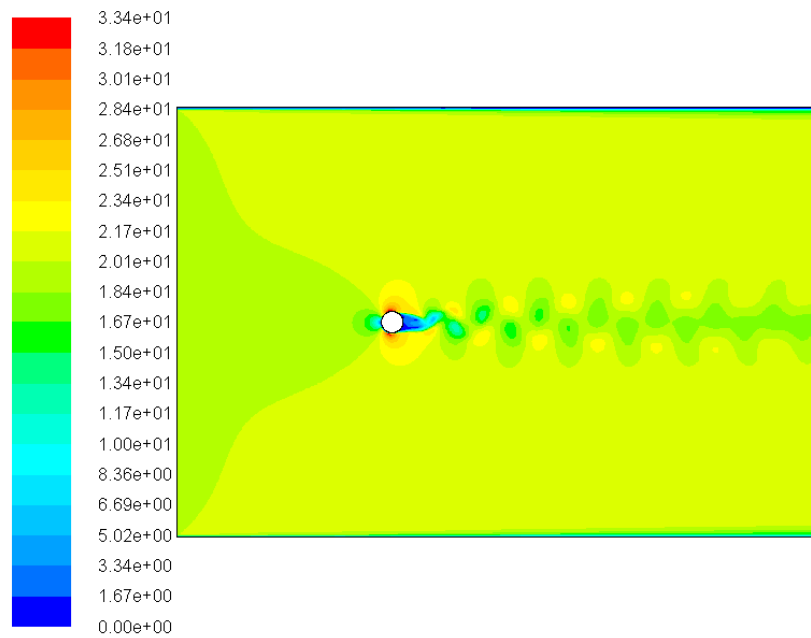
Turbulence Model	SST $k - \omega$
Fluid Property	Incompressible and compressible for both $y^+$ values
Pressure-Velocity Coupling	SIMPLE
Gradient Method	Green-Gauss cell based
Inlet	Velocity inlet $V = 20$ m/s with 5.06% turbulence intensity
Outlet	Pressure outlet $P = 1$ atm with 5.06% turbulence intensity
Initialization	Initialized from inlet
Time Step	$3.7 \times 10^{-5}$ s, 3000 time steps



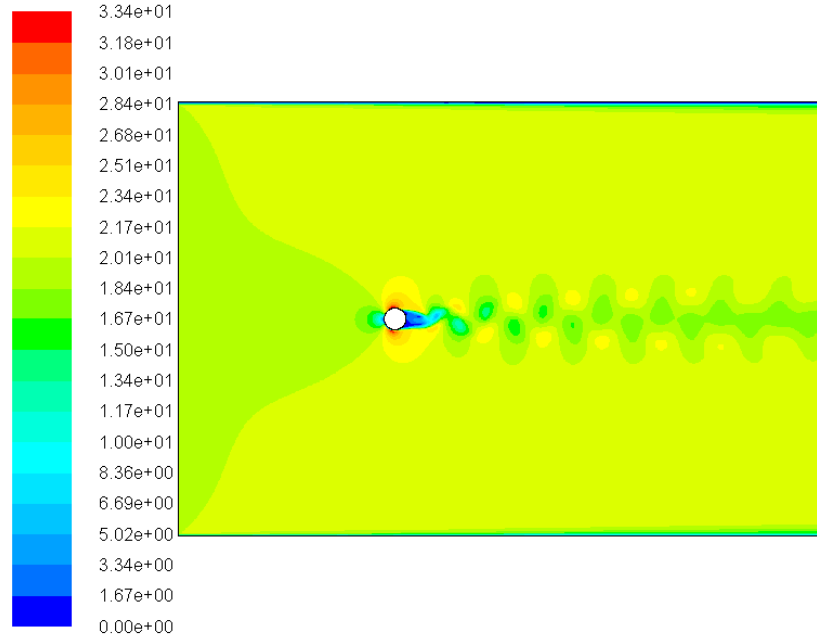
**Figure 44 Velocity Contour of Compressible Flow,  $y^+ = 1$  Case**



**Figure 45 Velocity Contour of Incompressible Flow,  $y^+ = 1$  Case**



**Figure 46 Velocity Contour of Compressible Flow,  $y^+ = 30$  Case**

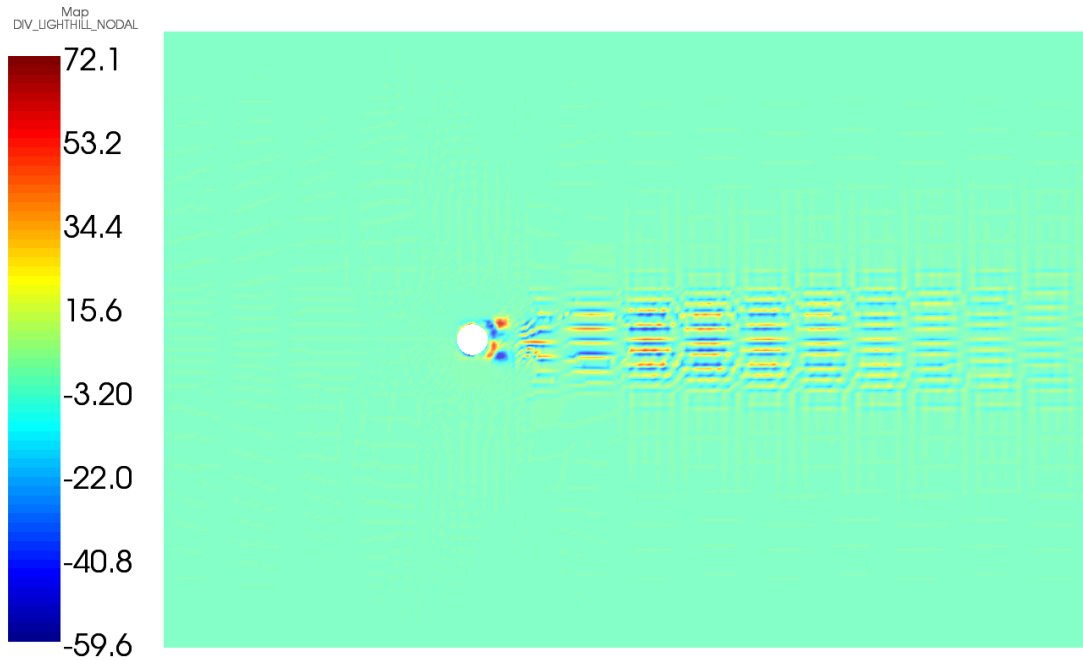


**Figure 47 Velocity Contour of Incompressible Flow,  $y^+ = 30$  Case**

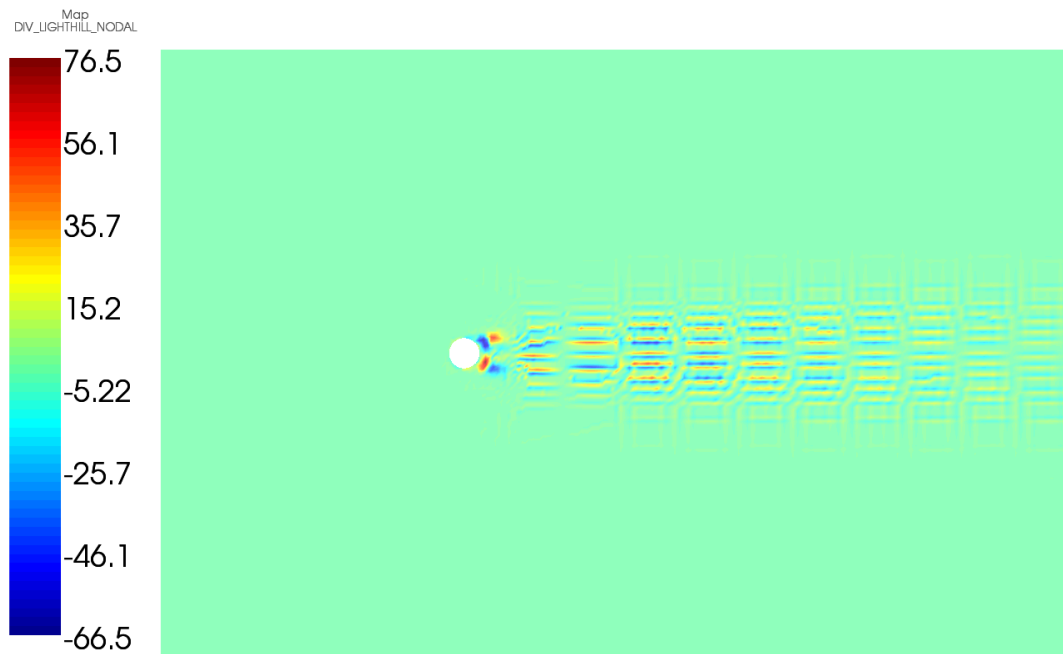
### **4.3.3 Acoustic Simulation**

Velocity and density fields at each of the 3000 time steps were imported to the FFT ACTRAN ICFD solver. With the help of this solver, the Lighthill tensor is calculated and a fast Fourier transform is performed to transfer the time domain data to the frequency domain.

Contour plots showing the divergence are shown in Figures 48 and 49 for compressible and incompressible flow respectively. Regions with large absolute values indicate stronger sources.



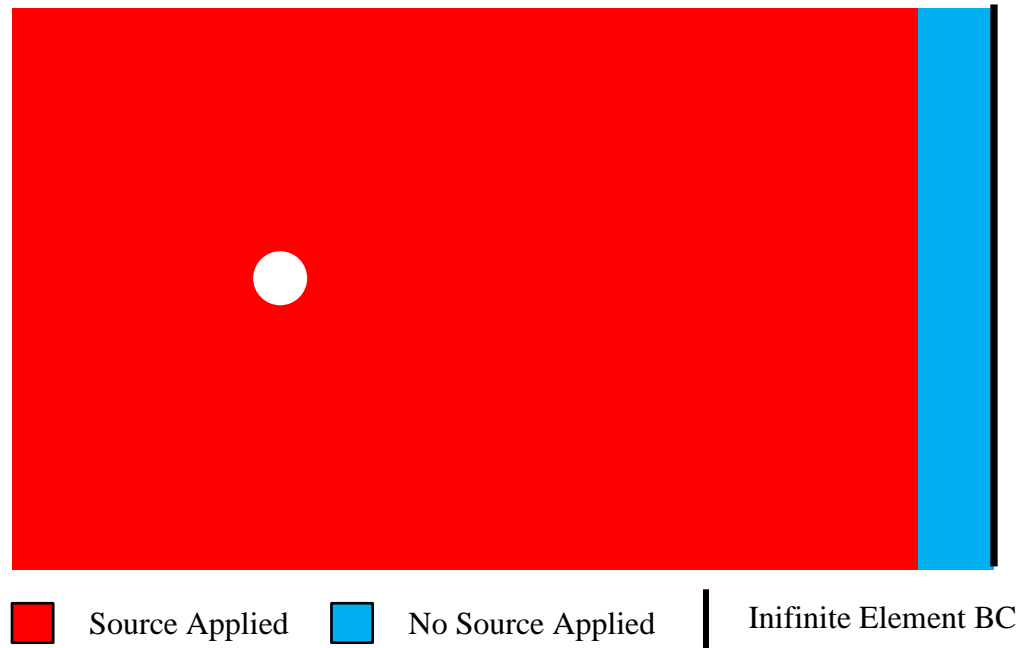
**Figure 48 Divergence of Lighthill Surface at 477 Hz (Compressible,  $y^+ = 1$ )**



**Figure 49 Divergence of Lighthill Surface at 477 Hz (Incompressible,  $y^+ = 1$ )**

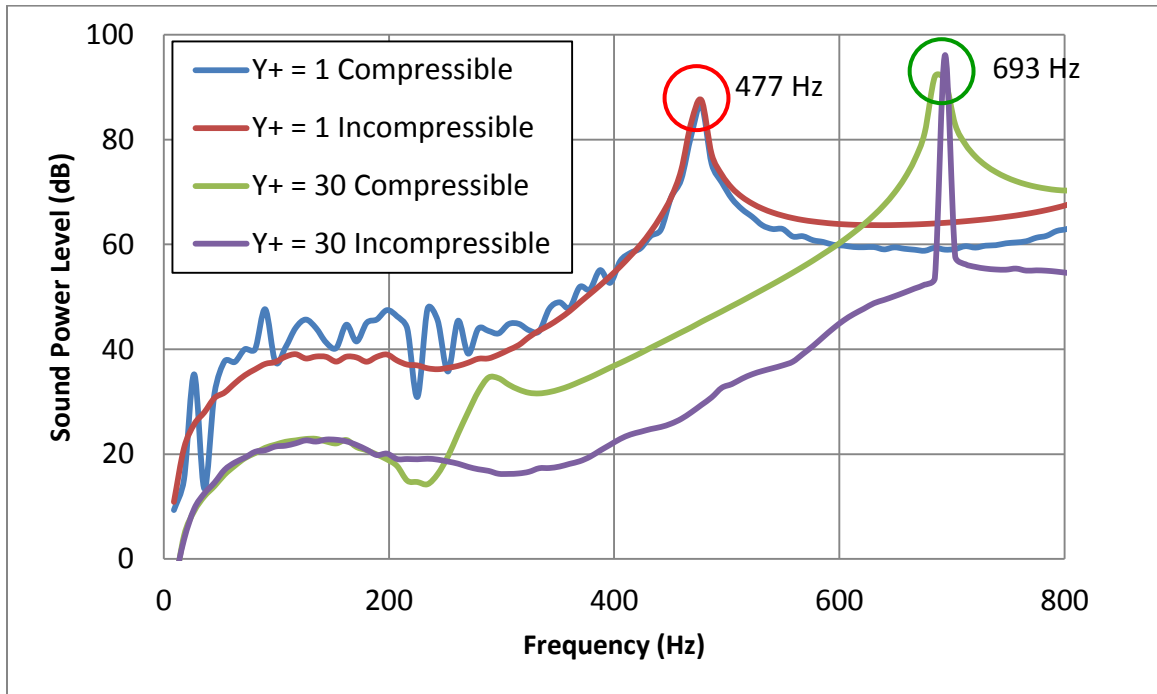


The setup for the direct frequency analysis is shown in Figure 50. The mesh for the direct frequency analysis is coarser than the mesh used in the CFD simulation because the geometric scale of the acoustic analysis is much larger. The conservative integration method is selected to map the aeroacoustic sources from the CFD domain to the acoustic domain so that all of the sources can be accounted for.



**Figure 50 Direct Frequency Analysis Setup**

#### 4.3.4 Result and Discussion



**Figure 51 Radiated Sound Power at Outlet**

Figure 51 shows the radiated sound power at the outlet for the four cases studied. The main peaks of the cases with a  $y^+$  value of 1 is at 477 Hz while the main peaks of the cases with a  $y^+$  value of 30 is at 693 Hz. The analytical solution is at 400 Hz (see Chapter 2.2). By inspecting the main peaks, it is obvious that the result from the cases with  $y^+ = 1$  is closer to the target. From the results, it appears that the incompressible flow will suffice if the flow velocity is very low compared to the speed of sound.

For cases with  $y^+$  value of 30, the results are not very satisfactory. In the flow over cylinder case, the strong adverse pressure gradient plays an important role. In order to model the flow separation in this case, the near wall region needs to be modeled with a good resolution so that the flow separation in the near wall region is modeled accurately.

It is recommended that a fine mesh be used when there are strong adverse pressure gradients. In the flow over cylinder case study, it has been verified that the SST  $k - \omega$  turbulence model and the Lighthill analogy appear to work reasonably to solve aeroacoustic problems with proper simulation setup and good quality mesh.

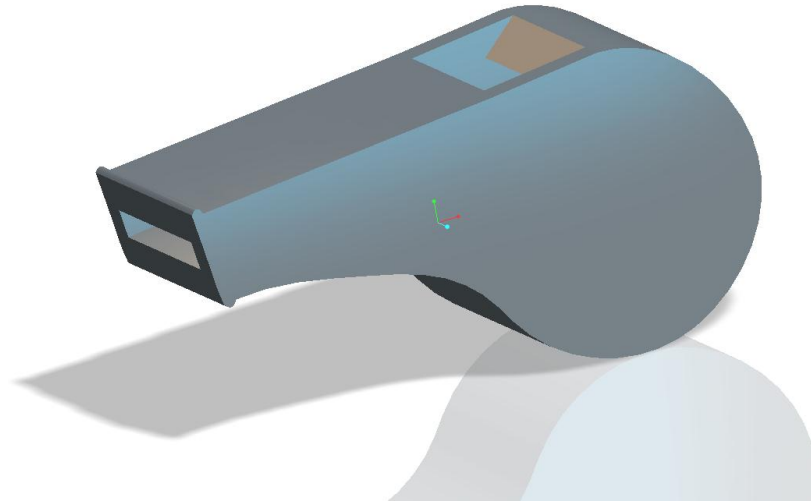
## Chapter 5

### Whistle Case Study – Measurement and Simulation

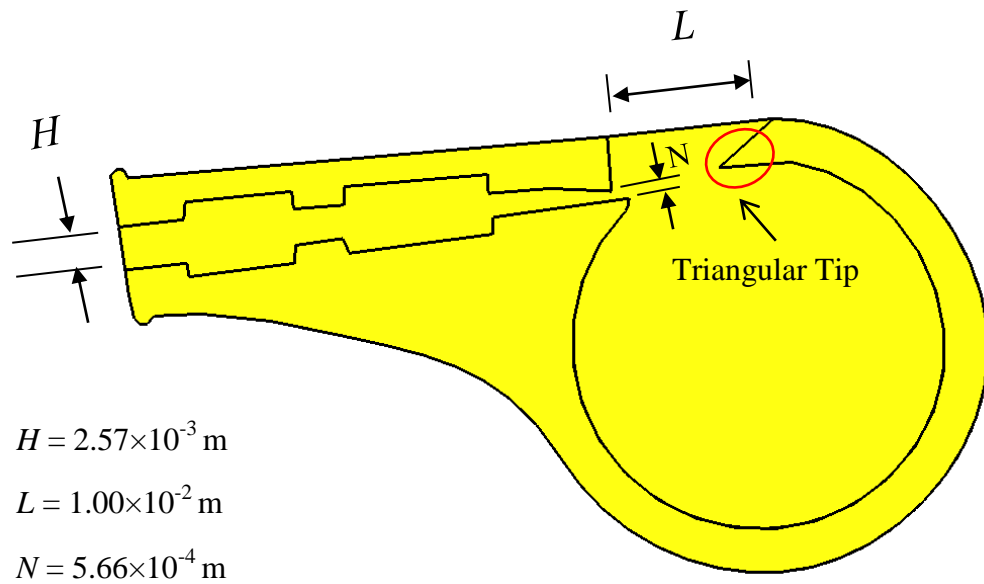
In this chapter, a pea-less whistle is studied with both experiment and simulation. In the simulation, different combinations of compressibility and two turbulence models are examined. The first run uses the  $k - \varepsilon$  model and compressible air and the second one uses the same turbulence model but incompressible air. The third run uses the  $k - \omega$  turbulence model with compressible air and the last takes the same turbulence model but with incompressible air. Scaling is needed so that the sound pressure from a 2-D simulation can be compared to the experiment. The scaling of the results from 2-D to 3-D is considered and recommendations are made at the end of this chapter.

#### 5.1 Whistle Geometry

The whistle used in this chapter is a common pea-less whistle which can be found at many stores. The material of this whistle is engineering PVC. If blown hard, the whistle can generate a sound pressure level of as high as 115 dB close to the outlet. Figure 52 shows the solid model of the whistle and Figure 53 the cross section. Some dimensions are presented in Figure 53. The shortest distance between the two walls at the neck of the whistle is  $5.66 \times 10^{-4}$  m. This small opening at the end of the inlet duct acts like a nozzle which accelerates the flow before the flow strikes the triangular tip (see Figure 53).



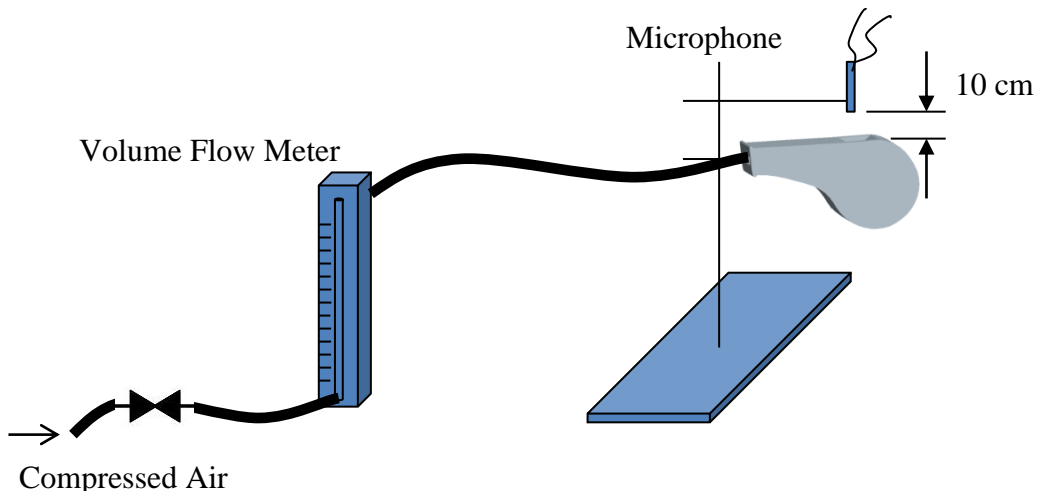
**Figure 52 Solid Model of the Whistle**



**Figure 53 Cross Section of the Whistle**

## 5.2 Sound Pressure Measurement

Figure 54 shows the experimental setup. Compressed air is used to drive the whistle. The flow is controlled by a valve and then flows through a flow meter. A microphone used to measure the sound pressure level is located 10 cm above the whistle outlet. The air flow rate is adjusted so that the air flow velocity at the inlet of the whistle is 8 m/s. The experiment was conducted inside of the hemi-anechoic chamber at the University of Kentucky. The chamber is qualified down to a 150 Hz. Figure 55 shows some photographs of the experimental setup including the whistle and attached air hose, and the flow meter.

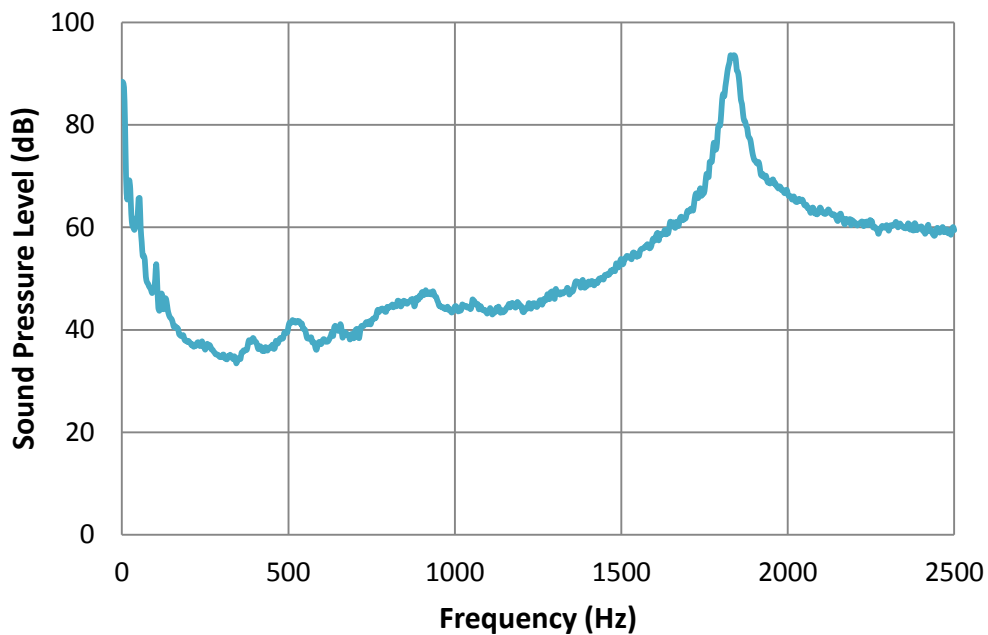


**Figure 54 Experimental Scheme**



**Figure 55 Experimental Setup**

The sound pressure was measured 3 times at the same location with the same flow velocity. The air was shut off after each measurement. An averaged sound pressure level was calculated from the data acquired from the three measurements. Each of the three measurements gives the same peak with very little variance. Figure 56 shows the averaged sound pressure level obtained at 10 cm above the outlet. The whistle frequency with 8 m/s inlet flow velocity is 1820 Hz with 90 dB magnitude. The result below 150 Hz is not trustworthy due to the cut off frequency of the hemi anechoic chamber and low frequency building noise.



**Figure 56 Averaged Measured Sound Pressure Level**

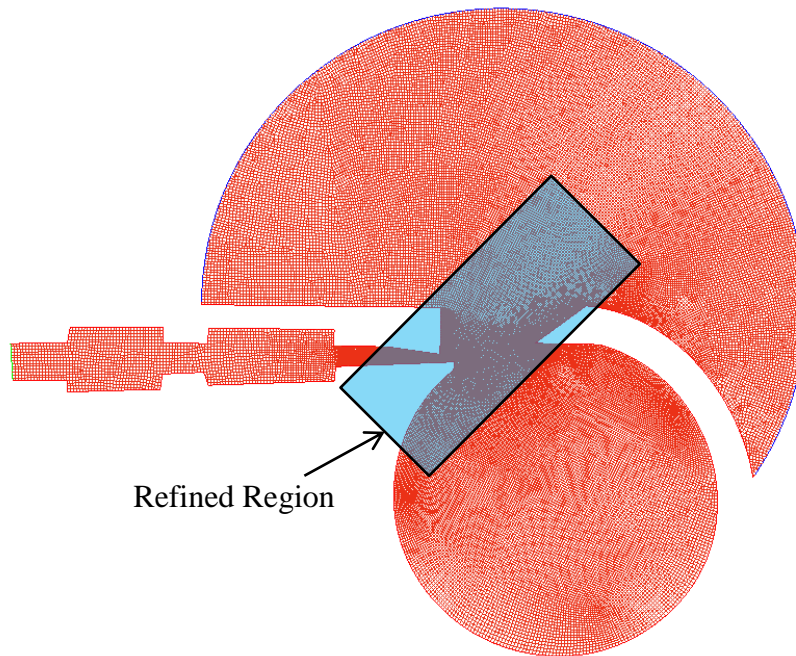
## 5.3 CFD Simulation

### 5.3.1 CFD Mesh

A CFD 2-D mesh of the whistle was generated using both structured and unstructured quad elements. The structured meshing strategy is used at some regions with regular or simple geometry while the unstructured meshing strategy is used at regions with irregular geometry. There were 51701 elements and 53689 nodes total. The minimum element size is  $3.3 \times 10^{-5}$  m while the maximum element size is  $3.3 \times 10^{-4}$  m. The shaded region in Figure 57 was extensively refined because vortices were expected to form in this region. The wall height of the mesh at the triangular obstacle satisfies  $y^+ < 6$  (see Chapter 3.5).

The Jacobian is used to check the overall element quality. Since it is related to the deviation of an actual element from the “perfect” shape. For example, the perfect shape of a triangular element is the equilateral and the perfect shape of a quad element is a square. By mapping an ideal element in parametric coordinates (i.e. the parametric coordinates of a perfect quad elements are (1,1), (-1,1), (-1,-1), (1, -1)) to the actual element in the global coordinates, the Jacobian matrix can be obtained. Usually, the Jacobian of an element in engineering meshing software is the ratio of the smallest determinant and the largest determinants of the Jacobian matrices evaluated at the integration points. In the CFD mesh of the whistle, only 26 of 51701 elements have a Jacobian less than 0.7 and the minimum Jacobian is 0.55. Jacobians of 0.7 and above are recommended [56].





**Figure 57 CFD Mesh of the Whistle**

### **5.3.2 CFD Simulations**

A total of 4 CFD runs are made. Table 7 shows the CFD setup parameters in common, and Table 8 shows what is unique for each of the four runs. The first 5000 time steps are disregarded because the flow is not well developed before  $5 \times 10^{-2}$  s. The velocity field and density field at each of the latter 10,000 time steps for each run are exported. The SST  $k - \omega$  and  $k - \varepsilon$  turbulence models were used.

**Table 7 CFD Simulation Setup (Common Parameters)**

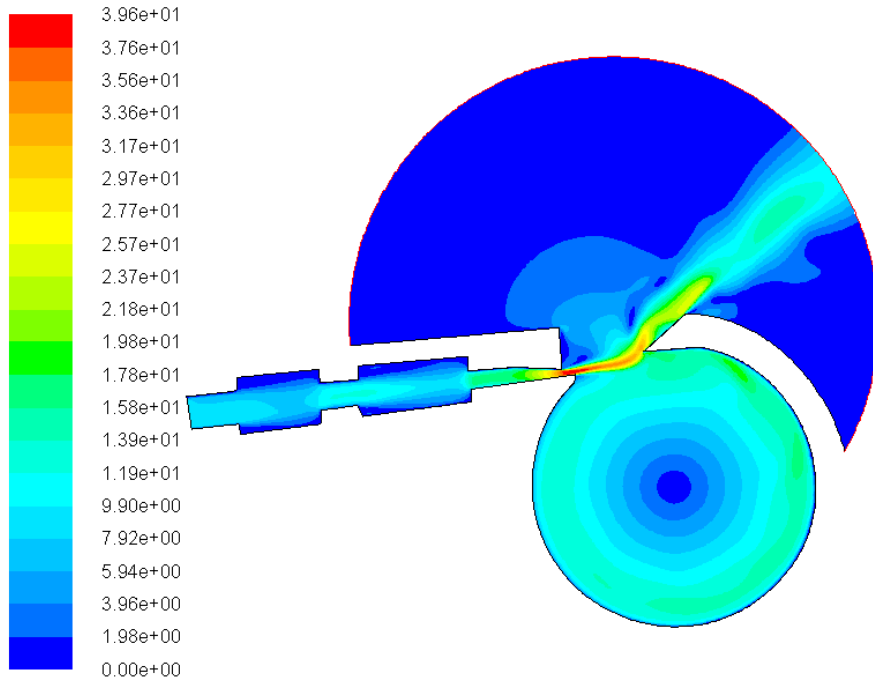
Pressure-Velocity Coupling	Simple
Gradient Method	Green-Gauss cell based
Inlet	Turbulent Intensity: 6.57%, Hydraulic Diameter: 0.00257m
Outlet	Pressure outlet at 1 atm. Turbulence parameters same above
Initialization	Standard initialization from inlet
Convergence Criterion	All residual $< 1 \times 10^{-3}$
Solution Output	Velocity field and density field at each time step
Time step	Time step size: $1 \times 10^{-5}$ s, 15,000 time steps

**Table 8 Simulation Setup (Parameters for Each Case)**

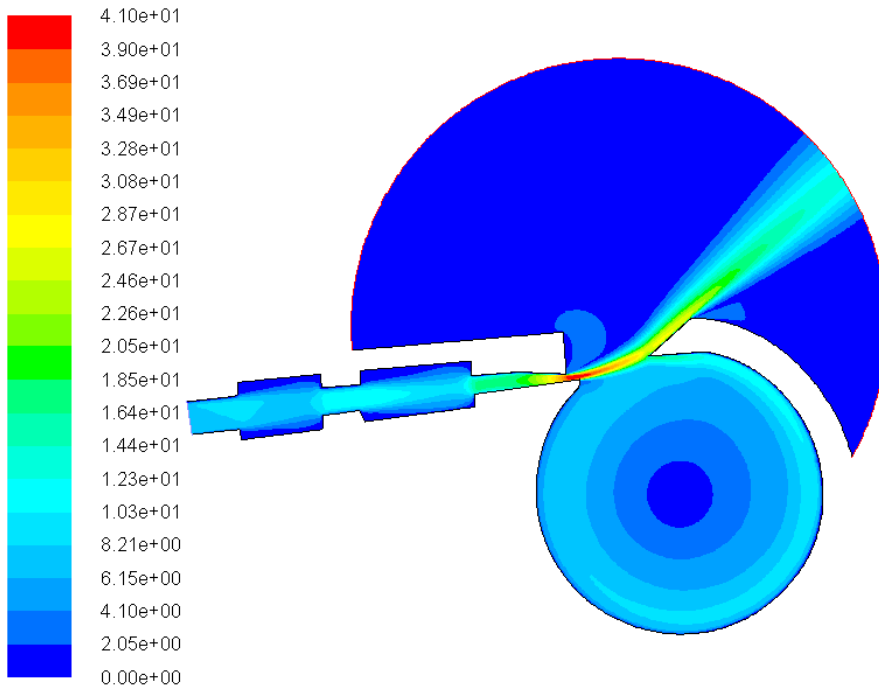
Runs	Turbulence Model	Air Property	Inlet Type and Value
Run 1	Standard k- $\epsilon$	Ideal-gas	Mass Flow Inlet $\dot{m} = 0.02489$ kg/s
Run 2	Standard k- $\epsilon$	Incompressible	Velocity Inlet $V = 8$ m/s
Run 3	SST k- $\omega$	Ideal-gas	Mass Flow Inlet $\dot{m} = 0.02489$ kg/s
Run 4	SST k- $\omega$	Incompressible	Velocity Inlet $V = 8$ m/s

Figures 58 through 61 show the flow velocity magnitude for runs 1 through 4.

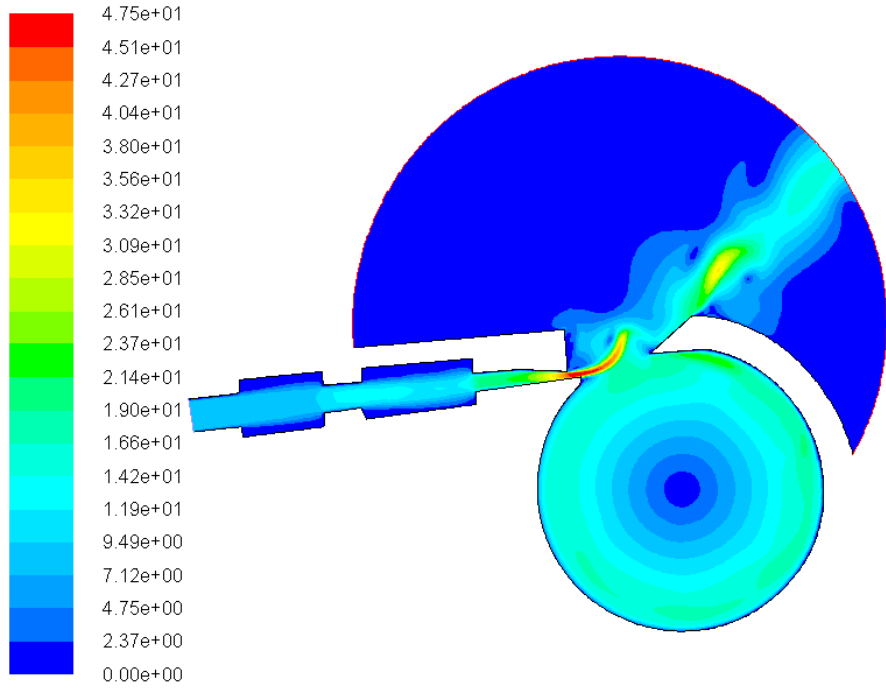
The flow fluctuation is the vortex shedding which will produce sound. Using the standard  $k - \epsilon$  model and incompressible flow, the pressure fluctuations were quickly damped out and vortex shedding was not captured. However, each of the other three models successfully simulated the phenomenon.



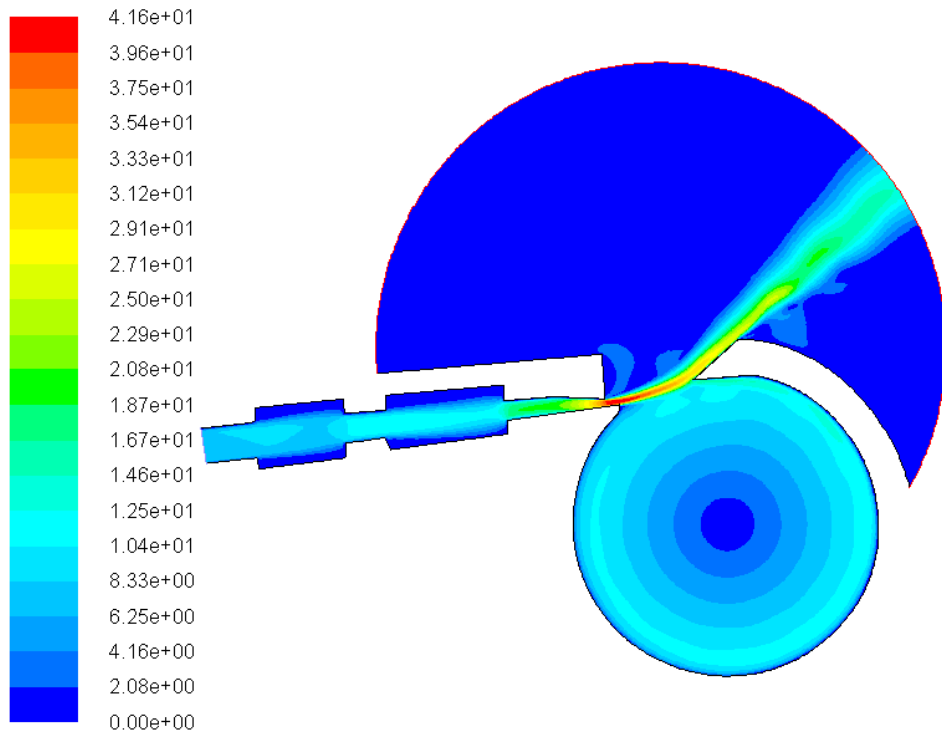
**Figure 58 Contour of Velocity Magnitude (Run1)**



**Figure 59 Contour of Velocity Magnitude (Run2)**



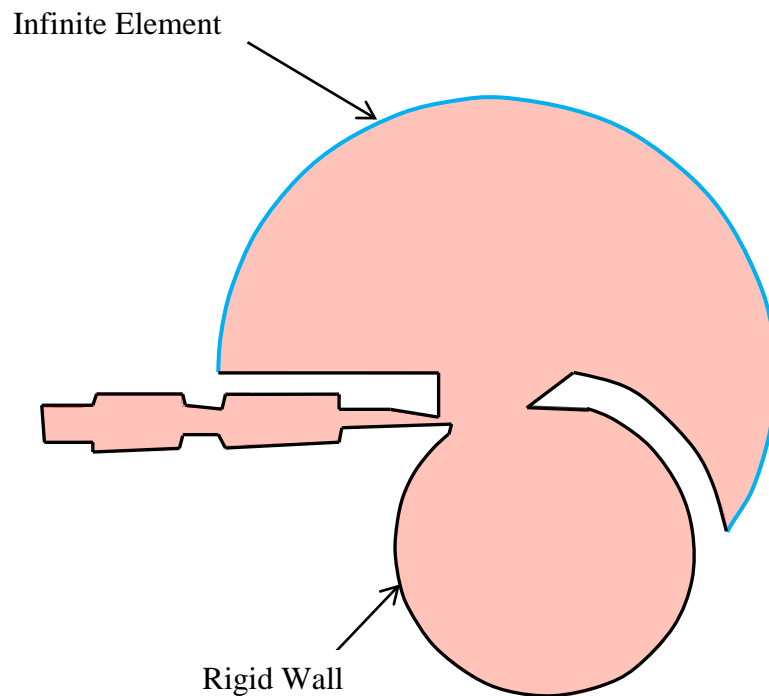
**Figure 60 Contour of Velocity Magnitude (Run3)**



**Figure 61 Contour of Velocity Magnitude (Run4)**

### 5.3.3 Acoustic Simulation

The CFD results from the four runs were then used to determine the aeroacoustic sources for acoustic FEM analyses. Figure 62 shows the boundary conditions for the acoustic FEM analysis. Infinite elements were used at the outlet of the domain while all other edges were assumed to be rigid ( $u = 0$  and  $v = 0$ ). The acoustic mesh has the same geometric dimensions as the CFD mesh, but is much coarser. As mentioned in previous chapters, a coarser acoustic mesh reduces the computation time of the acoustic direct frequency analysis.



**Figure 62 Boundary Conditions of Acoustic Simulation**

The flow velocity and density fields were obtained from the CFD with an aim to determine the aeroacoustic sources from Lighthill's analogy. The total amount of data was 30 GB and the computer time was approximately 48 hours. The velocity and density fields at each of the 10,000 time steps were imported to the FFT ACTRAN ICFD solver, and the sources were calculated by the ICFD solver in the time domain (see chapter 4.2.3.3 for the definition of the source terms and the equation used to determine the source terms). A Fast Fourier Transform was performed using a Hann Window (see Chapter 4.2.3.3) to convert the time domain source terms to the frequency domain. Then the frequency domain data is mapped from the CFD mesh to the acoustic mesh using the conservative integration method (see Chapter 3.3.1) so that all the sources were preserved during this process. A direct frequency analysis was performed to calculate the acoustic wave propagation. The sound power is evaluated at the outlet (infinite element boundary condition) of the acoustic domain (which coincides with the outlet of the CFD domain) (see Chapter 4.2.3.3 for the definition of sound power).

#### **5.3.4 Scaling**

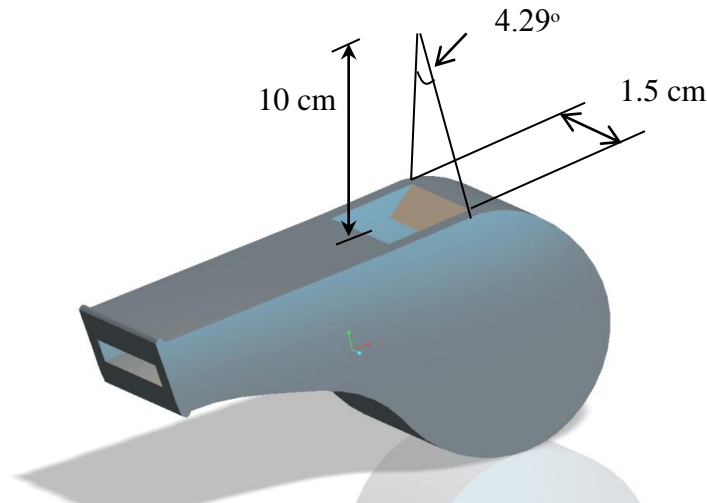
The simulation is performed in 2-D while the measurement was in 3-D. Accordingly, the 2-D results must be properly scaled to compare to measurement (in 3-D).

According to the sound power scaling laws (see Chapter 3.6.1), the sound power in 2-D should be multiplied by the Mach number. In the whistle case, the Mach number of the free stream was determined to be 0.023. As a result of scaling, 6.61 dB should be subtracted from the 2-D result.

The 2-D assumption assumes that the modeled cross-section is infinitely thick. In actuality, the whistle is finite in length. As a result the sound pressure should be reduced to account for the actual length. An angle  $\theta$  of 8.58 degrees (0.15 rad) can be defined according to Figure 63. Using Equation 3-8, the difference of the sound pressure level generated by the infinite depth of whistle and by the finite depth (1.5 cm) is calculated as follows

$$L_p = 10 \log_{10} \left( \frac{p_{infinite}^2}{p_{ref}^2} \right) - 10 \log_{10} \left( \frac{p_{finite}^2}{p_{ref}^2} \right) = 10 \log_{10} \left( \frac{\pi \text{ rad}}{0.15 \text{ rad}} \right) = 13.2 \text{ dB}$$

Therefore, 13.2 dB needs to be subtracted from the 2-D result. Additionally, 3 dB should be added to compensate for the Hann Window (see Chapter 4.2.4).



**Figure 63 Scale the Sound Pressure of a Whistle**

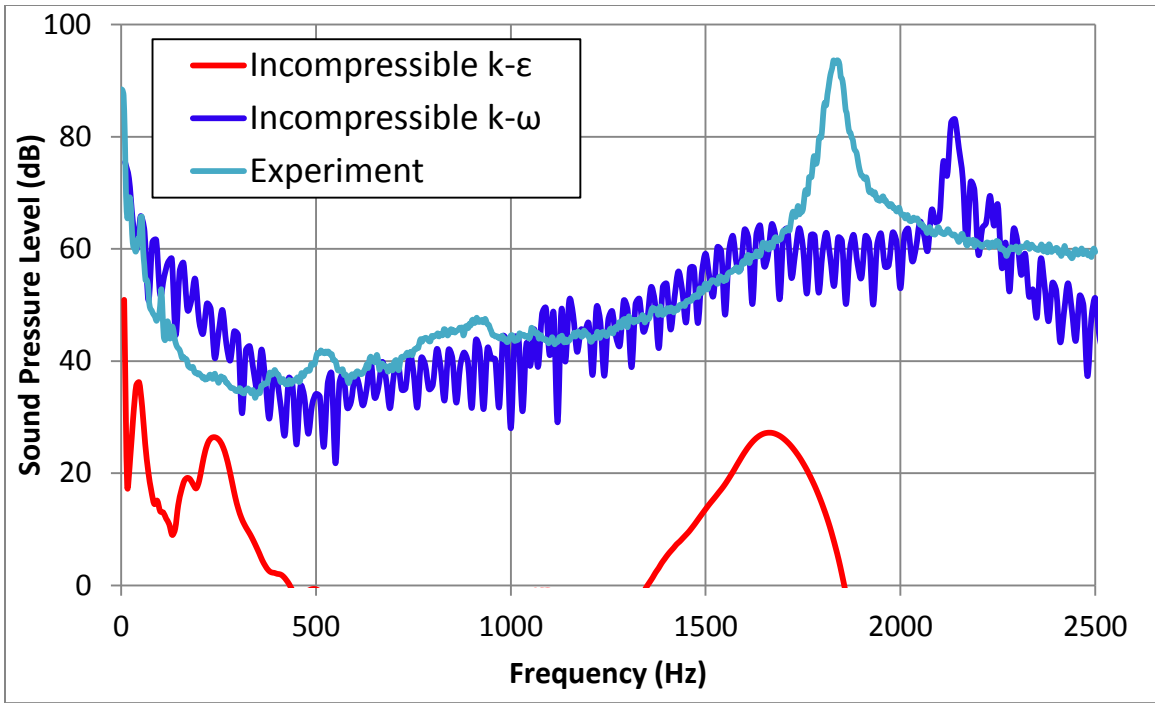
### **5.3.5 Results and Discussion**

Figures 64 and 65 show the simulation result for incompressible cases and compressible cases respectively. The compressible simulations compare better to measurement than the other cases. One reason for this is that the jet which strikes the

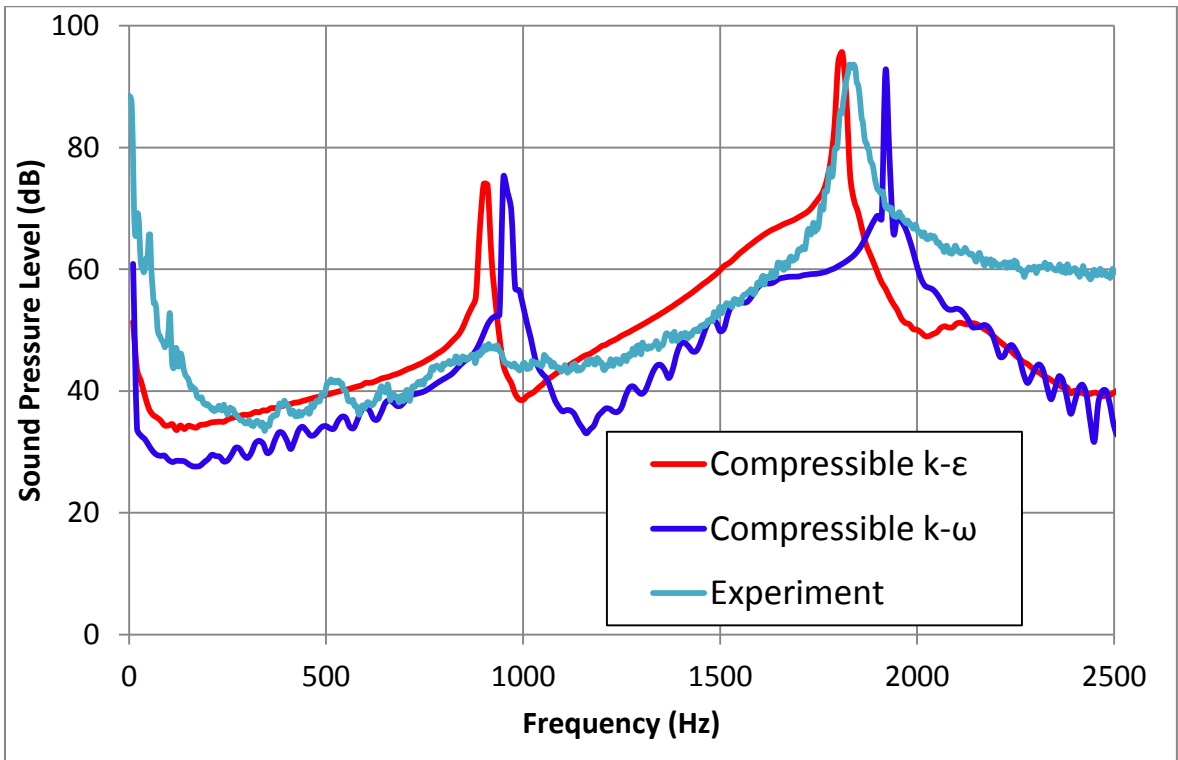
obstacle has a velocity magnitude of approximately 45 m/s and this is more than 10% of the Mach number. Although, it might be considered incompressible for most CFD applications, aeroacoustic simulations require that the pressure fluctuations are modeled correctly. Hence, compressibility proves to be essential. Figure 64 also indicates that the  $k - \varepsilon$  turbulence model does not perform well when incompressible flow is used if flow separation occurs. Figure 65 shows that compressible models predict the vortex shedding frequencies (i.e., whistle tones).

The peaks right below 1000 Hz likely correspond to a periodic behavior present in 2-D that would not be simulated in 3-D. A 3-D simulation could be explored to better account for the finite distance (1.5 cm) between the side walls which might invalidate the symmetry (2-D) assumption. In addition, an anti-aliasing filter may be used to suppress the solution oscillations caused by cell- $Re$  problem which resides in the discretized Navier-Stokes equation solutions [57] [58]. The scaling method developed in this thesis successfully scaled the three sets (compressible  $k - \varepsilon$  and both compressible and incompressible SST  $k - \omega$ ) of 2-D results to match the measurements within a difference of a few dB.





**Figure 64 Whistle Simulation Results (Incompressible)**



**Figure 65 Whistle Simulation Results (Compressible)**

## **Chapter 6**

### **Summary and Future Work**

#### **6.1 Summary**

Undoubtedly, computational fluid dynamics (CFD) has progressed considerably in the past decades due to the revolutionary development of computer hardware and solution techniques of differential equations. The advancement of CFD has also made aeroacoustic simulation, which is traditionally computationally intensive, less expensive than ever before. In the meanwhile, aeroacoustics has attracted increasing attention not only because of the tightened government regulations on noise emission, but also people's demand of higher living standards. Additionally, a manufacturer of a product with an excellent aeroacoustic performance is more likely to winkle customers into making purchases, which in turn benefits the global economy. For example, good jet engine designs can reduce the jet noise so that travelers can better enjoy their flights. In addition, the reduction of the flow noise is often accompanied by the minimization of energy cost and the improvement of the durability of the structures [59] [60]. In industry, whistle noise has become a common problem because of the much more sophisticated system design with an increasing number of components in the flow field. Additionally, fan noise is also a common concern because it contributes to noise problems significantly.

The objective of this thesis was to examine the utilization of CFD and acoustic FEM. in consort to determine aeroacoustic noise due to vortex shedding. An emphasis has been placed on simplifying the analyses to 2-D to reduce CPU time. Additionally, the application studied is whistle noise at low Mach numbers which is a concern for the HVAC, automotive and heavy equipment industries.

It has been shown that convergence is faster for a structured mesh. Generally speaking, it is recommended to use the structured mesh when it does not take too much time to generate. However, using an unstructured mesh is also acceptable. The simulations with unstructured meshes in this thesis have been successful.

Whistle noise modeling is the major topic of this thesis. The use of a CFD-sound propagation solver coupling approach was validated by comparing simulation results to measurement. In addition, the results of Helmholtz resonator and flow over cylinder case were compared, in Chapter 4, to analytical solutions.

Although it has been verified that the incompressible flow assumption can be sufficient for some flow situations with a very low flow speed, it is recommended to assume compressible flow instead of incompressible in cases where the flow velocity is more than 10% of the Mach number. If that is the case, the aeroacoustic source terms are very sensitive to density changes. Failure to use compressible flow will potentially result in solutions that do not even capture the vortex shedding phenomenon. For example, the incompressible  $k - \varepsilon$  turbulence model in conjunction with the acoustic was not able to successfully model the aeroacoustic sources for the whistle. On the contrary, both the compressible  $k - \varepsilon$  and SST  $k - \omega$  models were able to capture the vortex shedding and the acoustic solver was able to produce good results that are comparable to measurement.

Modeling a 3-D situation in 2-D and applying scaling to the 2-D result is another important contribution of this thesis. In the modeling, the scaled 2-D results were close to the experimental result within a few dB. If the 2-D simulation is set up properly, the scaled 2-D result can be used to predict the measured sound pressure level. Generally, 2-

D simulation is faster than 3-D because there are fewer nodes. Moreover, 2D models are simpler because they have fewer parameters than corresponding models in 3D. As a result, it is recommended to use a 2-D model when applicable instead of 3-D in the initial design stage for industrial projects as the turnaround time and the cost can be greatly reduced.

The CFD simulation is the most important part of a complete aeroacoustic simulation because the transient solution data is used to calculate the aeroacoustic sources. There is no turbulence model that will work for all types of flow situations, and therefore, it is important to choose the turbulence model which is suitable for a certain type of flow. The  $k - \varepsilon$  and  $k - \omega$  models have shown similar convergence rates and both models perform well for a wide range of flow situations.

## **6.2 Future Work**

A 2-D simulation is the first step towards more complicated modeling approaches. However, 2D models are only applicable for simpler and more idealized geometries. Hence, a 3-D simulation should be performed before finalizing the design. A logical next step is to explore 3D simulation for a similar whistle case.

Validation of models is the first step to actually using models to drive design. It is recommended that continued validation of models be performed to accumulate experience.

Another logical step would be to start investigating more complicated problems in 2-D. For example, a similar investigation examining fan noise is recommended. The

models studied in this thesis are all static (without any moving parts) whereas fan noise problems require a moving mesh.

## References

- [1] H. D. Baumann and W. B. Coney, "Noise of Gas Flows," in *Noise and Vibration Control Engineering: Principles and Applications*, Hoboken, NJ, John Wiley & Sons, 2006, pp. 611-658.
- [2] M. J. Lighthill, "On Sound Generated Aerodynamically: I. General Theory," *Proceedings of the Royal Society*, vol. 211, pp. 564-587, 1952.
- [3] J. E. Ffowcs Williams and D. L. Hawkings, "Sound Generation by Turbulence and Surfaces in Arbitrary Motion," *Proceedings of Royal Society*, vol. 264, no. 1151, pp. 321-342, 1969.
- [4] W. Layton and A. Novotný, "On Lighthill's Acoustic Analogy for Low Mach Number Flows," in *New Directions in Mathematical Fluid Mechanics*, Basel, Switzerland, Birkhäuser, 2010, pp. 247-279.
- [5] M. Wang, J. B. Freund and S. K. Lele, "Computational Prediction of Flow-Generated Sound," *Annual Review of Fluid Mechanics*, vol. 38, pp. 483-512, 2006.
- [6] ANSYS Inc., *FLUENT 14.0 User's Guide*, 2011.
- [7] A. D. Trim, H. Braaten, H. Lie and M. A. Tognarelli, "Experimental Investigation of Vortex-Induced Vibration of Long Marine Risers," *Journal of Fluids and Structures*, vol. 21, no. 3, pp. 335-361, 2005.
- [8] M. J. Crocker, *Handbook of Acoustics*, New York: John Wiley & Sons, Inc., 1998.

- [9] H. P. Wallin, U. Carlsson, M. Abom, H. Boden and R. Glav, *Sound and Vibration*, Stockholm: KTH, 2011.
- [10] S. R. Ahmed, "Aerodynamic Sound Sources in Vehicles-Prediction and Control," in *Handbook of Noise and Vibration Control*, Hoboken, NJ, John Wiley & Sons, Inc, 2007, p. 1074.
- [11] G. Birkhoff, "Formation of Vortex Streets," *Journal of Applied Physics*, vol. 24, no. 1, pp. 98-103, January 1953.
- [12] J. F. Douglas, J. M. Gasiorek and J. A. Swaffield, *Fluid Mechanics*, London: Pitman Publishing, 1979.
- [13] J. H. Lienhard, "Synopsis of lift, drag, and vortex frequency," Washington State University, Pullman, Washington, 1966.
- [14] E. F. Relf, "On the sound emitted by wires of circular section when exposed to an air current," *Philosophical Magazine*, vol. 42, no. 247, pp. 173-176, 1921.
- [15] R. D. Blevins, "Review of sound induced by vortex shedding from cylinders," *Journal of Sound and Vibration*, vol. 92, no. 4, pp. 455-470, 1984.
- [16] M. M. Zdravkovich, "Complementary comment on "review of sound induced by vortex shedding", " *Journal of Sound and Vibration*, vol. 99, no. 2, pp. 295-297, 1985.
- [17] L. Rayleigh, *Theory of Sound*, New York: Dover Publications, 1945.

- [18] E. Z. Stowell and A. F. Deming, "Vortex noise from rotating cylindrical rods," *Journal of the Acoustical Society of America*, vol. 7, pp. 190-198, 1936.
- [19] P. Leehey and C. E. Hanson, "Aeolian tones associated with resonant vibration," *Journal of Sound and Vibration*, vol. 13, pp. 456-483, 1971.
- [20] M. Howe, *Acoustics of fluid structure interactions*, Cambridge, UK: Cambridge University Press, 1998, p. 104.
- [21] F. Mechel, *Formulas of Acoustics*, Berlin, Germany: Springer-Verlag, 2002.
- [22] FFT, ACTRAN 12.1 User's Guide, Belgium, 2011.
- [23] B. E. Launder and D. B. Spalding, *Lectures in Mathematical Models of Turbulence*, Academic Press, 1972.
- [24] L. Xiong, Y. Lin and S. Li, "k-ε Turbulent Model and its Application to the FLUENT," *Industrial Heating*, vol. 36, no. 4, pp. 13-15, 2007.
- [25] A. N. Kolmogorov, "Equations of Turbulent Motion of an Incompressible Fluid," *Izvestia Academy of Sciences; USSR; Physics*, vol. 6, no. 1-2, pp. 56-58, 1942.
- [26] D. C. Wilcox, "Numerical Study of Separated Turbulent Flows," in *AIAA Paper 74-584*, Palo Alto, CA, 1974.
- [27] D. C. Wilcox and R. M. Traci, "A Complete Model of Turbulence," in *AIAA Paper 76-351*, San Diego, CA, 1976.



- [28] D. C. Wilcox and M. W. Rubesin, "Progress in Turbulence Modeling for Complex Flow Fields Including Effects of Compressibility," NASA TP-1517, 1980.
- [29] D. C. Wilcox, *Turbulence Modeling for CFD*, Glendale, CA: Griffin Printing, 1993.
- [30] F. R. Menter, "Zonal two-equation k-w turbulence model for aerodynamic flows," *AIAA Paper 93-2906*, 1993.
- [31] F. R. Menter, "Influence of freestream values on k-w turbulence model predictions.," *AIAA Journal*, vol. 30, no. 6, 1992.
- [32] F. R. Menter, M. Kuntz and R. Langtry, "Ten years of industrial experience with the SST Turbulence Model," in *Turbulence, Heat and Mass Transfer 4*, Antalya, Turkey, 2003.
- [33] F. R. Menter, "Two-equation eddy-viscosity Turbulence models for engineering applications," *AIAA Journal*, vol. 32, no. 8, pp. 1598-1605, 1994.
- [34] T. B. Gatski, M. Y. Hussaini and J. L. Lumley, *Simulation and Modeling of Turbulent Flows*, New York: Oxford University Press, Inc, 1996.
- [35] L.-W. Hu and M. S. Kazimi, "LES benchmark study of high cycle temperature fluctuations caused by thermal striping in a mixing tee," *International Journal of Heat and Fluid Flow*, vol. 27, no. 1, pp. 54-64, February 2006.
- [36] D. You and P. Moin, "A dynamic global-coefficient subgrid-scale eddy-viscosity model for large-eddy simulation in complex geometries," *Physics of Fluids*, vol. 19,

no. 6, 2007.

- [37] D. W. Herrin, T. W. Wu and A. F. Seybert, "Practical Issues regarding the use of the Finite and Boundary Element Methods for Acoustics," *Building Acoustics*, vol. 10, no. 4, pp. 257-279, 2003.
- [38] D. S. Burnett and R. L. Holford, "An ellipsoidal acoustic infinite element," *Computer methods in applied mechanics and engineering*, vol. 164, no. 1-2, pp. 49-76, 2 October 1998.
- [39] S. Sovani, W. Seibert and M. Ehlen, "Simulation of Transient Aerodynamics Predicting Buffeting, Roaring and Whistling using CFD," in *MIRA International Vehicle Aerodynamics Conference*, 2004.
- [40] G. M. Lilley, "The Radiated Noise from Isotropic Turbulence Revisited," NASA Langley Research Center ICASE Report 93-75; NASA CR-191547, 1993.
- [41] Takahashi Kin'ya, M. Miyamoto, Y. Ito, T. Takami, T. Kobayashi, A. Nishida and M. Aoyagi, "Numerical analysis on 2D and 3D edge tones in terms of aerodynamic sound theory," in *Proceedings of 20th International Congress on Acoustics, ICA 2010*, Sydney, Australia, 2010.
- [42] G. Rubio, W. Roeck, W. Desmet and M. Baelmans, "Large Eddy Simulation for Computation of Aeroacoustic Sources in 2D-Expansion Chambers," in *Direct and Large-Eddy Simulation VI*, Springer Netherlands, 2006, pp. 555-564.

- [43] W. Layton and A. Novotny, "On Lighthill's acoustic analogy for low Mach number flows," in *New Directions in Mathematical Fluid Mechanics*, Basel, Switzerland, Birkhäuser Basel, 2010, pp. 247-279.
- [44] D. C. Wilcox, *Basic Fluid Mechanics*, San Diego, California: Birmingham Press, Inc., 2007.
- [45] M. Wang, J. B. Freund and S. K. Lele, "Computational Prediction of Flow-Generated Sound," *The Annual Review of Fluid Mechanics*, vol. 38, pp. 483-512, 2006.
- [46] H.-J. Bungartz and M. Schäfer, *Fluid-structure Interaction: Modelling, Simulation, Optimization.*, Berlin: Springer, 2006.
- [47] S. M. Salim and S. C. Cheah, "Wall  $y^+$  Strategy for Dealing with Wall-bounded Turbulent Flows," in *Proceedings of the International MultiConference of Engineers and Computer Scientists 2009*, Hong Kong, 2009.
- [48] tecplot, "A Wind Turbine CFD Solution - Turning up the (green) power with Tecplot 360 and Pointwise," 26 May 2011. [Online]. Available:  
<http://www.tecplot.com/LinkClick.aspx?fileticket=g6V6bAAezYg%3d&tabid=317>.  
[Accessed 1 June 2012].
- [49] O. R. Burggraf, "Analytical and numerical studies of the structure of steady separated flows," *Journal of Computational Physics*, vol. 89, pp. 389-413, 1990.

- [50] U. Ghia, K. N. Ghia and C. T. Shin, "High-Re solutions for incompressible flow using the Navier-Stokes equations and a multigrid method," *Journal of Computational Physics*, vol. 48, pp. 387-411, 1982.
- [51] U. Ingard, "On the Theory and Design of Acoustic Resonators," *Journal of the Acoustical Society of America*, vol. 25, no. 6, pp. 1037-1061, 1953.
- [52] ANSYS Inc., "ANSYS FLUENT Tutorial," 2008.
- [53] S. E. Kim and D. Choudhury, "A Near-Wall Treatment Using Wall Functions Sensitized to Pressure Gradient," in *Proceedings of the ASME/JSME Fluids Engineering and Laser Anemometry Conference and Exhibition*, Hilton Head, SC, 1995.
- [54] S. V. Patankar and D. B. Spalding, "A Calculation Procedure for Heat, Mass and Momentum Transfer in Three-dimensional Parabolic Flows," *International Journal of Heat Mass Transfer*, vol. 15, p. 1787, 1972.
- [55] F. Nicoud and F. Ducros, "Subgrid-Scale Stress Modelling Based on the Square of the Velocity Gradient Tensor.Flow," *Turbulence, and Combustion*, vol. 62, no. 3, pp. 183-200, 1999.
- [56] Altair Engineering, Inc., "HyperWorks Desktop User's Guide," 2012.
- [57] J. M. McDonough, "Lectures in Computational Fluid Dynamics of Incompressible Flow: Mathematics, Algorithms and Implementations," 22 January 2008. [Online]. Available: <http://www.engr.uky.edu/~acfd/me691-lctr-nts.pdf>. [Accessed 1 May

2012].

- [58] F. G. Shuman, "Numerical Methods in Weather Prediction: II. Smoothing and Filtering," *Monthly Weather Review*, vol. 85, no. 11, pp. 357-361, November 1957.
- [59] H. H. (. Hubbard, "Aeroacoustics of Flight Vehicles: Theory and Practice, Vol. 1: Noise Sources, Vol. 2: Noise Control," *NASA RP-125*, 1991.
- [60] K. W. T. Christopher, "Computational Aeroacoustics: Issues and Methods," *AIAA Journal*, vol. 33, no. 10, pp. 1788-1796, October 1995.
- [61] A. Oberai, F. Ronaldkin and T. Hughes, "Computation of Trailing-Edge Noise due to Turbulent Flow over an Airfoil," *AIAA Journal*, vol. 40, pp. 2206-2216, 2002.
- [62] A. Oberai, F. Ronaldkin and T. Hughes, "Computational Procedures for Determining Structural-Acoustic Response due to Hydrodynamic Sources," *Comput. Methods Appl. Mech. Engrg.*, vol. 190, pp. 345-361, 2000.
- [63] S. J. Wang and A. S. Mujumdar, "A comparative study of five low Reynolds number  $k-\epsilon$  models for impingement heat transfer," *Applied Thermal Engineering*, vol. 25, no. 1, pp. 31-44, January 2005.
- [64] M. L. Munjal, *Acoustics of Ducts and Mufflers*, New York: John Wiley & Sons, 1987.
- [65] P. Davies, J. B. Coelho and M. Bhattacharya, "Reflection coefficients for an unflanged pipe with flow," *Journal of Sound and Vibration*, vol. 72, no. 4, pp. 543-

546, 22 October 1980.

- [66] O. Ozgun and M. Kuzuoglu, "Non-Maxwellian locally-conformal PML absorbers for finite element mesh truncation," *IEEE Trans Antennas Propagation*, pp. 931-937, 2007.
- [67] H. Beriot and M. Tournour, "On the locally-conformal perfectly matched layer implementation for helmholtz equation," in *Proceedings of NOVEM 2009 Conference*, Oxford, 2009.
- [68] O. Ozgun and M. Kuzuoglu, "Near field performance analysis of locally-conformal perfectly matched absorbers via Monte-Carlo simulations," *Journal of computational Physics*, no. 227, pp. 1225-1245, 2007.
- [69] D. J. Tritton, "Experiments on the Flow Past a Circular Cylinder at Low Reynolds Numbers," *Journal of Fluid Mechanics*, vol. 6, p. 547, 1959.

## **Vita**

Jiawei Liu was born in Inner Mongolia, China on May 25, 1987. He received the degree of Bachelor of Science in Mechanical Engineering from the University of Kentucky in 2010 with honor. In August 2010, he was accepted by the University Scholar Program of Mechanical Engineering at the University of Kentucky and enrolled in the graduate school. He had a co-op job as a NVH Engineer at Cummins Inc. and had one SAE conference paper during the two years of graduate study.